

AD-A105 854

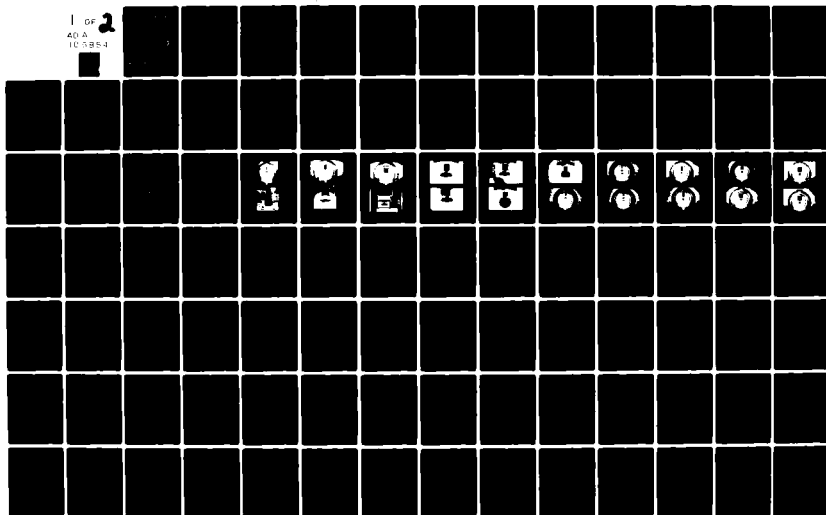
CALIFORNIA INST OF TECH PASADENA GRADUATE AERONAUTIC--ETC F/6 20/4
DETERMINATION OF AIRLOADS ON CERTAIN AIRPORT TOWERS DUE TO AD01--ETC(U)
AUG 81 C D BABCOCK, W H BETTES DOT-TSC-1633
GALCIT-1020

FAA/RD-81-74

NL

UNCLASSIFIED

1 OF 2
AD A
10 5854



DOT/FAA/RD-81-74
DOT-TSC-FAA-81-14

Determination of Airloads on Certain Airport Towers due to Addition of Radomes

(13) LEVEL II

Charles D. Babcock
William H. Bettes

California Institute of Technology
Graduate Aeronautical Laboratories
Pasadena, CA 91125

August 1981
Final Report

DTIC
ELECTE
OCT 16 1981
B

This document is available to the public
through the National Technical Information
Service, Springfield, Virginia 22161.



U.S. Department of Transportation
Federal Aviation Administration

Systems Research and Development Service
Washington DC 20590

AD A105854

DTIC FILE COPY

NOTICE

This document is disseminated under the sponsorship of the U.S. Departments of Defense and Transportation in the interest of information exchange. The U.S. Government assumes no liability for its contents or use thereof.

NOTICE

The U.S. Government does not endorse products or manufacturers. Trade or manufacturers' names appear herein solely because they are considered essential to the objectives of this report.

Technical Report Documentation Page

1. Report No. DOT/FAA/RD-81-74	2. Government Accession No. AD-A105854	3. Recipient's Catalog No. 11
4. Title and Subtitle DETERMINATION OF AIRLOADS ON CERTAIN AIRPORT TOWERS DUE TO ADDITION OF RADOMES.		5. Report Date August 1981
7. Author(s) Charles D. Babcock and William H. Bettes		6. Performing Organization Code DTS-541
9. Performing Organization Name and Address California Institute of Technology* Graduate Aeronautical Laboratories Pasadena CA 91125		8. Performing Organization Report No. DOT-TSC-FAA-81-14 GALCIT-1020
12. Sponsoring Agency Name and Address U.S. Department of Transportation Federal Aviation Administration Systems Research and Development Service Washington DC 20590		10. Work Unit No. (TRAIS) FA121/R1135
15. Supplementary Notes * Under Contract to:		11. Contract or Grant No. DOT-TSC-1633
U.S. Department of Transportation Research and Special Programs Administration Transportation Systems Center Cambridge MA 02142		13. Type of Report and Period Covered FINAL REPORT Jan 1979-Dec. 1980
14. Sponsoring Agency Code FAA-ARD-100		
16. Abstract <p>This report presents the results of wind tunnel tests conducted on three different radome configurations mounted atop three different airport tower designs. The wind tunnel tests were conducted on 1/12th scale models. Field tests were conducted on one full-scale radome and tower configuration and the data compared with the wind tunnel data. The data are useful for comparing the airloads transmitted into an airport-tower roof by the various radomes and for evaluating the effects tower geometry can have on these airloads.</p>		
17. Key Words ASDE-3; Radome wind tunnel tests; Radome wind loading tests; Radome airloads on towers	18. Distribution Statement DOCUMENT IS AVAILABLE TO THE PUBLIC THROUGH THE NATIONAL TECHNICAL INFORMATION SERVICE, SPRINGFIELD, VIRGINIA 22161	
19. Security Classif. (of this report) Unclassified	20. Security Classif. (of this page) Unclassified	21. No. of Pages 136
22. Price		

1/11 15 4/10 C

PREFACE

The work covered by this report was conducted by the Graduate Aeronautical Laboratories of the California Institute of Technology under contract to the U.S. Department of Transportation. Wind tunnel tests were performed on scaled ASDE radome models mounted on scaled models of three towers, the Pei, the Walton Beckett, and the FAA Tests Center's ASDE tower. Full scale field tests were conducted on the FAA Test Center's ASDE Tower to correlate wind tunnel results with results from an actual installation. The purpose of this effort was to establish the airloads that might be expected on represented FAA towers due to an ASDE radome. This report documents the results of the effort.

Accession For	
NTIS GRA&I	<input checked="checked" type="checkbox"/>
DTIC TAB	<input type="checkbox"/>
Unannounced	<input type="checkbox"/>
Justification	
By _____	
Distribution/	
Availability Codes	
Dist	Avail and/or Special
A	

22 21 20 19 18 17 16 15 14 13 12 11 10 9 8 7 6 5 4 3 2 1

9 8 7 6 5 4 3 2 1

Symbol	What You Know	Multiply by	To Find	Symbol
<hr/>				
LENGTH				
	inches	* 2.5	centimeters	cm
	feet	30	centimeters	cm
	yards	0.9	meters	m
	miles	1.6	kilometers	km
<hr/>				
AREA				
	square inches	6.5	square centimeters	cm ²
	square feet	0.09	square meters	m ²
	square yards	0.8	square meters	m ²
	square miles	2.6	square kilometers	km ²
	acres	0.4	hectares	ha
<hr/>				
MASS (weight)				
	ounces	28	grams	g
	pounds	0.45	kilograms	kg
	short tons (2000 lb)	0.9	tonnes	t
<hr/>				
VOLUME				
	teaspoons	5	milliliters	ml
	tablespoons	15	milliliters	ml
	fluid ounces	30	milliliters	ml
	cups	0.24	liters	l
	pints	0.47	liters	l
	quarts	0.96	liters	l
	gallons	3.8	liters	l
	cubic feet	0.03	cubic meters	m ³
	cubic yards	0.76	cubic meters	m ³
<hr/>				
TEMPERATURE (exact)				
	Fahrenheit temperature	5/9 after subtracting 32°	Celsius temperature	°C

[illegible]

Symbol	When You Know	Multiply by	To Find	Symbol
LENGTH				
mm	millimeters	0.04	inches	in
cm	centimeters	0.4	inches	in
m	meters	3.2	feet	ft
mi	miles	1.1	yards	yd
km	kilometers	0.6	miles	mi
AREA				
sq mm	square centimeters	0.16	square inches	sq in
sq cm	square meters	1.2	square yards	sq yd
sq m	square kilometers	0.4	square miles	sq mi
ha	hectares (10,000 m ²)	2.5	acres	ac
MASS (weight)				
g	grams	0.075	ounces	oz
kg	kilograms	2.2	pounds	lb
t	tonnes (1,000 kg)	1.1	short tons	st
VOLUME				
ml	milliliters	0.03	fluid ounces	fl oz
l	liters	2.1	pints	pt
kl	kiloliters	1.06	quarts	qt
m ³	cubic meters	0.76	gallons	gal
cm ³	cubic centimeters	35	cubic feet	cu ft
m ³	cubic meters	1.3	cubic yards	cu yd
TEMPERATURE (base)				
°C	Celsius	9/5 (then add 32)	Fahrenheit temperature	°F

TEMPERATURE (°C)

TABLE OF CONTENTS

<u>Section</u>	<u>Page</u>
1. INTRODUCTION.....	1-1
2. DISCUSSION AND RESULTS.....	2-1
3. REMARKS AND CONCLUSIONS.....	3-1
APPENDIX A - WIND TUNNEL TESTS.....	A-1
APPENDIX B - FIELD TESTS.....	B-1
APPENDIX C - REPORT OF NEW TECHNOLOGY.....	C-1

LIST OF ILLUSTRATIONS

<u>Figure</u>	<u>Page</u>
2-1. WIND TUNNEL AND FIELD TEST DATA COMPARISON AT $\psi = 0$ DEGREES.....	2-2
2-2. WIND TUNNEL AND FIELD TEST DATA COMPARISON AT $\psi = 2.3$ DEGREES.....	2-3
2-3. WIND TUNNEL AND FIELD TEST DATA COMPARISON AT $\psi = 3.6$ DEGREES.....	2-4
A-1. VERTICAL SECTION THROUGH TEN-FOOT WIND TUNNEL. TWO-PARAMETER SIX COMPONENT SUSPENSION SYSTEM.....	A-3
A-2. LOADS AND MOMENT TRANSFER.....	A-4
A-3. TOWER YAW ANGLES.....	A-5
A-4. FAATC TOWER MODEL AND TOWER INSTALLATION IN WIND TUNNEL.....	A-6
A-5. PEI TOWER MODEL.....	A-7
A-6. WELTON-BECKETT TOWER MODEL.....	A-8
A-7. ROTADOME MODEL.....	A-9
A-8. ROTADOME WITH SIMULATED LAP JOINTS ON FAATC TOWER WITH $\psi = 22.5^\circ$	A-10
A-9. TEACUP RADOME MODEL AND ROTADOME MODEL ON FAATC TOWER.....	A-11
A-10. SPHERICAL AND TEACUP RADOME MODELS ON FAATC TOWER.	A-12
A-11. ROTADOME AND SPHERICAL RADOME MODELS ON PEI TOWER.	A-13
A-12. TEACUP RADOME MODEL ON PEI TOWER AND ROTADOME MODEL ON WELTON-BECKETT TOWER.....	A-14
A-13. SPHERICAL AND TEACUP RADOME MODELS ON WELTON-BECKETT TOWER.....	A-15
A-14. FORCE AND MOMENT COEFFICIENTS FOR ROTADOME AT STANDARD HEIGHT ON FAATC TOWER.....	A-19

LIST OF ILLUSTRATIONS

<u>Figure</u>	<u>Page</u>
A-15. FORCE AND MOMENT COEFFICIENTS FOR ROTADOME WITH SIMULATED LAP JOINTS ON FAATC TOWER AT STANDARD HEIGHT.....	A-24
A-16. FORCE AND MOMENT COEFFICIENTS FOR ROTADOME LOAD- CELLS HEIGHT ON FAATC TOWER.....	A-27
A-17. FORCE AND MOMENT COEFFICIENTS FOR ROTADOME WITH SIMULATED LAP JOINTS AT LOAD-CELL HEIGHT ON FAATC TOWER.....	A-30
A-18. FORCE AND MOMENT COEFFICIENTS FOR ROTADOME AND PEI TOWER.....	A-33
A-19. FORCE AND MOMENT COEFFICIENTS FOR ROTADOME ON WELTON-BECKETT TOWER.....	A-38
A-20. FORCE AND MOMENT COEFFICIENTS FOR SPHERICAL RADOME ON FAATC TOWER.....	A-41
A-21. FORCE AND MOMENT COEFFICIENTS FOR SPHERICAL RADOME ON PEI TOWER.....	A-46
A-22. FORCE AND MOMENT COEFFICIENTS FOR SPHERICAL RADOME ON WELTON-BECKETT TOWER.....	A-51
A-23. FORCE AND MOMENT COEFFICIENTS FOR TEACUP RADOME ON FAATC TOWER.....	A-54
A-24. FORCE AND MOMENT COEFFICIENTS FOR TEACUP RADOME ON PEI TOWER.....	A-59
A-25. FORCE AND MOMENT COEFFICIENTS FOR TEACUP RADOME ON WELTON-BECKETT TOWER.....	A-64
A-26. COMBINED ONE-TWELFTH AND ONE-SIXTH-SCALE DATA FOR ROTADOME ON THE FAATC TOWER.....	A-67
A-27. COMBINED ONE-TWELFTH AND ONE-SIXTH-SCALE DATA FOR SPHERICAL RADOME ON THE FAATC TOWER.....	A-68
A-28. FORCE AND MOMENT COEFFICIENTS FOR ROTADOME ON FAATC TOWER WITH LOAD-CELLS INSTALLED AT WIND ANGLES ENCOUNTERED MOST OFTEN DURING FIELD TESTS..	A-69

LIST OF ILLUSTRATIONS

<u>Figure</u>	<u>Page</u>
B-1. ROTADOME AND TOWER AT FAATC.....	B-2
B-2. LOAD-CELL INSTALLATION.....	B-4
B-3. FIELD TEST INSTRUMENTATION LAYOUT.....	B-6
B-4. RAW-DATA SAMPLE VERSUS TIME.....	B-8
B-5. FORCE AND MOMENT COEFFICIENTS AS A FUNCTION OF TIME	B-15
B-6. FORCE AND MOMENT COEFFICIENTS VERSUS DELAY TIME....	B-19

LIST OF TABLES

<u>Table</u>		<u>Page</u>
2-1.	TOWER-ROOFTOP LOADS PREDICTED FOR VARIOUS TEST RADOMES.....	2-8
A-1.	AIRSTREAM DYNAMIC PRESSURE AND RADOME REYNOLDS NUMBER VERSUS AIRSTREAM TEST VELOCITY.....	A-17
A-2.	RADOME DIMENSIONS USED IN DATA REDUCTION.....	A-18
B-1.	LOAD-CELL CALIBRATION FACTORS.....	B-3
B-2.	DATA-AVERAGED RESULTS.....	B-29

NOMENCLATURE

A	Projected frontal area of basic radome
C_C	Cross-wind force coefficient = $\frac{\text{cross-wind force}}{qA}$ (positive to right-hand side when looking into approaching airstream)
C_D	Drag coefficient = $\frac{\text{drag force}}{qA}$ (positive in direction of airstream motion)
C_L	Lift coefficient = $\frac{\text{lift force}}{qA}$ (positive when it tends to lift radome off tower)
C_ℓ	Rolling-movement coefficient* = $\frac{\text{rolling moment}}{qAd}$ (positive when it tends to lower right-hand side of radome as observed looking into approaching airstream)
C_m	Pitching-moment coefficient* = $\frac{\text{pitching moment}}{qAd}$ (positive when it tends to raise section of radome facing into approaching airstream)
d	Platform diameter of basic radome
q	Dynamic pressure of airstream = $\frac{\rho}{2} V^2$
R_d	Reynolds number = $\frac{\rho V d}{\mu}$
R_0	Rotadome support reaction
R_{120}	Rotadome support reaction
R_{240}	Rotadome support reaction
u	Component of wind velocity
v	Component of wind velocity

* Moments are referenced to a point at the intersection of the tower roof and the radome axis of symmetry unless otherwise noted.

V	Velocity of airstream taken at elevation of maximum diameter of radome.
w	Component of wind velocity
θ	Wind angle relative to 0° support leg
θ_w	Wind angle relative to anemometer axis, $\tan^{-1} v/u$
μ	Absolute viscosity of air
ρ	Mass density of air
ψ	Angle of yaw of tower relative to vertical plane through approaching airstream.

Definition of Model Test Configurations

Tower Model:

FAATC	One-twelfth-scale model of the airport tower at FAATC (Federal Aviation Administration Technical Center) in Atlantic City, New Jersey, which was used in the full-scale field tests. Photographs of the wind tunnel model are presented in Figures A-4 and A-7; the field test tower is pictured in Appendix B.
Pei	One-twelfth-scale model of a Pei-designed airport tower similar to the tower at Chicago O'Hare Airport. Photographs of this pentagonal tower model are presented in Figure A-5.
Welton-Beckett	One-twelfth-scale model of a Welton Beckett-designed airport tower similar to the tower at the Dallas-Fort Worth airport. Photographs of this tower model are presented in Figure A-6.

Radome Model:

Rotadome	One-twelfth-scale model of an 18-foot diameter rotating radome designated ASDE-3 and incorporating an elliptical upper section and modified conical lower section. The model
----------	--

included the radome support structure and legs and a simulated rotadome drive system. Photographs of this model are presented in Figures A-7, A-8, A-9, A-11, and A-12. A photograph of the field test rotadome is presented in Appendix B.

Spherical

One-twelfth-scale model of a 19.2-foot diameter truncated spherical (geodesic) radome designated ASDE-3. The surface of the model sphere was roughened to the texture of an outside plastered wall to force boundary layer transition similar to that for a geodesic structure. Photographs of this model are presented in Figures A-8, A-10, A-11, and A-13; note that the lower edge of the sphere was sealed to the tower roof using a 3/8-inch thick sponge rubber strip to prevent air-flow under the sphere.

Teacup

One-twelfth-scale model of a 9.12-foot diameter spherical radome which is truncated top and bottom with the top section fitted with a nearly flat conical section. This model was formed from the spherical model by replacing the upper portion of the sphere with a conical overhanging section. Photographs of this model are presented in Figure A-9, A-10, A-12, and A-13.

1. INTRODUCTION

This report presents the results of wind tunnel tests conducted on three different airport tower-mounted radomes which house ground-search radar antennas. The antennas are for use in determining the location and movement of aircraft and other vehicles on airport runways and the surrounding areas. The three radomes tested were a rotadome (ASDE-3), a spherical radome (ASDE-2), and the teacup radome. Each radome was tested mounted atop three different-style airport towers. The towers represented were (a) one of the FAATC towers which is of truss-type construction; (b) a Pei-designed tower, which is of pentagonal cross-section similar to that at the Chicago's O'Hare Airport; and (c) a Welton Beckett-designed tower similar to that at the Dallas-Fort Worth Airport. Each tower and radome are described in the nomenclature. Photographs are also presented for each test combination in Appendix A.

The wind tunnel models were constructed to 1/12th scale, and because of the limited Reynolds number range which could be achieved with these models in the wind tunnel, field tests were carried out full scale under actual wind conditions. The field tests were conducted using one of the FAATC towers in Atlantic City, New Jersey, and the ASDE-3 rotadome which uses rotation of the outer shell to provide the same window for the radar equipment throughout the 360° scan. The field test data are used to correlate the wind tunnel data with actual wind loads encountered in the field.

The purposes of these tests were (1) to compare the airloads which might be encountered by each of these radomes, and (2) to determine the effects various tower geometries might have on these airloads. The data could also be used to establish criteria for the loads which might be transmitted onto airport tower roofs due to airloads acting on a radome attached to that roof.

2. DISCUSSION AND RESULTS

It should be emphasized that the forces and moments determined from the wind tunnel and field tests are essentially the static forces and moments acting on the radome. The field test data contained both static and dynamic components. The dynamic components were removed from these field data during data reduction since these loads result in large measure from the excitation of the tower by the wind forces.

Complete data from the wind tunnel tests are presented along with a discussion of the results of Appendix A. The field test results and discussion are presented in Appendix B.

Wind tunnel test data from Figures A-26 and A-28 (Appendix A) were used together with a majority of the field test data to determine how well the wind tunnel data could be expected to predict the airloads actually encountered by a tower-mounted radome in a wind environment. The wind tunnel moment data were re-reduced to act in the plane representative of the top of the field test load cells to make these moments compatible with those measured during the field tests. The field tests data could not be adjusted to the reference tower-roof level used for the wind tunnel data because the horizontal load force could not be measured during the field tests.

Those data which are directly comparable between wind tunnel and field tests are presented in Figures 2-1, 2-2 and 2-3. Field test data which have been omitted from the comparison are those where either wind direction was rapidly changing or where a substantial vertical wind velocity component was recorded. In either case, quasi steady-state conditions were unlikely to exist and the chance of an uneven velocity front approaching the tower and radome was great. Since only a single anemometer station was used during the field tests, any gradient in the wind velocity in a horizontal plane resulted in load cell data which

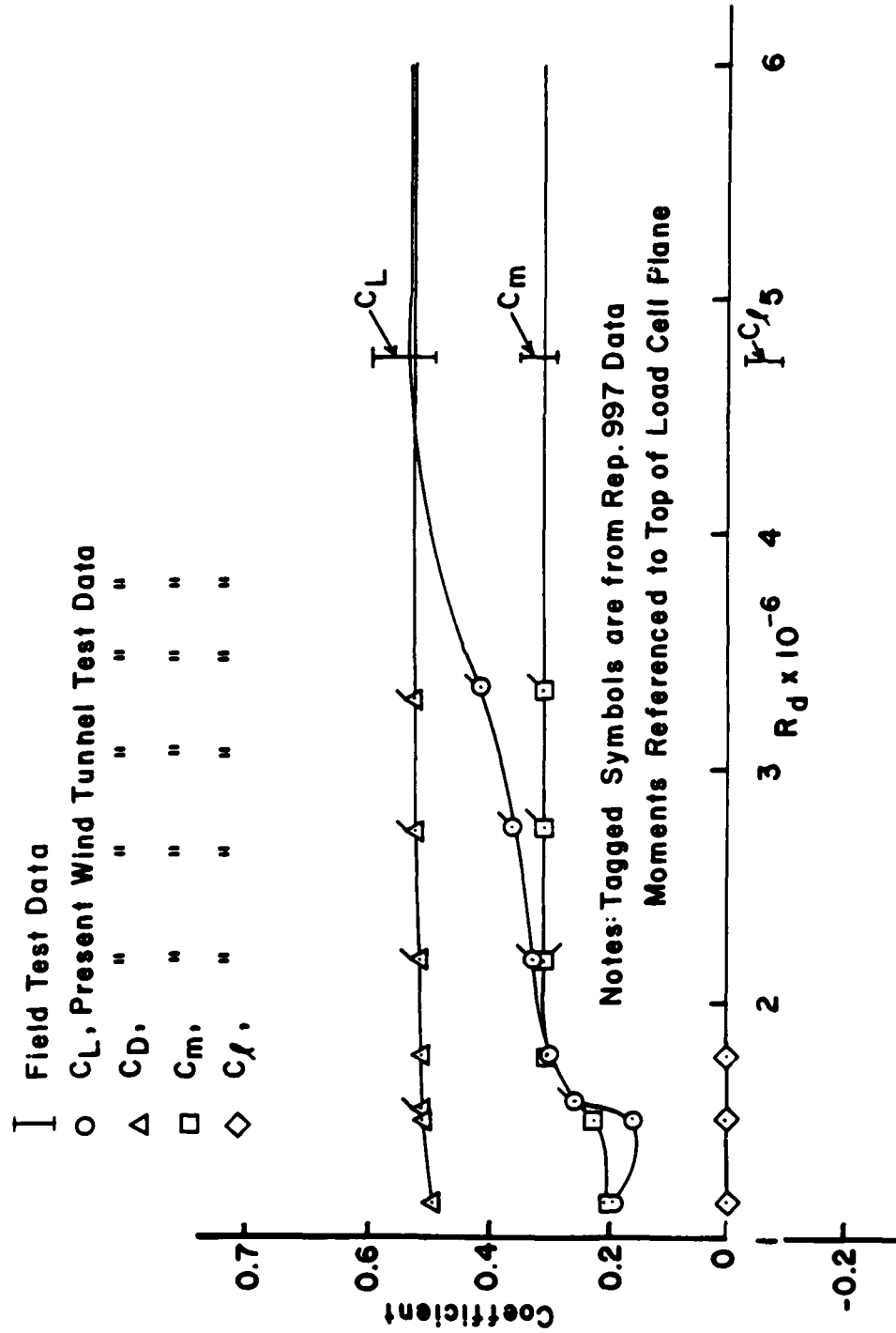


FIGURE 2-1. WIND TUNNEL AND FIELD TEST DATA COMPARISON AT $\psi = 0$ DEGREES

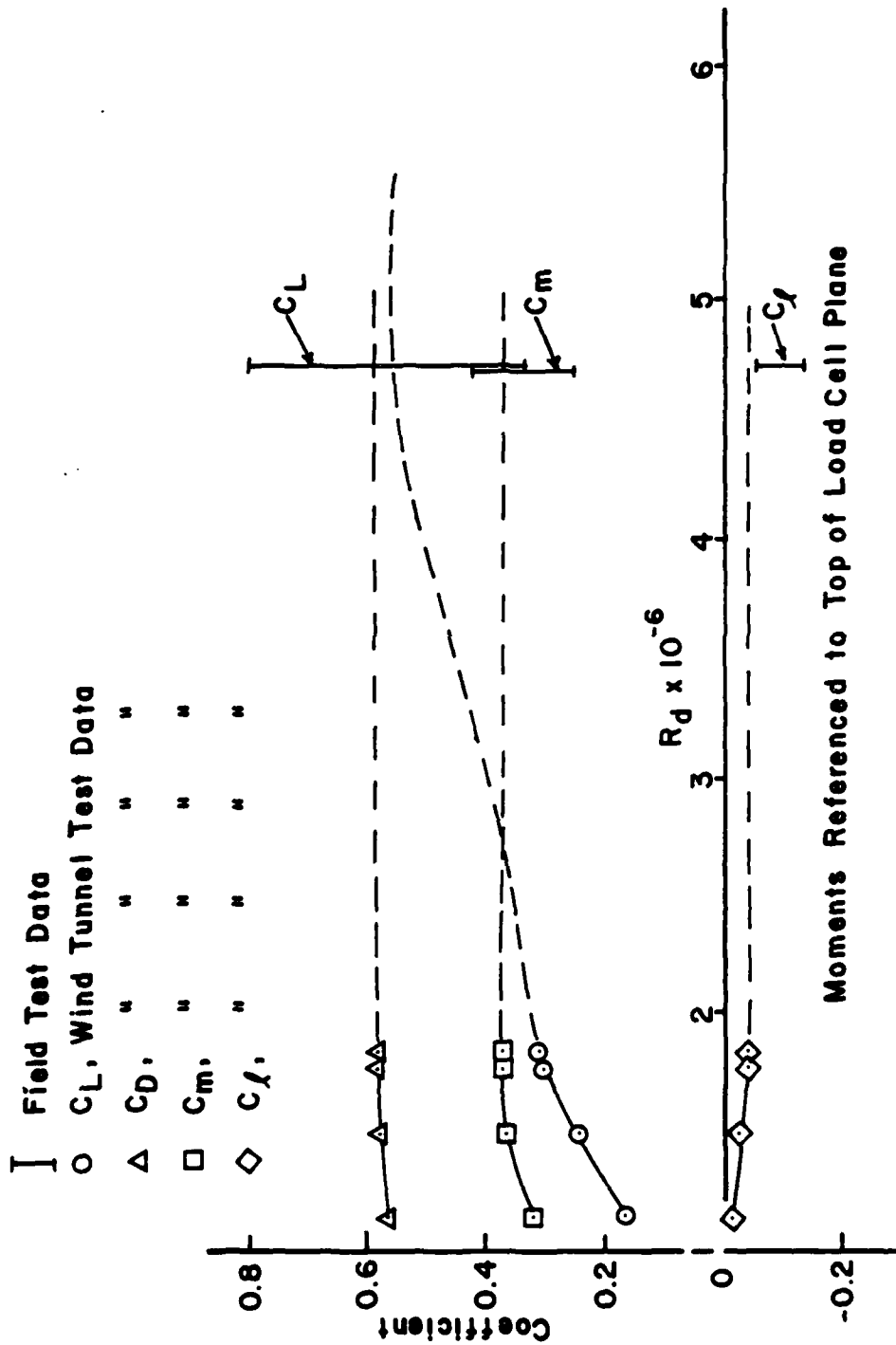


FIGURE 2-2. WIND TUNNEL AND FIELD TEST DATA COMPARISON AT $\psi = 2.3$ DEGREES

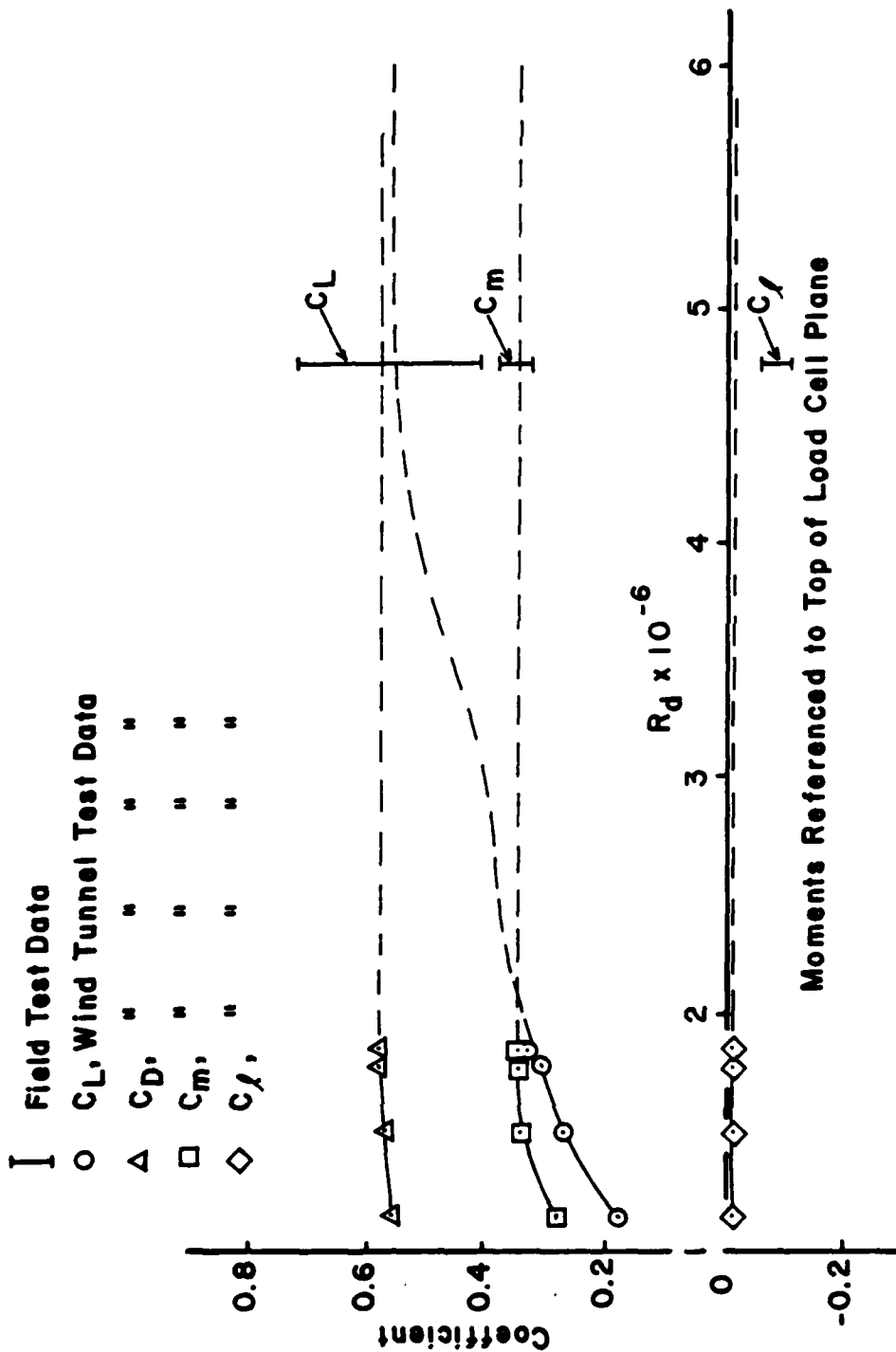


FIGURE 2-3. WIND TUNNEL AND FIELD TEST DATA COMPARISON AT $\psi = -3.6$ DEGREES

could not be reduced because the mean velocity approaching the tower and radome was indeterminate.

The wind tunnel test data indicate that the airloads acting on the rotadome vary substantially over the wind-angle $0^\circ \leq \psi \leq 22.5^\circ$, and while the initial wind tunnel data for the FAATC tower and rotadome configuration were recorded only at $\psi = 0^\circ$, 22.5° and 45° , field test data were measured for a great number of wind directions between $\psi = -16^\circ$ and $\psi = +5^\circ$. The great majority of the useful field test data, however, was recorded with either $\psi = -3.6^\circ$ or $\psi = 2.3^\circ$, within approximately $\pm 0.7^\circ$. A smaller portion of the useful field test data was recorded with $\phi \doteq 0^\circ$. To have a larger data base for comparison, additional wind tunnel tests were conducted after completion of the field tests at $\psi = -3.6^\circ$ and $\psi = 2.3^\circ$.

The data in Figures 2-1 through 2-3 are defined in the nomenclature, and indicate that all of the data except the lift-force coefficient, C_L , are reasonably flat with Reynolds number, R_d . Note that, except for C_L , the data change very little with R_d for $R_d > 1.75 \times 10^6$, and therefore these data could easily be extrapolated out to the R_d value of 4.75×10^6 encountered during the field tests. The C_L data recorded during the wind tunnel tests, however, were found to be quite dependent upon R_d , or at least test velocity, since the flow angularity caused by the tower presence was strongly affected by this parameter. The C_L data could not have been extrapolated to the higher R_d values without the help of the field test data. The C_L data, however, do not appear materially to affect the moment data, and the value of the lift force, even when extrapolated to an equivalent 130-mph wind speed, is not substantially greater than the static weight of the full-scale rotadome. For this reason, the non-linear behavior of C_L vs. R_d in the range of the wind tunnel tests is not considered serious. The drag (C_D) data are presented only to show their behavior with Reynolds number since these data could not be obtained during the field tests.

It is generally conceded that the force acting in a horizontal plane on a bluff body is more reliably measured in a wind tunnel than are the moments acting on the same body. The fact that the pitching-moment data taken in the wind tunnel agree with those recorded during the full-scale field tests suggests that the wind tunnel-measured horizontal force data are also reliable.

The rolling-moment data (C_ℓ) taken from the field test recording charts are consistently more negative than comparable data from the wind tunnel tests. It is believed that two factors contributed to this difference in the C_ℓ data. First, the position of the rotadome support legs relative to the tower was different for the field and wind tunnel test configurations. The R_{120} field test leg was more closely normal to the airstream than any of the legs on the wind tunnel model. Second, it is believed that there existed a small voltage output from the R_{120} load cell at zero load during the field tests. This would result in a consistent negative shift in C_ℓ without much affecting the C_m data since this leg was very nearly in the plane where C_m was referenced. The effect of this zero offset on C_L would, of course, tend to modify the C_L values presented on Figures 2-1 through 2-3. The scatter in the field test C_L data, however would tend to mask this affect.

The wind tunnel data presented on Figures A-14, and A-18 through A-25 in Appendix A were used to determine the steady-state loads which would be transmitted into the roofs of the various test towers due to steady winds acting on the test radomes. Data recorded from the rotadome model were extrapolated to full-scale, high-wind Reynolds numbers using the data on Figure A-26, and assuming that C_D and C_m are invariant for $R_d > 2.5 \times 10^6$. A similar extrapolation was performed for the spherical and teacup radomes using Figure A-27, and assuming C_D and C_m to be invariant for $R_d > 2.0 \times 10^6$. In each case, data from the wind tunnel tests were used which resulted in the largest loads measured for the tower and radome configurations.

These predicted full-scale airloads are presented in Table 2-1 for each tower and radome combination, together with the test yaw angle for which the data were acquired. Wind velocities considered are 60, 95, and 130 mph. The loads were calculated from the relations.

$$\text{Resultant shear force} = \frac{\rho}{2} V^2 A \left(C_D^2 + C_C^2 \right)^{1/2}$$

$$\text{Resultant overturning moment} = \frac{\rho}{2} V^2 A d \left(C_m^2 + C_\ell^2 \right)^{1/2}$$

where the air density, ρ , was taken to be for standard-day, sea-level conditions.

The angle relative to the approaching wind at which these loads act is given by

$$\tan^{-1} \left| \frac{C_C}{C_D} \right| \text{ and } \tan^{-1} \left| \frac{C_\ell}{C_m} \right|, \text{ respectively.}$$

There are three cases in Table 2-1 where the loads do not act in a plane parallel with the approaching wind (i.e., C_C and $C_\ell \neq 0$). For these cases, the angles at which the loads are acting relative to the oncoming wind are given in the footnotes.

It is quite possible that for some wind angles, not tested, the cross-wind force and rolling moment would contribute a much more substantial portion of the total air loads than those found at the selected test angles. In these cases, the loads would act at much greater angles relative to the oncoming wind. The comparative results presented in Table 2-1 should not be much affected however.

TABLE 2-1. TOWER-ROOFTOP LOADS PREDICTED FOR VARIOUS TEST RADOMES

Tower	Steady Wind Velocity, (mph)	ASDE-3 (Rotadome)		ASDE-2 (Spherical)		Teacup	
		Shear force, (lb)	Overturning moment, (ft-lb)	Wind angle, deg.)	Shear force, (lb)	Overturning moment, (ft-lb)	Wind angle, (deg.)
NAFEC	60	523	6403		1090	8838	1068 14773
	95	1312	18050	22.5 ¹⁾	2733	22155	2676 37032 45
	130	2457	30058		5118	41491	5012 69350
Pel	60	601	8017		1296	9676	1176 16428
	95	1506	20095	36	3249	24254	2948 41179 18 ³⁾
	130	2820	37633		6085	45421	5520 77112
Welton Beckett	60	474	6325		1114	9303	1106 16066
	95	1188	15855	45	2794	23321	22.5 and 45
	130	2225	29692		5232	43674	2773 40272 5192 75418

1) Shear load acting at 2.4° and overturning moment at 2.2° relative to wind.

2) Shear load acting at 16.8° and overturning moment at 9.7° relative to wind.

3) Shear load acting at 3.8° and overturning moment at 8.4° relative to wind.

3. REMARKS AND CONCLUSIONS

The loads data in Table 2-1 show dramatically how these loads are dependent upon the square of velocity, increasing by a factor of 4.7 between a 60- and a 130-mph wind. General conclusions which may be drawn from this table are as follows:

1) The shear forces from the spherical and teacup radomes are approximately twice as large as those from the rotadome.

2) The overturning moment, on the average, is 25 percent greater for the spherical and 56 percent for the teacup radome than for the rotadome.

These results are primarily due to the much larger projected frontal areas of the spherical and teacup radomes compared with the rotadome. The large overturning moments measured for the teacup radome are due to the teacup overhang which is effectively at an angle of attack due to tower-induced flow angularity.

3) The highest loads on each of the radomes were measured when they were coupled with the Pei tower, and the smallest loads were measured when the radomes were mounted on the Welton Beckett or FAATC towers.

This is because the upper portion of the Pei tower was smaller than the other two towers, and therefore, has less influence on the airstream striking the radomes. The larger towers result in a substantial region above the tower where there is little air movement due to flow separation. The lower portions of the radomes were, therefore, shielded from the airstream when mounted atop the larger towers.

For all towers tested, a shear layer existed resulting from the flow up the windward face of the tower and the accelerated free-stream flow over the tower. These shear layers contain velocities which are greater than free stream and strike the radomes, resulting in airloads higher than would be accounted were the radomes tested alone in free air. This is best evidenced

by the spherical radome which would have a drag coefficient of approximately 0.25 in free air at the test Reynolds numbers, yet drag coefficients greater than 0.5 were measured during these tests.

During the field tests, data were recorded both with the rotadome stationary and with the rotadome revolving in its normal operational manner of 60 rpm. Results of these tests were essentially the same with and without rotadome rotation, within data scatter. It is concluded from these results that any effects of rotadome rotation on the airloads acting on it are negligibly small.

Appendix A data indicate that radome details close to the tower roof; for example, the location of the rotadome drive motor or supporting legs, make only a small difference in the airloads measured. The airloads do, however, depend in large measure on the tower geometry and the wind direction relative to the tower. This is due to the strong influence the tower geometry has on both vertical airflow angularity over the radome and the region of the airflow separation over the tower roof. The data also suggest that any radome should be mounted as close to the tower roof as possible to minimize the overturning moment which is caused primarily by the horizontal wind loading.

As previously stated, the wind tunnel tests were conducted under steady airstream conditions without any attempt to represent a vertical velocity gradient such as might be encountered in the field. The field tests were conducted with the wind approaching the test tower from across an open airport field which provided a long stretch without obstacles to the wind approaching the tower. The effects of terrain and adjacent buildings could have a large effect on the radome airloads, and, as shown, tower geometry and wind-approach angles have large effects.

The unsteady winds encountered during the field tests did not seem to have a large effect on the overall airloads measured, at least for the few wind angles which could be checked. It is

quite possible, however, to have local, time-dependent peak pressures acting on curved surfaces in unsteady winds which are three times greater than found in steady winds. The integrated unsteady pressures from a curved body in unsteady flow, resulting in overall loads, are generally no greater at the time that the peak pressure was recorded than the overall loads measured in steady flow however. Since very little data of this type exists, the safe assumption is that the peak unsteady loads will, in general, be greater than measured steady-state loads.

APPENDIX A

WIND TUNNEL TESTS

INTRODUCTION

This appendix presents the results of wind tunnel tests conducted on 1/12-scale models of three types of airport tower-mounted radomes. The three radomes tested are for use with ground-search-type radar antennas which are used to determine the location and movement of aircraft and vehicles on airport runways and adjacent areas. The radomes tested are described in the nomenclature section, and are referred to as (1) Rotadome, (2) Spherical, and (3) Teacup. Each of these radomes was tested mounted atop three different styles of airport tower. The towers, represented in 1/12-scale, are also described in the nomenclature section, and include the FAATC tower patterned after the tower at FAATC, New Jersey, where the full-scale field tests were conducted; the Pei tower, similar to the Pei-designed tower at Chicago's O'Hare airport; and the Welton Beckett tower, similar to the Welton Beckett-designed tower at the Dallas-Fort Worth airport.

The primary purpose of these tests was to determine the airloads acting on each of the radomes and the effects of tower geometry on these airloads. These data are intended to be useful in specifying the structural loads on an airport tower roof carrying a radome subjected to wind forces.

Test Setup

The 1/12-scale tower models were constructed to represent the upper 56 feet of the full-scale towers. These tower models were attached to the non-metric yaw turntable in the ceiling of GALCIT (Graduate Aeronautical Laboratories, California Institute of Technology) 10-foot wind tunnel test section. Each tower was constructed with a hollow center, such that a strut from the external balance system located above the yaw turntable could pass through the tower with the free end of the strut attached to the

radome under test. In this manner, each radome model was positioned as though it were attached to the tower roof, however, physical contact between radome and tower models was carefully avoided by a small airgap between the two. A ground-detection system was installed in each tower model to ensure that neither the radome nor its support strut touched the tower under airloads. The technique permitted the direct measurement of the airloads acting on the radome alone in the proximity of the tower.

The general layout and dimensions of the GALCIT 10-foot wind tunnel are given in Figure A-1. Photographs of each test tower mounted on the yaw turntable are presented in Figures A-2 through A-6, and photographs of each tower and radome configuration are shown in Figure A-7 through A-13.

Data Acquisition and Reduction

Because the tower models were large compared with the cross-sectional area of the wind tunnel test section, it was not possible analytically to correct the wind tunnel airstream velocity for the blockage effects of these tower models. An airstream-velocity calibration was, therefore, performed with each tower model present and at each tower angle relative to the airstream using a standard pilot-static probe. These calibration data were then corrected for the blockage effects of each radome model which caused an increase in airstream velocity due to Bernoulli's principle. This correction, which accounts for the increased velocity due to an effective reduction in test section area, is given by the following formula:

$$\epsilon = \frac{1}{4} \frac{A}{S_0} ,$$

where ϵ (the incremental velocity correction) is the sum of a solid blockage factor, dependent on the projected frontal area of the radome model (A), and a wake-blockage factor. S_0 is the tunnel cross-sectional area minus the cross-sectional area

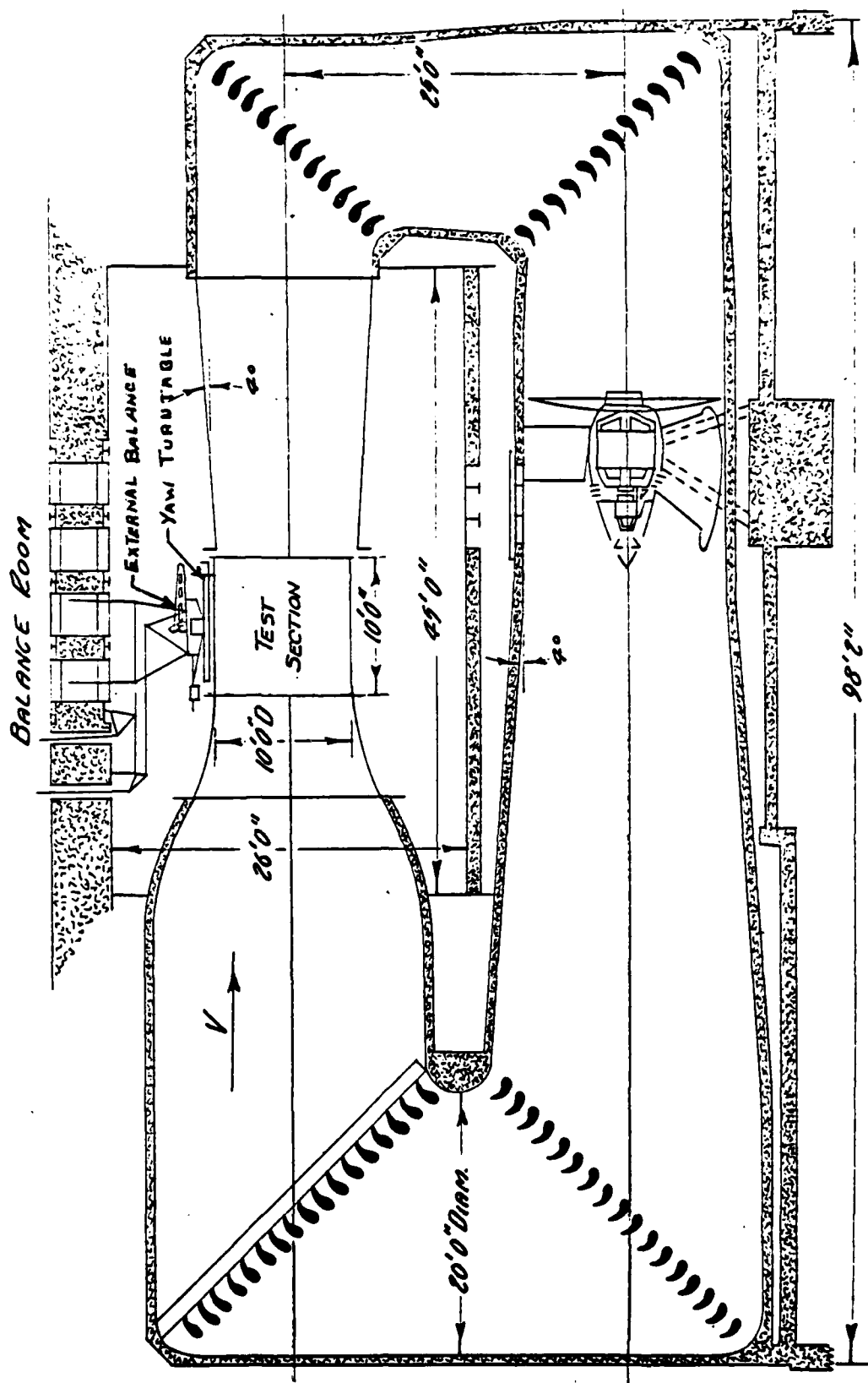
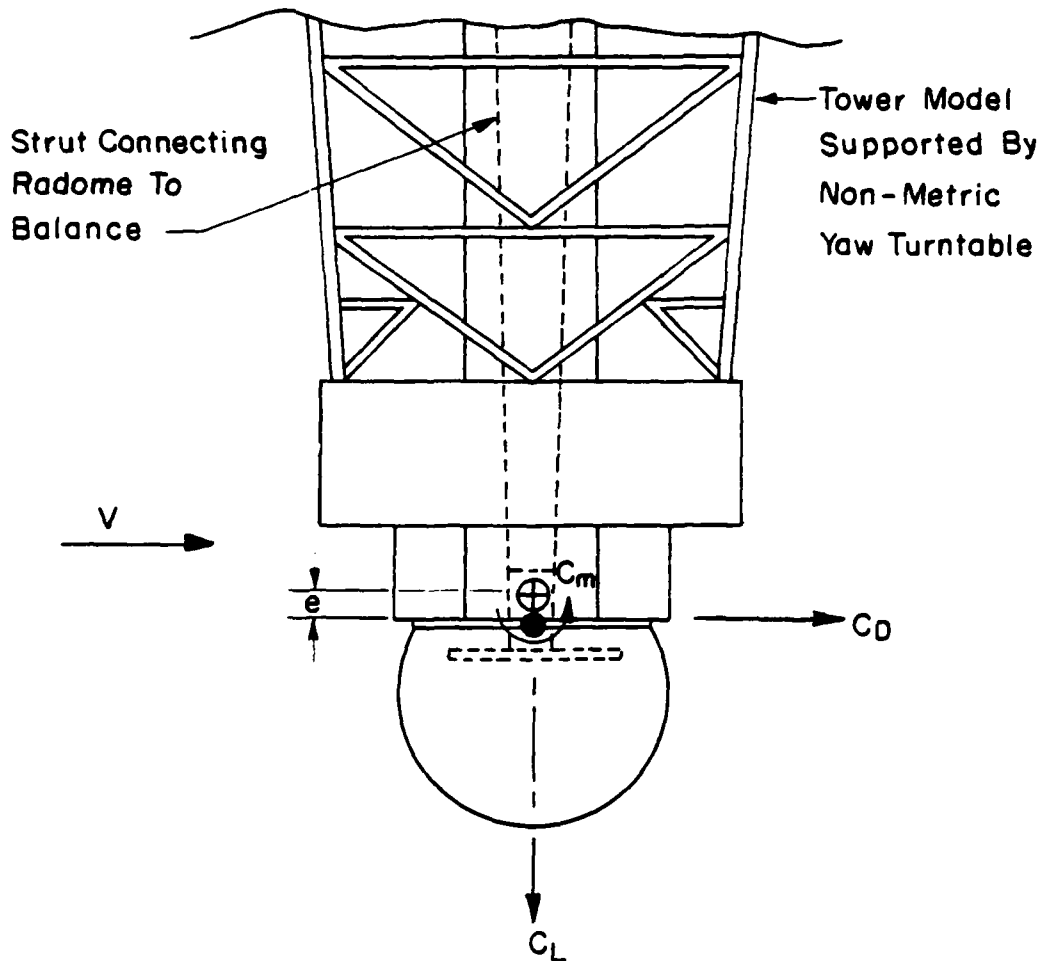


FIGURE A-1. VERTICAL SECTION THROUGH TEN-FOOT WIND TUNNEL. TWO-PARAMETER SIX COMPONENT SUSPENSION SYSTEM

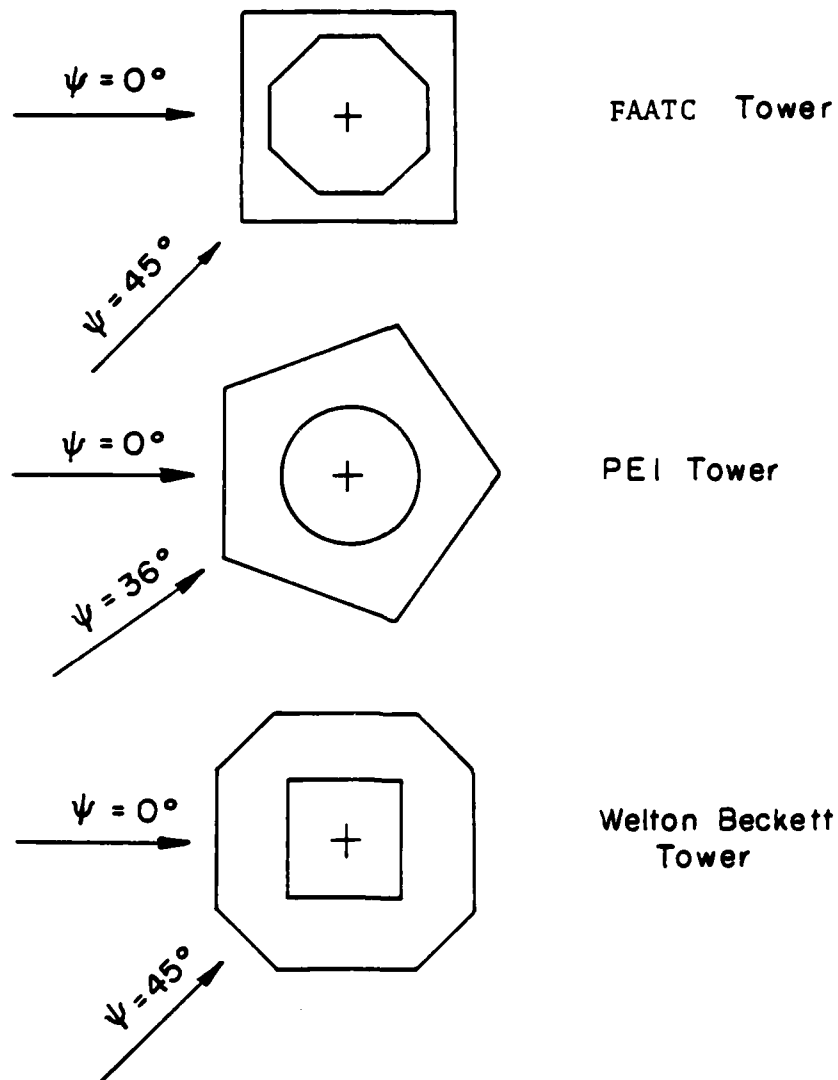
⊕ Virtual Center Of
Balance System

● Moment Reference Center



View Shown As Installed In Wind Tunnel
(FAATC Tower, Spherical Antenna Shown)

FIGURE A-2. LOADS AND MOMENT TRANSFER



Planform Views Shown With
Yaw Angle Range For Each Test
Tower

FIGURE A-3. TOWER YAW ANGLES

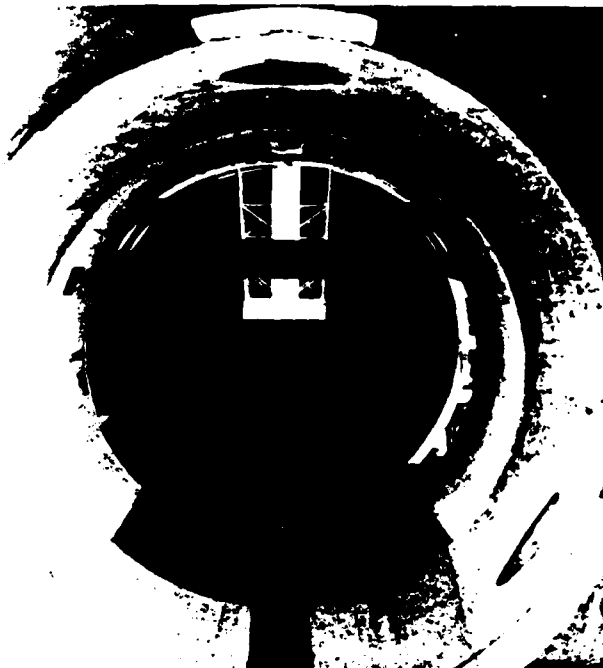


FIGURE A-4a. FAATC TOWER MODEL WITH $\psi = 0^\circ$

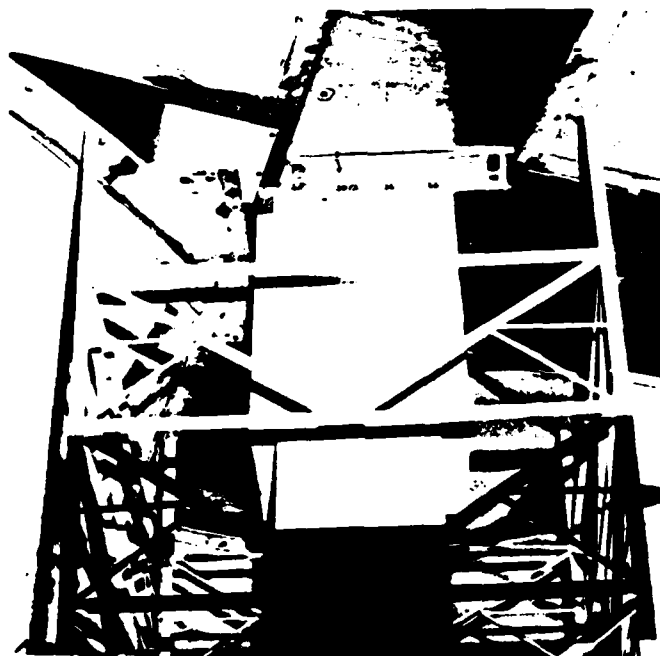


FIGURE A-4b. ATTACHMENT OF FAATC TOWER
TO NOMETRIC YAW TURNTABLE

FIGURE A-4. FAATC TOWER MODEL AND TOWER
INSTALLATION IN WIND TUNNEL

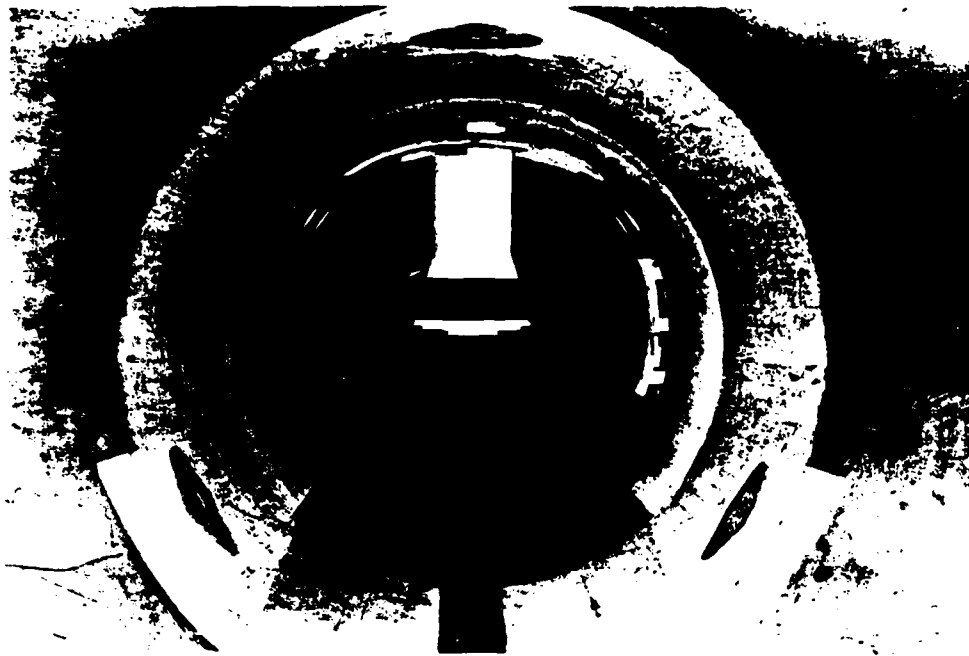


Fig. A5a Pei tower model with $\psi = 36^\circ$



Fig. A5b View showing top detail of Pei tower model

FIGURE A-5. PEI TOWER MODEL



Fig. A6a Welton Beckett tower with $\psi = 22.5^\circ$

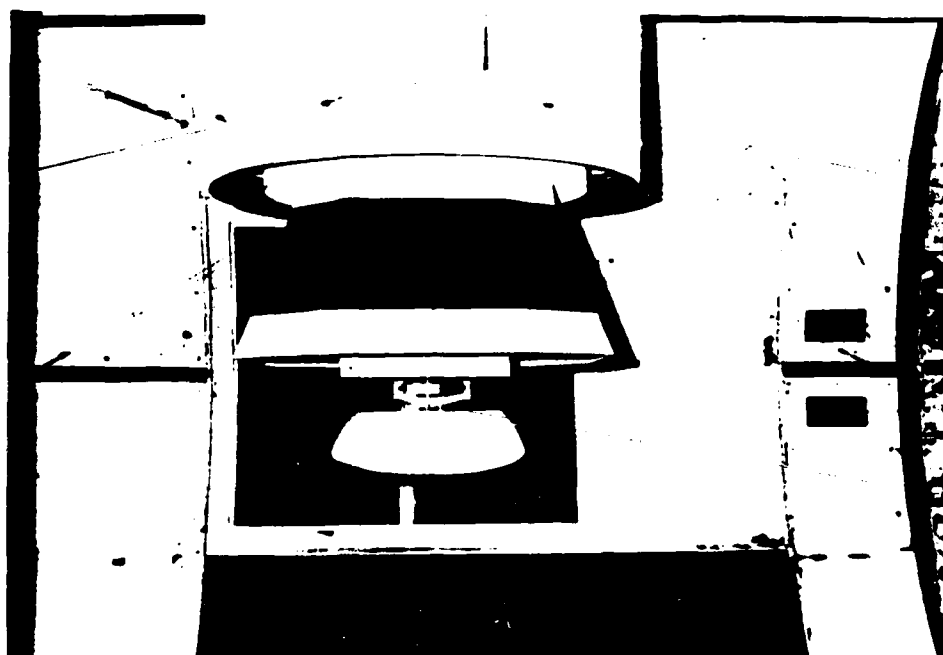


Fig. A6b View showing top detail of Welton Beckett tower model

FIGURE A-6. WELTON-BECKETT TOWER MODEL

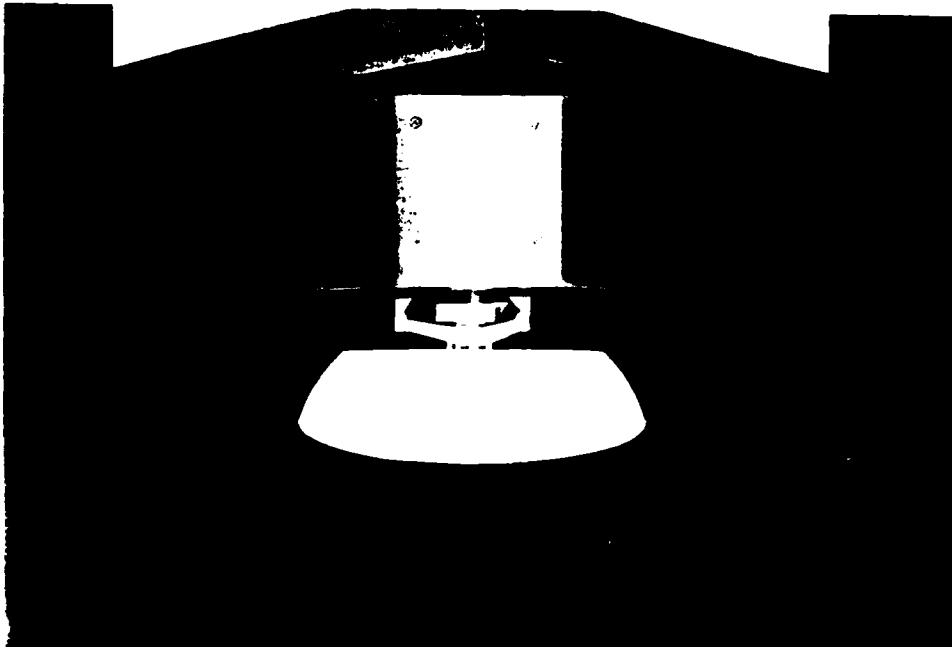


FIGURE A-7a. ROTADOME MODEL ON FAATC TOWER AT $\psi = 45^\circ$
WITH ROTADOME DRIVE MOTOR AFT

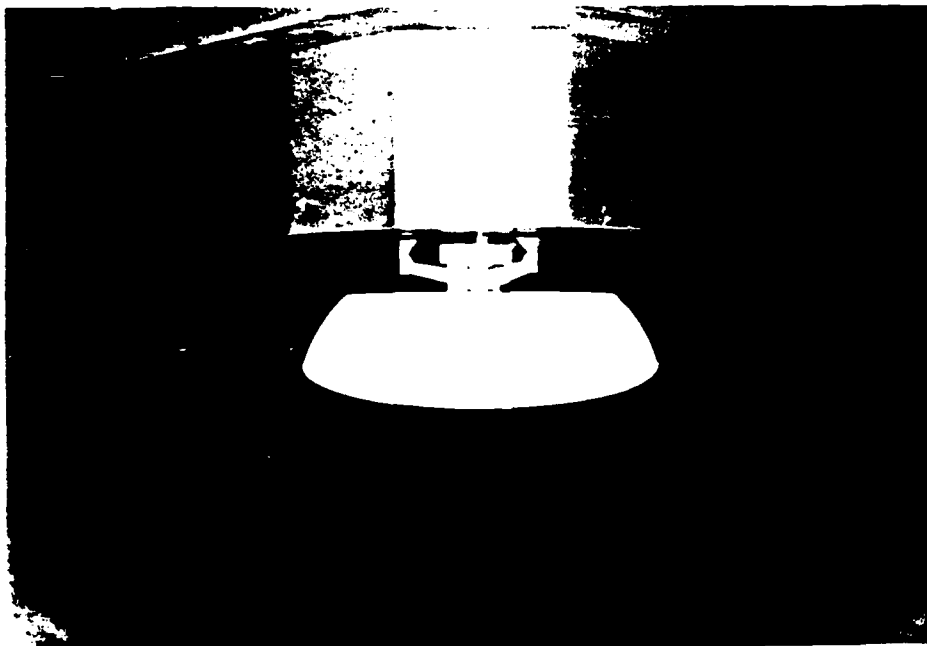


FIGURE A-7b. ROTADOME MODEL ON FAATC TOWER AT $\psi = 45^\circ$
WITH ROTADOME DRIVE MOTOR FORWARD

FIGURE A-7. ROTADOME MODEL



FIGURE A-8a. ROTADOME WITH SIMULATED LAP JOINTS ON
FAATC TOWER WITH $\psi = 22.5^\circ$

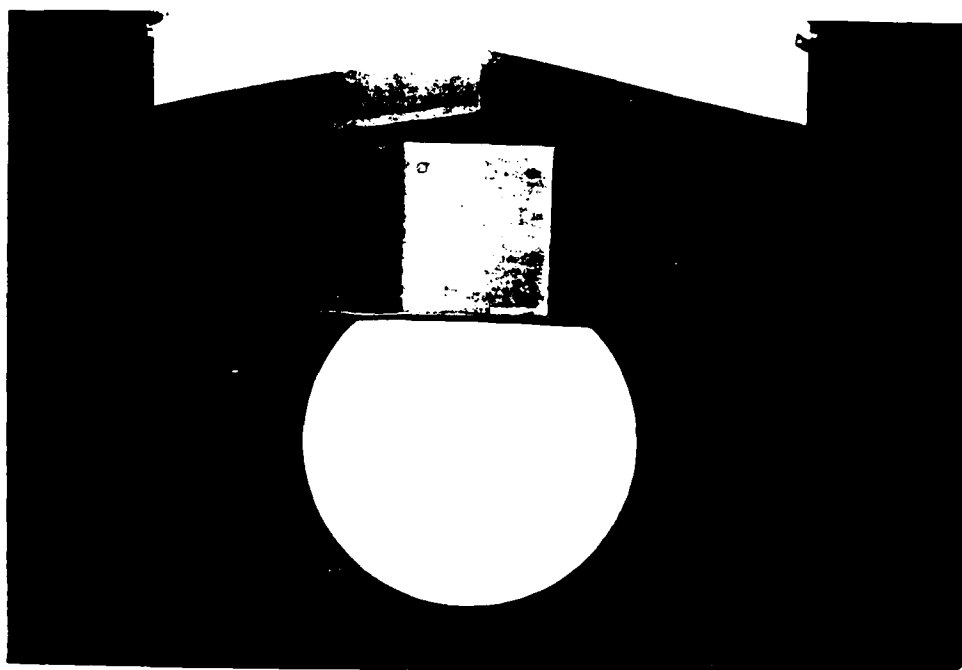


FIGURE A-8b. SPHERICAL RADOME ON FAATC TOWER WITH $\psi = 45^\circ$

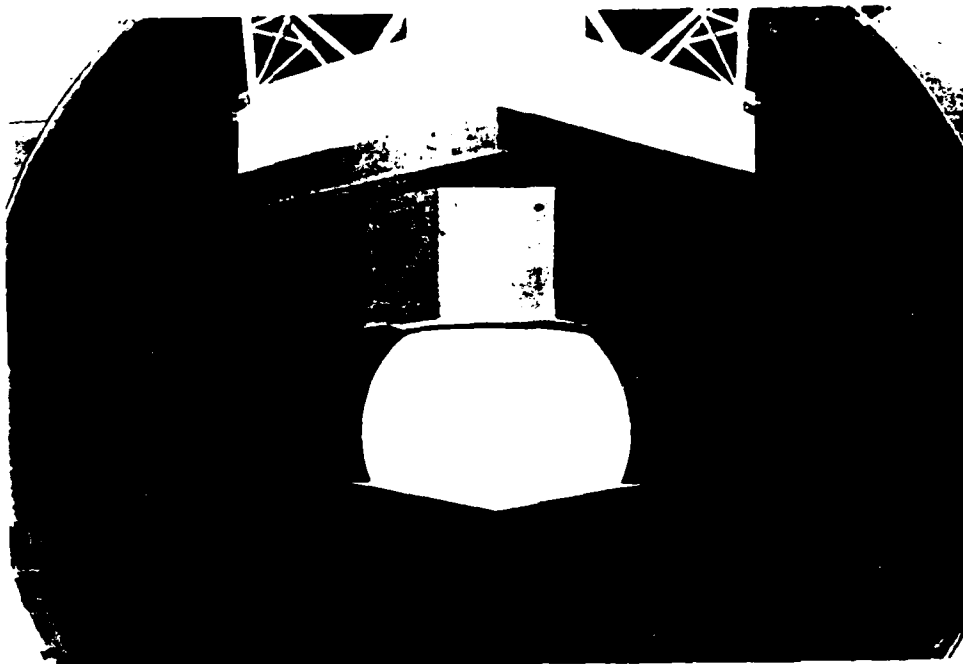


FIGURE A-9a. TEACUP RADOME ON FAATC TOWER WITH $\psi = 45^\circ$

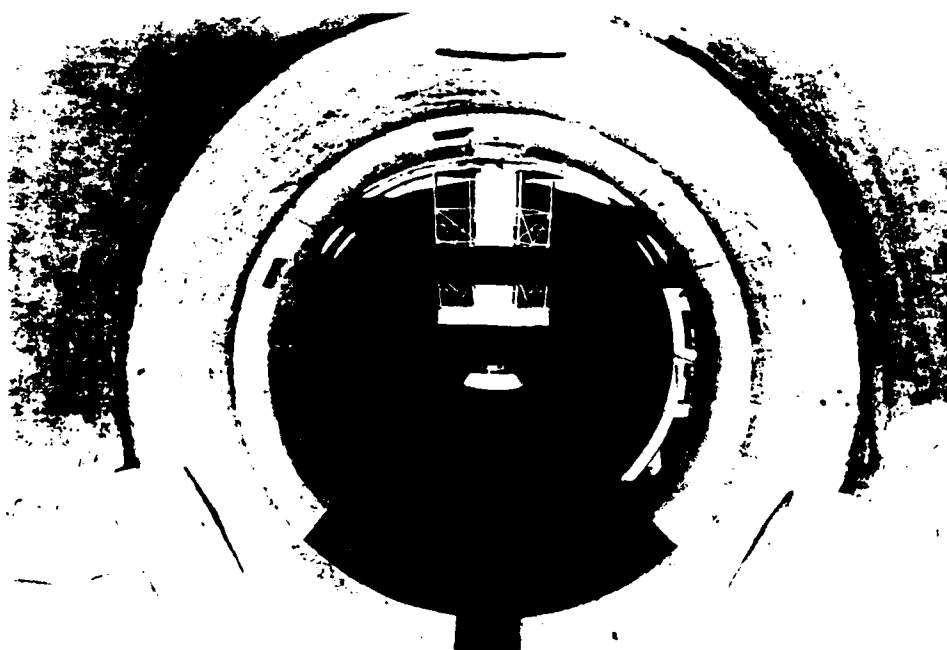


FIGURE A-9b. ROTADOME ON FAATC TOWER WITH $\psi = 22.5^\circ$

FIGURE A-9. TEACUP RADOME MODEL AND ROTADOME
MODEL ON FAATC TOWER

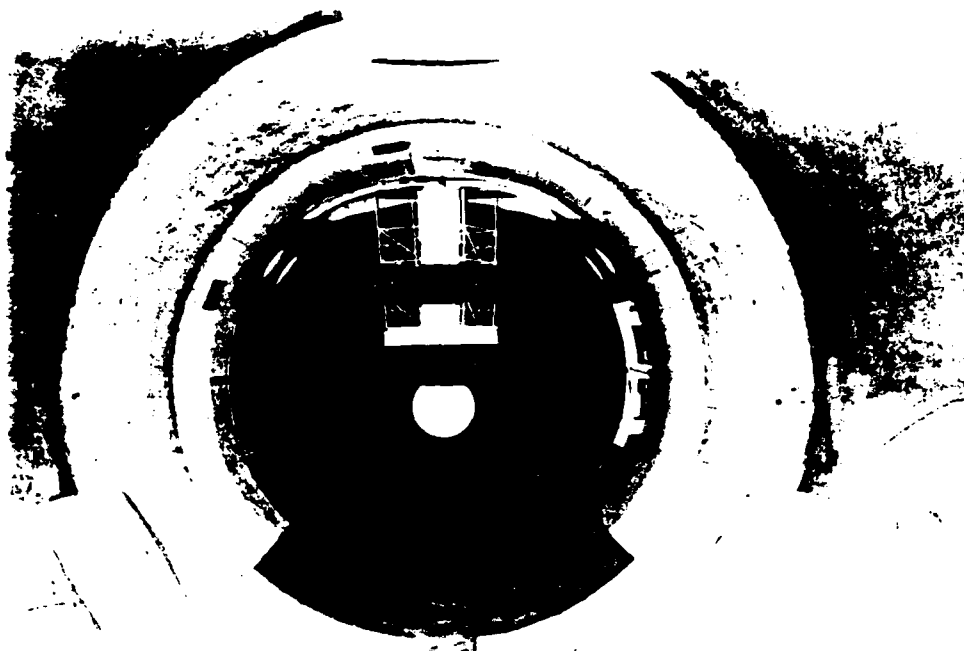


FIGURE A-10a. SPHERICAL RADOME ON FAATC TOWER WITH $\psi = 22.5$



FIGURE A-10b. TEACUP RADOME ON FAATC TOWER WITH $\psi = 22.5^\circ$

FIGURE A-10. SPHERICAL AND TEACUP RADOME MODELS ON FAATC TOWER

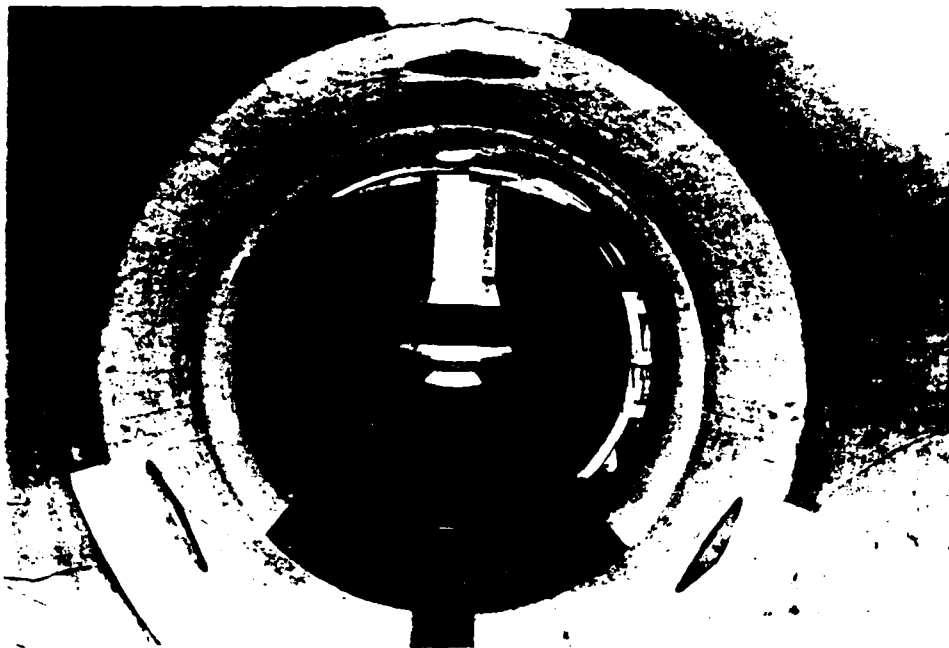


Fig. Alla Overall view of rotadome on Pei tower with $\psi = 0^\circ$

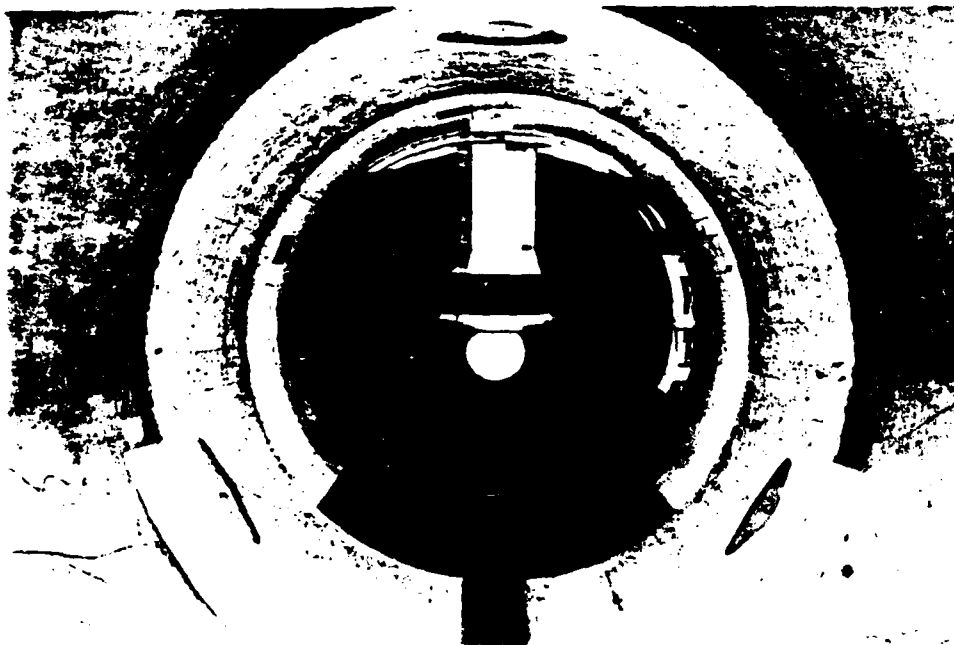


Fig. Allb Overall view of spherical radome on Pei tower with $\psi = 0^\circ$

FIGURE A-11. ROTADOME AND SPHERICAL RADOME MODELS ON PEI TOWER

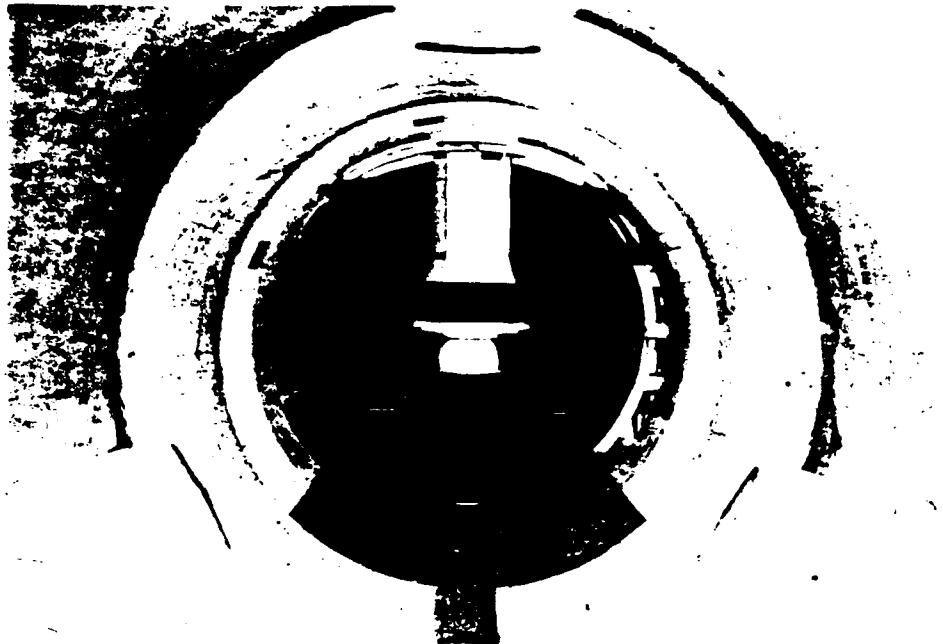


Fig. A12a Overall view of teacup radome on Pei tower with $\theta = 0^\circ$

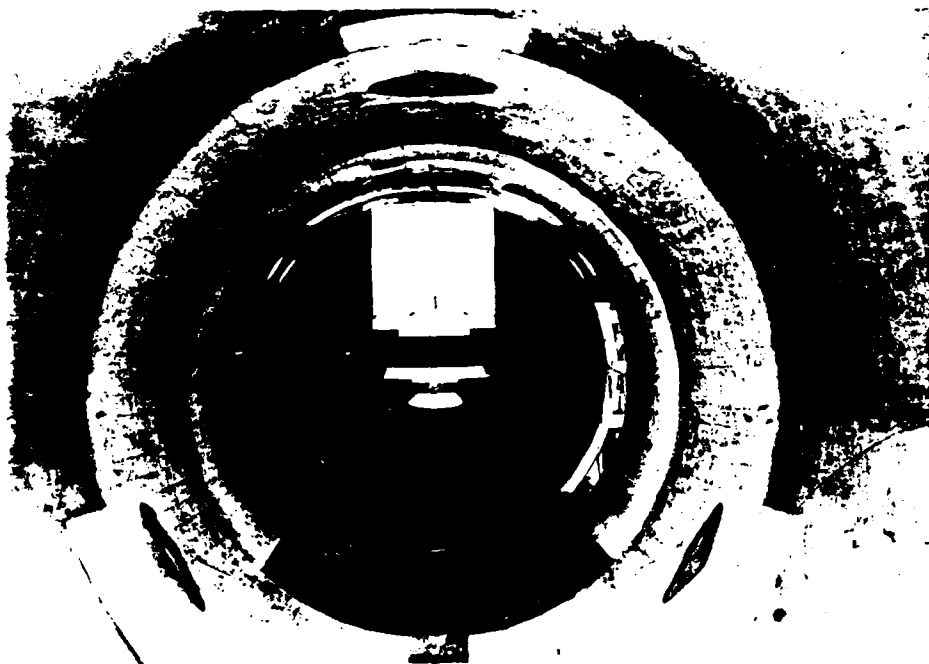


Fig. A12b Overall view of rotadome on Walton Beckett tower with $\theta = 0^\circ$

FIGURE A-12. TEACUP RADOME MODEL ON PEI TOWER AND
ROTADOME MODEL ON WELTON-BECKETT TOWER

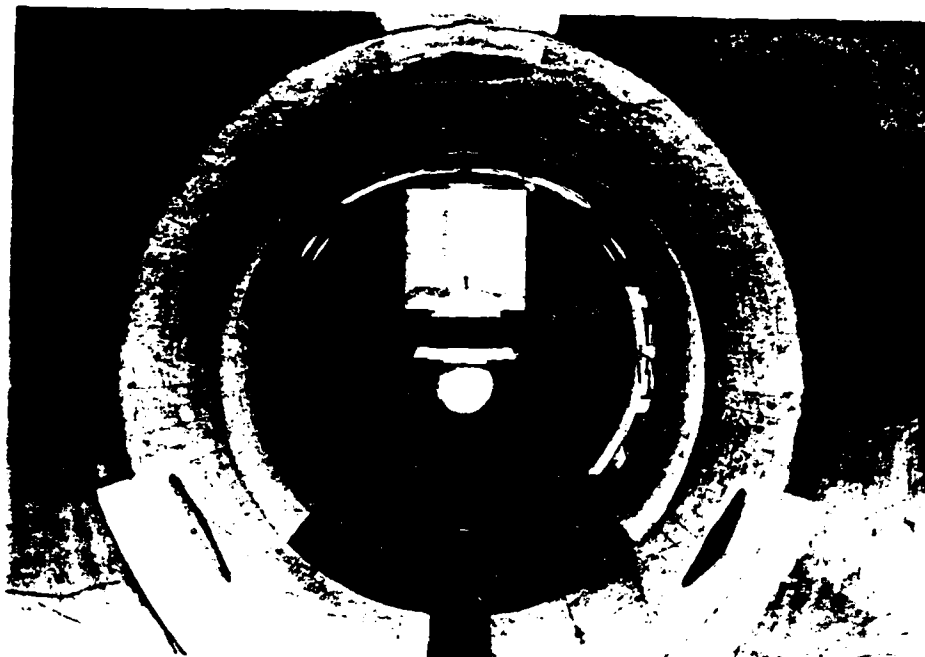


Fig. A13a Overall view of spherical radome on
Welton Beckett tower with $\psi = 0^\circ$

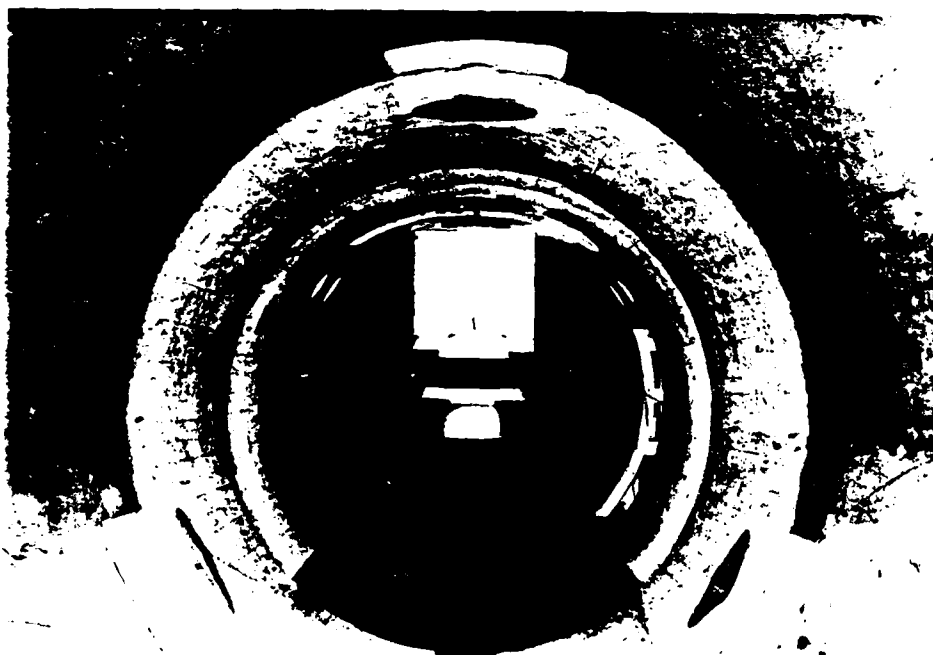


Fig. A13b Overall view of teacup radome on
Welton Beckett tower with $\psi = 0^\circ$

FIGURE A-13. SPHERICAL AND TEACUP RADOME
MODELS ON WELTON-BECKETT TOWER

minus the cross-sectional area occupied by the tower model.

The data acquired during these tests include radome aerodynamic lift, drag, cross-wind force, pitching moment, and rolling moment. A few measurements of the tower-induced flow angularity just upstream of the radomes were also made using a 5-inch long strand of darning cotton attached to the end of a probe.

Data were collected at a minimum of three airstream velocities for each test configuration. The test airstream velocities and the resulting airstream dynamic pressures and Reynolds numbers for each radome are given in Table A-1.

Since each of the radome models was essentially symmetrical, it was not necessary to test these models at more than one angle relative to the airstream. The tower-model geometry, however, was known to have a strong influence on the radome airloads, and therefore, it was necessary to investigate the radome airloads for various tower orientations relative to the airstream. For each tower configuration, three yaw angles were selected for the tests. These angles are given on the data plots in the figures of this appendix, and the yaw angle ranges are given in Figure A-3.

The force and moment data have been reduced to the dimensionless coefficients defined in the nomenclature. These coefficients are useful in that their values are essentially invariant above some critical Reynolds number, and therefore, may be applied at much higher Reynolds numbers than those encountered during these tests.

The positive sense of the main coefficients presented in this report is shown in Figure A-2. It will be noted that the drag or shear force acts along the plane of the tower-cab roof, and the moment also acts as roof levels on radome centerline.

The pitching moment is calculated from the measured data at the balance virtual center as follows:

$$C_m = C_{m_1} - \frac{e}{d} C_D, \text{ and the rolling moment is } C_\ell = C_{\ell_1} - \frac{e}{d} C_C,$$

TABLE A-1. AIRSTREAM DYNAMIC PRESSURE AND RADOME REYNOLDS
NUMBER VERSUS AIRSTREAM TEST VELOCITY

RADOME CONFIGURATION	V, mph	q, lb/ft ²	R _d × 10 ⁻⁶
Rotadome	94.5	21	1.14
	112.9	30	1.37
	123.7	36	1.50
	130.4	40	1.58
	145.8	50	1.77
	152.9	55	1.86
Spherical	94.5	21	1.22
	112.9	30	1.46
	123.7	36	1.60
	130.4	40	1.69
	145.8	50	1.89
Teacup	94.5	21	1.22
	112.9	30	1.46
	123.7	36	1.60
	130.4	40	1.69
	145.8	50	1.89

where C_m and C_{d1} are measured at the balance virtual center (see Figure A-2).

The model radome projected frontal area, A , and diameter, d , used to calculate the force and moment coefficients are given in Table A-2.

TABLE A-2. RADOME DIMENSIONS USED IN DATA REDUCTION

RADOME CONFIGURATION	A, ft^2	d, ft
Rotadome	0.6163	1.500
Spherical	1.8272	1.600
Teacup	1.4507	1.600

Wind Tunnel Test Results

Data from the force and moment tests are presented as dimensionless lift, drag, pitching-moment, rolling-moment, and cross-wind force coefficients as defined in the nomenclature. These data are presented in plotted form as a function of Reynolds number in Figures A-14 through A-25 and A-28. Each figure, where plotted data are presented, has been divided into either three or five subfigures for ease of reading. That is, Figure Aa shows lift coefficient values, Ab gives drag coefficient values, and Ac presents the pitching-moment coefficient values. Where the rolling-moment and cross-wind force coefficient values were non-zero, the data would be presented on Figures Ad and Ae, respectively.

Figures A-14 through A-19, and A-26 and A-28 show data recorded from the radome in proximity to the FAATC tower, the Pei tower, and the Welton-Beckett tower. Additional tests were conducted on the rotadome configuration in proximity to the FAATC tower for use in correlating the wind tunnel and field test data. These data are also presented in the aforementioned subfigure group. The results of the spherical radome tests in proximity

$\gamma = 0^\circ$, MOTOR FWD., RUN 19
 Δ " " " AFT. " 20
 Δ " = 22.5° , " FWD., " 3
 Δ " " " AFT., " 10
 Δ " = 45° , " FWD., " 1
 Δ " " " AFT., " 2

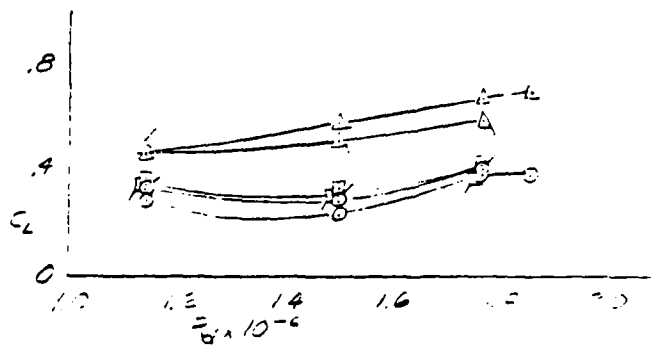


FIGURE A-14. FORCE AND MOMENT COEFFICIENTS FOR ROTADOME AT STANDARD HEIGHT ON FAATC TOWER

\circ $\theta = 0^\circ$, MOTOR FWD., RUN 19
 \circ " " " AFT., " 20
 Δ " $= 22.5^\circ$, " FWD., " 9
 Δ " " " AFT., " 10
 \square " $= 45^\circ$, " FWD., " 1
 \square " " " AFT., " 2

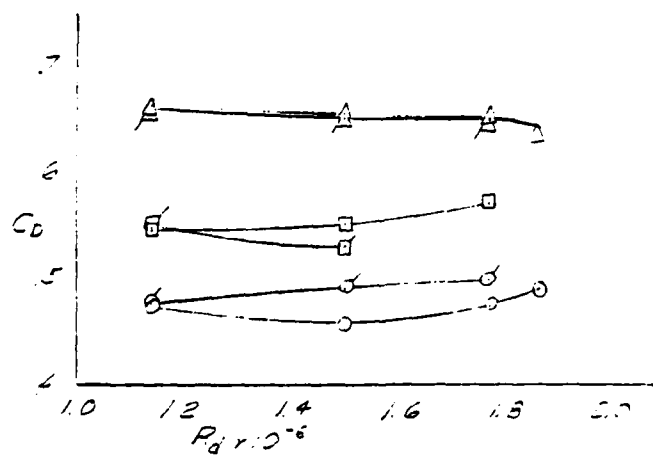


FIGURE A-14. FORCE AND MOMENT COEFFICIENTS FOR ROTADOME AT STANDARD HEIGHT ON FAATC TOWER (Continued)

○	$\psi = 0^\circ$	MOTOR FWD.	RUN 19
○	" = "	" AFT.	" 20
△	" = 22.5°	" FWD.	" 9
△	" = "	" AFT.	" 10
□	" = 45°	" FWD.	" 1
□	" = "	" AFT.	" 2

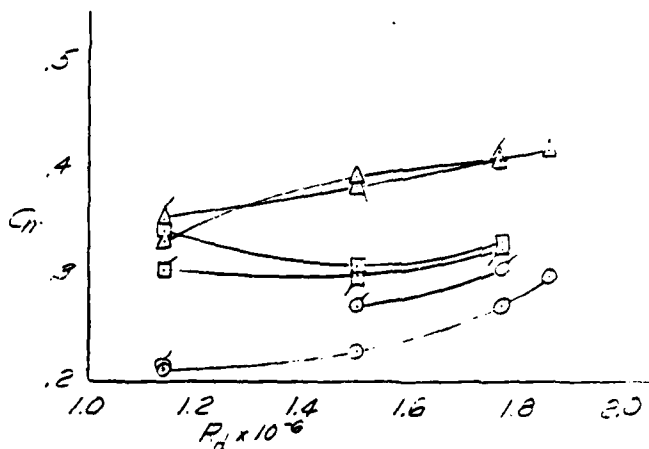


FIGURE A-14. FORCE AND MOMENT COEFFICIENTS FOR ROTADOME AT STANDARD HEIGHT ON FAATC TOWER (Continued)

$\Delta \gamma = 22.5^\circ$, MOTOR FUEL, RUN 9

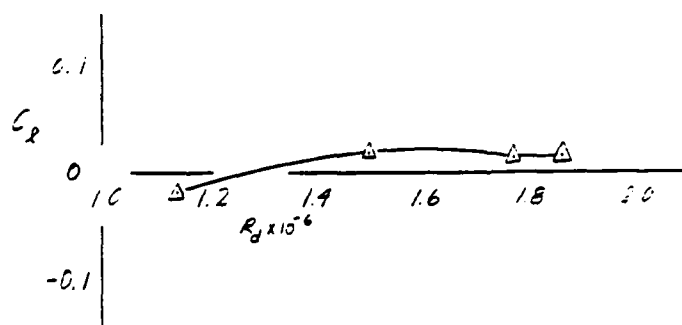


FIGURE A-14. FORCE AND MOMENT COEFFICIENTS FOR ROTADOME AT STANDARD HEIGHT ON FAATC TOWER (Continued)

$\Delta \psi = 22.5^\circ$, MOTOR FWD., RUN 9

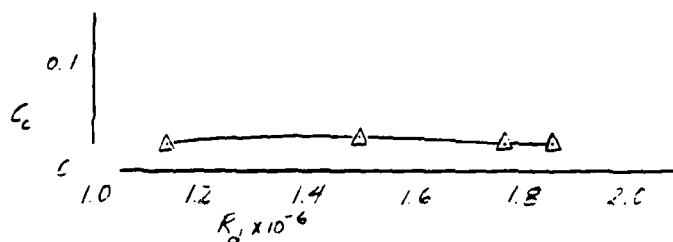


FIGURE A-14. FORCE AND MOMENT COEFFICIENTS FOR ROTADOME AT STANDARD HEIGHT ON FAATC TOWER (Continued)

MOTOR ATT.

O $\psi = 0^\circ$, RUN 18
 Δ " = 22.5° , " 11

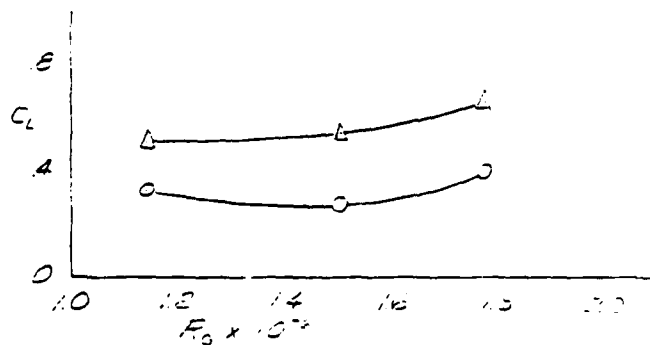


FIGURE A-15. FORCE AND MOMENT COEFFICIENTS FOR ROTADOME WITH SIMULATED LAP JOINTS ON FAATC TOWER AT STANDARD HEIGHT

MOTOR AFT.

○ $\psi = 0^\circ$ RUN 18
 Δ " $\psi = 22.5^\circ$, " 11

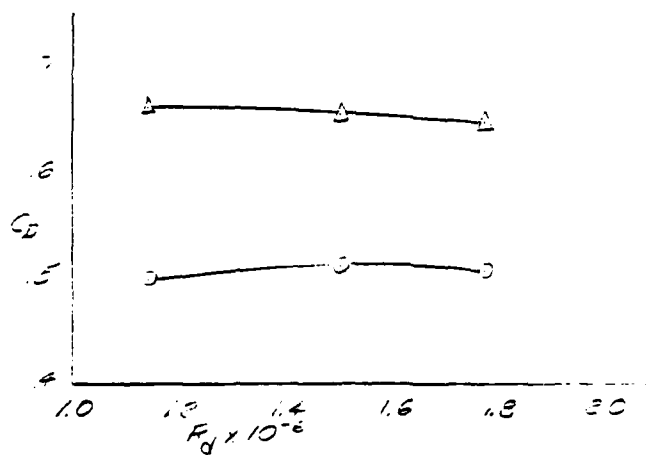


FIGURE A-15. FORCE AND MOMENT COEFFICIENTS FOR ROTADOME WITH SIMULATED LAP JOINTS ON FAATC TOWER AT STANDARD HEIGHT (Continued)

MOTOR NET

O $\psi = 0^\circ$, RUN 18
 Δ $\psi = 225^\circ$, " 11

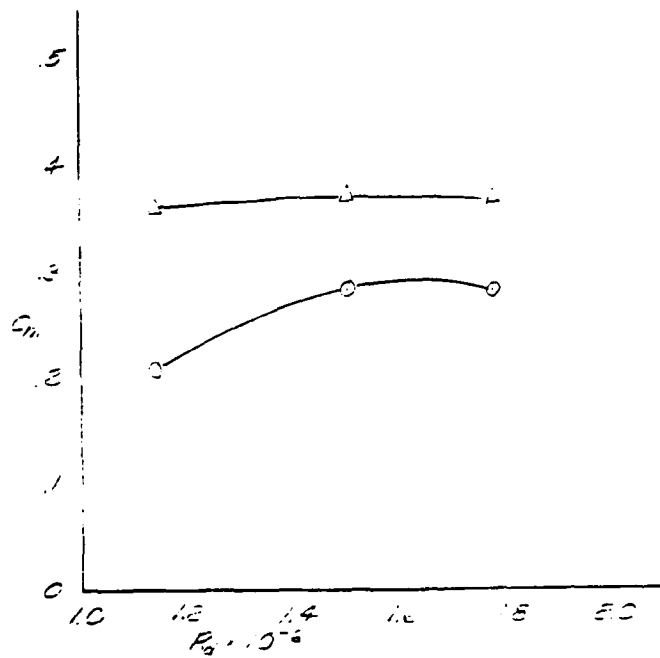


FIGURE A-15. FORCE AND MOMENT COEFFICIENTS FOR ROTADOME WITH SIMULATED LAP JOINTS ON FAATC TOWER AT STANDARD HEIGHT
 (Continued)

C $\psi = 0^\circ$, MOTOR FWD, RUN 15
 σ " " " AFT, " 16
 Δ " $= 22.5^\circ$ " " FWD, " 14
 \angle " " " AFT, " 13
 \square " $= 45^\circ$ " " FWD, " 4
 \boxminus " " " AFT, " 3

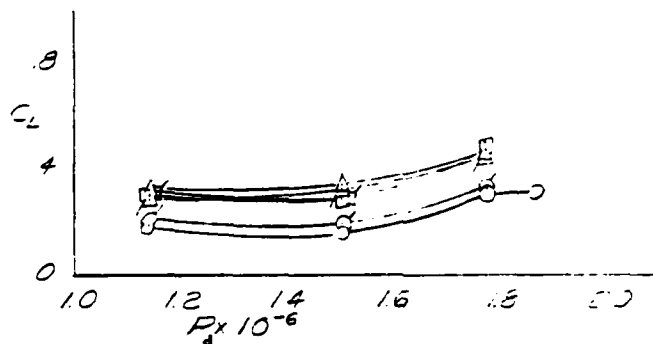


FIGURE A-16. FORCE AND MOMENT COEFFICIENTS FOR ROTADOME LOAD-CELL HEIGHT ON FAATC TOWER

0	$\psi = 0^\circ$	MOTOR FWD	RUN 15
0	" = "	" AFT	" 16
0	" = 22.5°	" FWD	" 4
0	" = "	" AFT	" 13
0	" = 45°	" FWD	" 4
0	" = "	" AFT	" 3

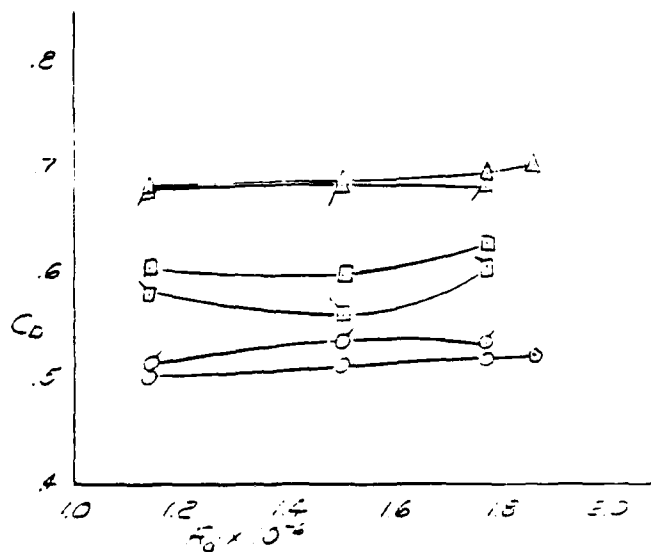


FIGURE A-16. FORCE AND MOMENT COEFFICIENTS FOR ROTADOME LOAD-CELL HEIGHT ON FAATC TOWER
(Continued)

$\psi = 0^\circ$, MOTOR FWD. , RUN 15
 $\alpha = "$ " , " AFT. , " 16
 $\Delta = 22.5^\circ$, " FWD. , " 14
 $\square = "$ " , " AFT. , " 13
 $\square = 45^\circ$, " FWD. , " 4
 $\square = "$, " AFT. , " 3

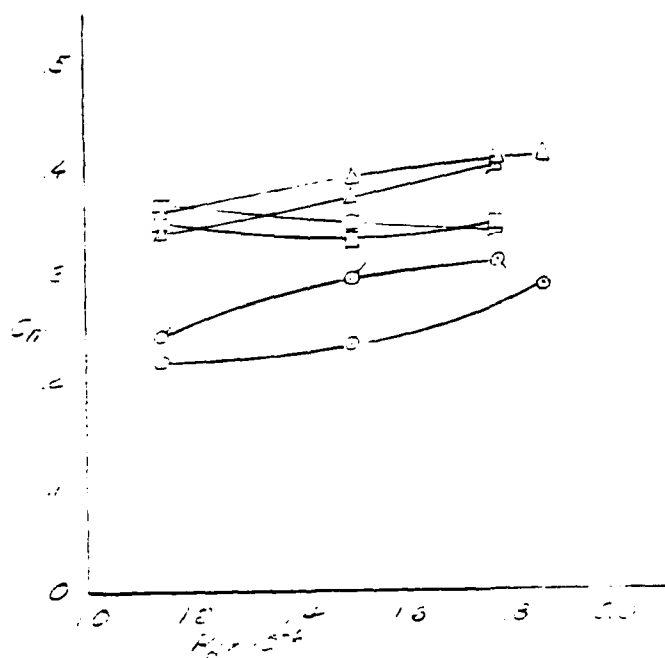


FIGURE A-16. FORCE AND MOMENT COEFFICIENTS FOR ROTADOME LOAD-CELL HEIGHT ON FAATC TOWER
 (Continued)

Water Jet

○ $\psi = 0^\circ$ Run 17
 △ $\psi = 22.5^\circ$ " 12

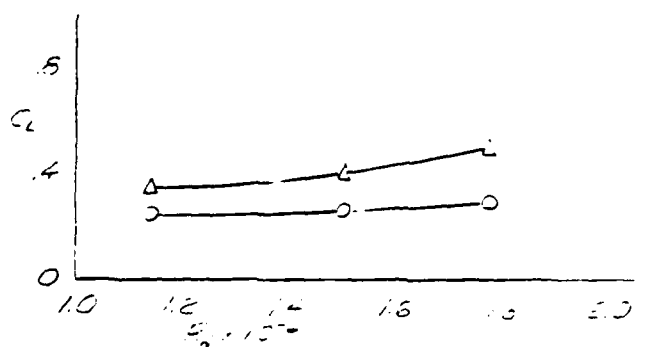


FIGURE A-17. FORCE AND MOMENT COEFFICIENTS FOR ROTADOME WITH SIMULATED LAP JOINTS AT LOAD-CELL HEIGHT ON FAATC TOWER

MOTOR AFT

○ $\psi = 0^\circ$, JUN 17
 Δ $\psi = 225^\circ$, " 12

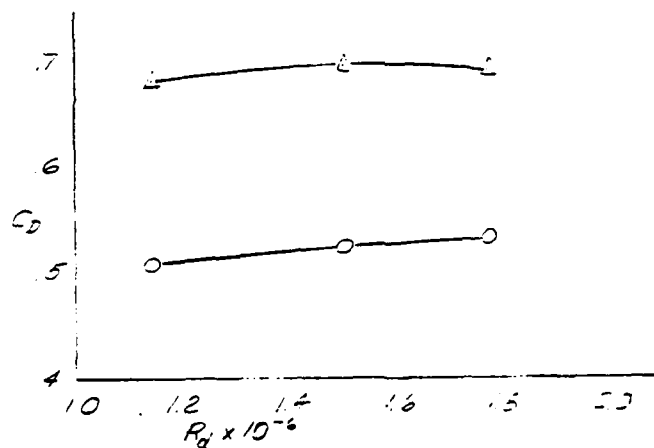


FIGURE A-17. FORCE AND MOMENT COEFFICIENTS FOR ROTADOME WITH SIMULATED LAP JOINTS AT LOAD-CELL HEIGHT ON FAATC TOWER (Continued)

MOTCR AFT

○ $\psi = 0^\circ$ 17
 △ $\psi = 22.5^\circ$ 12

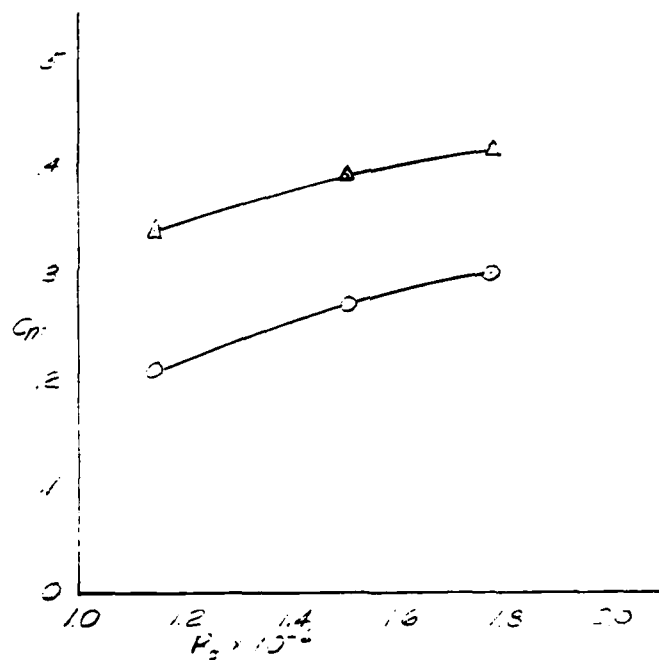


FIGURE A-17. FORCE AND MOMENT COEFFICIENTS FOR ROTADOME WITH SIMULATED LAP JOINTS AT LOAD-CELL HEIGHT ON FAATC TOWER (Continued)

0	$\psi = 0^\circ$	Water Fwd	Run 23
0	" = "	AFT	" 24
18	" = 18°	Fwd	" 30
18	" = "	AFT	" 29
56	" = 56°	Fwd	" 31
56	" = "	AFT	" 32

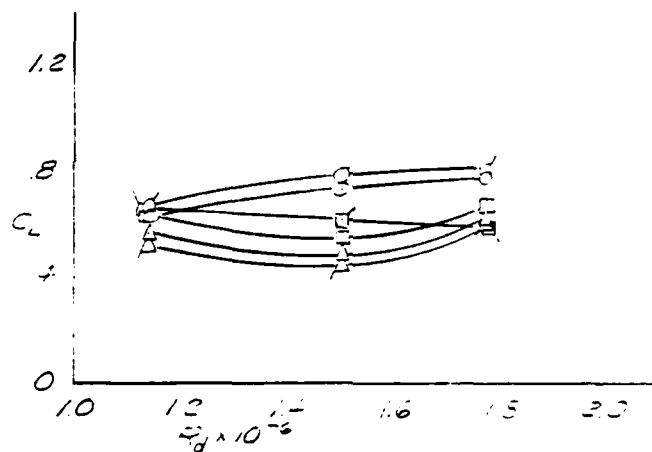


FIGURE A-18. FORCE AND MOMENT COEFFICIENTS
FOR ROTADOME AND PEI TOWER

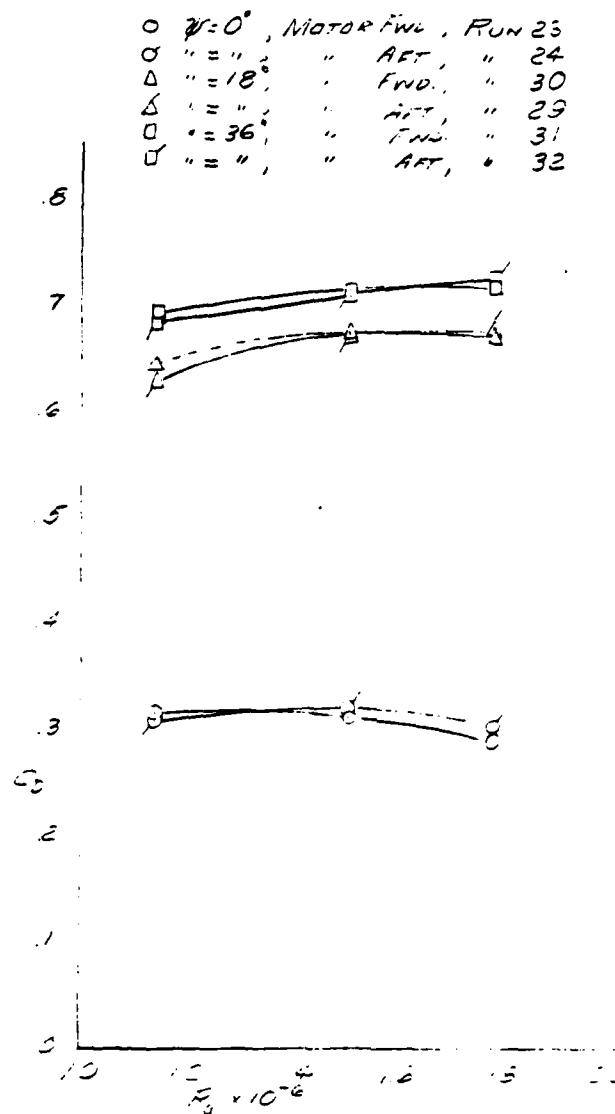


FIGURE A-18. FORCE AND MOMENT COEFFICIENTS
FOR ROTADOME AND PEI TOWER (Continued)

0	$\psi = 0^\circ$, MOTOR FWD, RUN 23
1	" = " " AFT, " 24
2	" = 18° , " FWD, " 30
3	" = " " AFT, " 29
4	" = 36° , " FWD, " 31
5	" = " " AFT, " 32

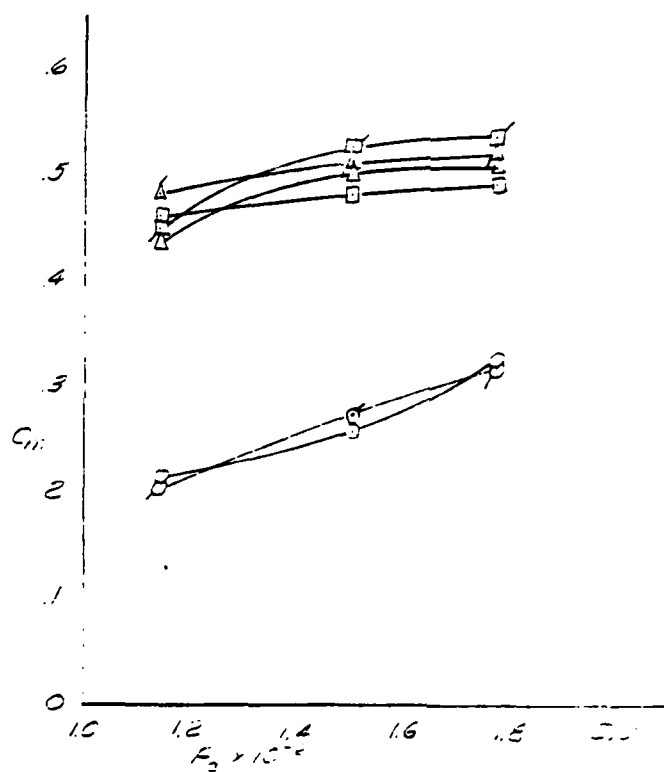


FIGURE A-18. FORCE AND MOMENT COEFFICIENTS FOR ROTADOME AND PEI TOWER. (Continued)

$\Delta \psi = 15^\circ$, MOTOR FWD, RUN 30

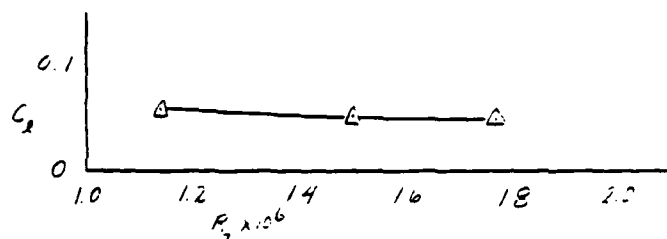


FIGURE A-18. FORCE AND MOMENT COEFFICIENTS FOR ROTADOME AND PEI TOWER (Continued)

$\Delta \gamma = 15^\circ$, MOTOR FWD, RUN 30

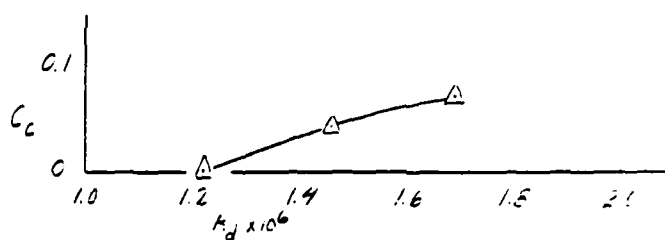


FIGURE A-18. FORCE AND MOMENT COEFFICIENTS
FOR ROTADOME AND PEI TOWER (Continued)

○	$\gamma = 0^\circ$, Motor	FWD.,	RUN 48
○	" = " , "	AFT.,	" 47
△	" = 22.5° , "	FWD.,	" 42
△	" = " , "	AFT.,	" 41
□	" = 45° , "	FWD.,	" 43
□	" = " , "	AFT.,	" 44

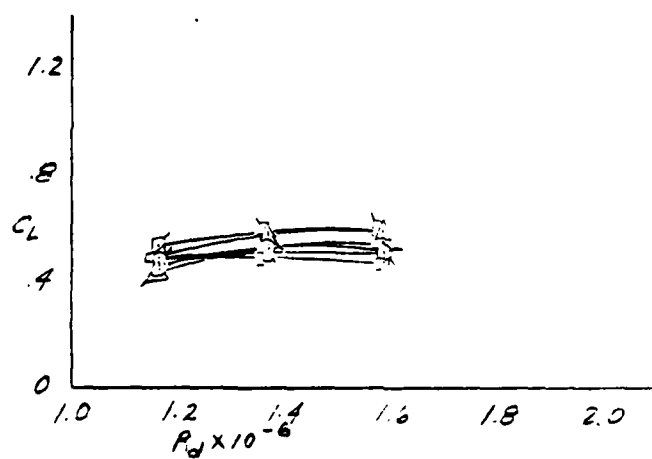


FIGURE A-19. FORCE AND MOMENT COEFFICIENTS FOR ROTADOME ON WELTON-BECKETT TOWER

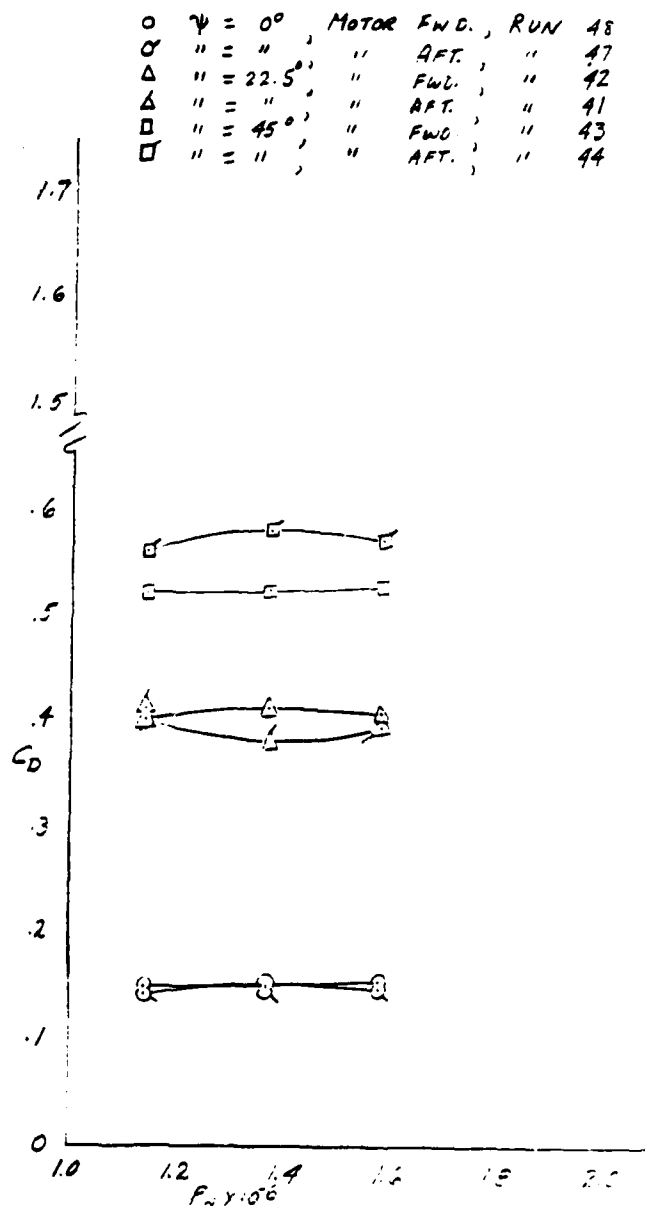


FIGURE A-19. FORCE AND MOMENT COEFFICIENTS FOR ROTADOME ON WELTON-BECKETT TOWER (Continued)

○	$\psi = 0^\circ$	MOTOR	FWD.	RUN	48
○	" = "	"	AFT.	"	47
△	" = 22.5°	"	FWD.	"	42
△	" = "	"	AFT.	"	41
□	" = 45°	"	FWD.	"	43
□	" = "	"	AFT.	"	44

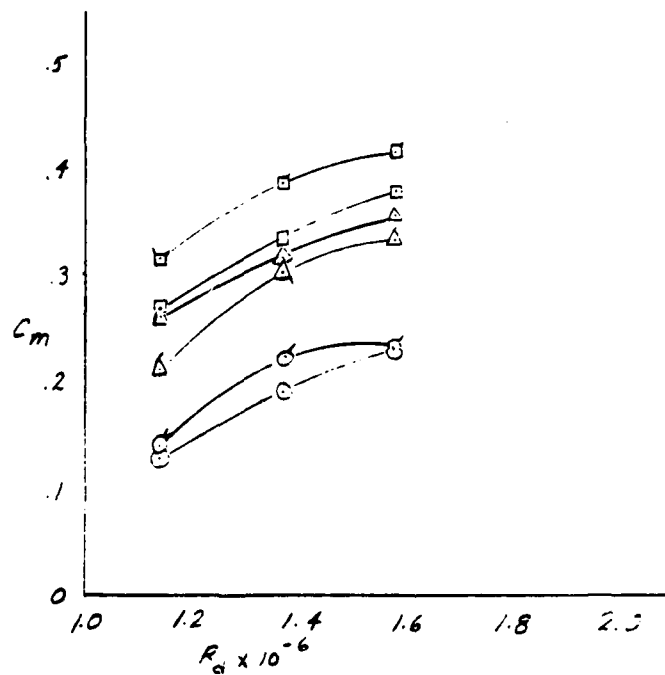


FIGURE A-19. FORCE AND MOMENT COEFFICIENTS FOR ROTADOME ON WELTON-BECKETT TOWER (Concluded)

\circ $\theta = 0^\circ$, Run 21
 Δ " = 22.5° , " 8
 \square " = 45° , " 5

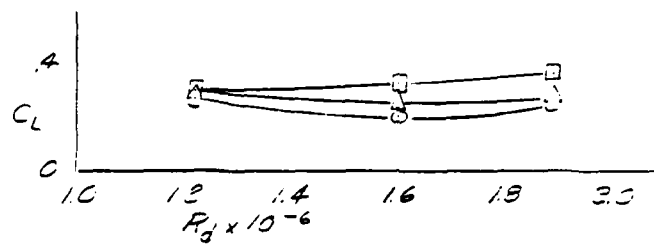


FIGURE A-20. FORCE AND MOMENT COEFFICIENTS FOR SPHERICAL RADOME ON FAATC TOWER

$\circ \psi = 0^\circ$, RUN 21
 $\Delta \psi = 22.5^\circ$, " 8
 $\square \psi = 45^\circ$, " 5

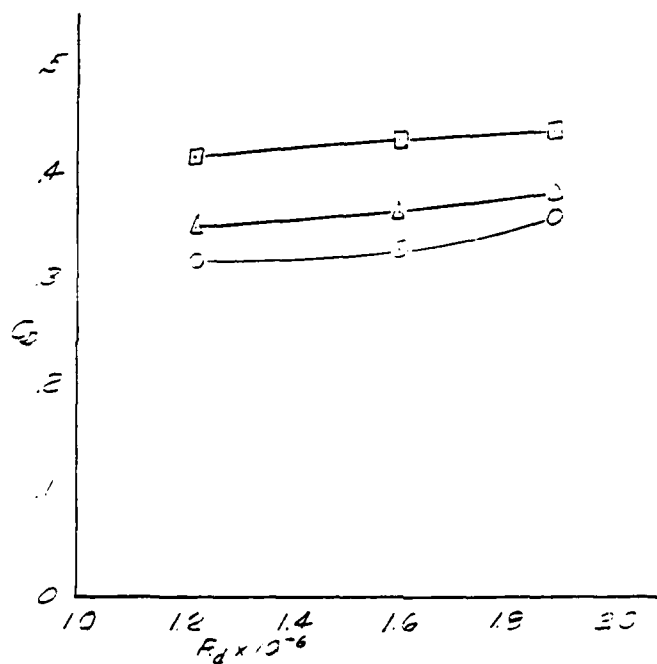


FIGURE A-20. FORCE AND MOMENT COEFFICIENTS FOR SPHERICAL RADOME ON FAATC TOWER (Continued)

\circ $\psi = 0^\circ$, RUN 21
 \triangle $\psi = 22.5^\circ$, " 8
 \square $\psi = 45^\circ$, " 5

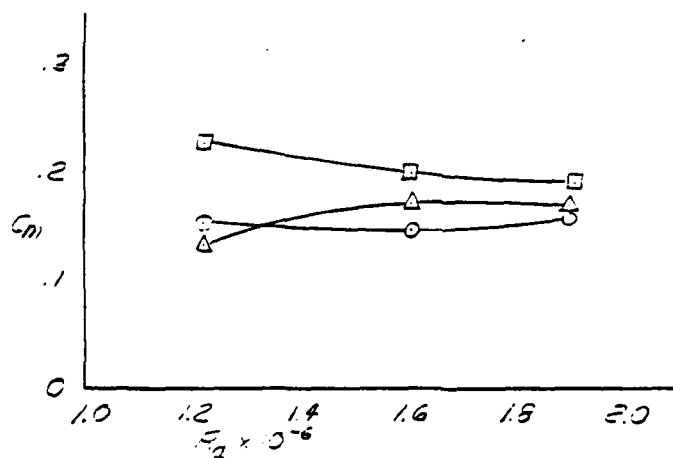


FIGURE A-20. FORCE AND MOMENT COEFFICIENTS FOR SPHERICAL RADOME ON FAATC TOWER (Continued)

$\Delta \psi = 22.5^\circ$, RUN B

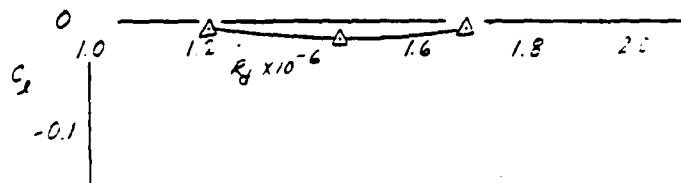


FIGURE A-20. FORCE AND MOMENT COEFFICIENTS FOR SPHERICAL RADOME ON FAATC TOWER (Continued)

$\Delta \psi = 22.5^\circ$, RUN 8

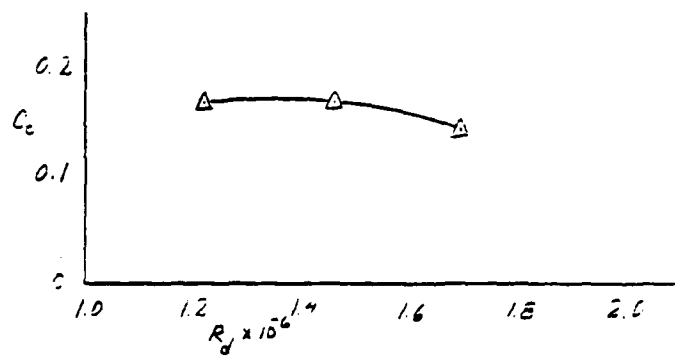


FIGURE A-20. FORCE AND MOMENT COEFFICIENTS FOR SPHERICAL RADOME ON FAATC TOWER (Concluded)

$\psi = 0^\circ$, RUN 25
 $\psi = 18^\circ$, " 28
 $\psi = 36^\circ$, " 33

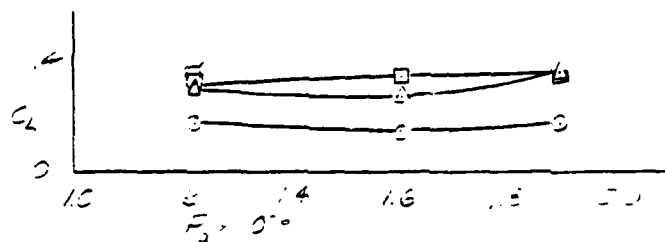


FIGURE A-21. FORCE AND MOMENT COEFFICIENTS FOR
 SPHERICAL RADOME ON PEI TOWER

$\circ \psi = 0^\circ$, RUN 25
 $\Delta \psi = 18^\circ$, " 28
 $\square \psi = 36^\circ$, " 33

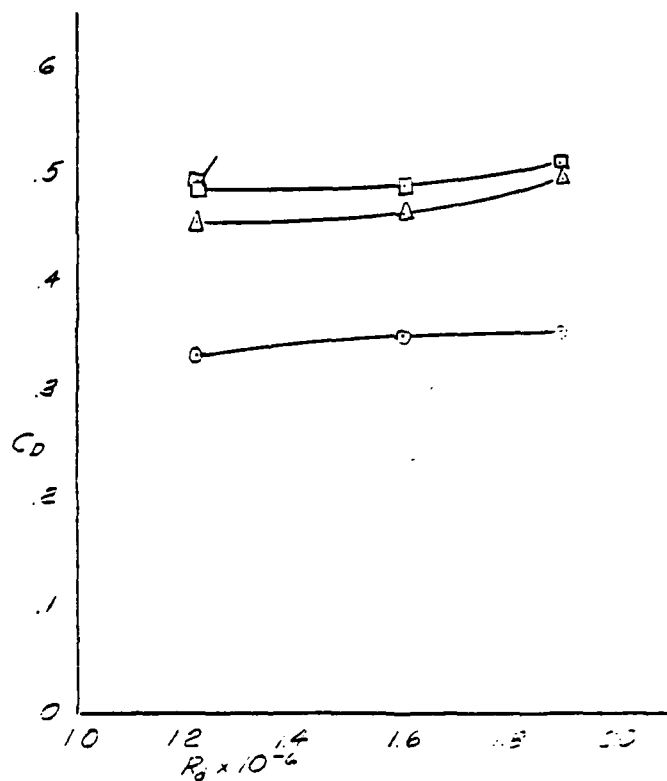


FIGURE A-21. FORCE AND MOMENT COEFFICIENTS FOR SPHERICAL RADOME ON PEI TOWER (Continued)

O $\psi = 0^\circ$, RUN 25
 A $\psi = 18^\circ$, " 28
 □ $\psi = 36^\circ$, " 33

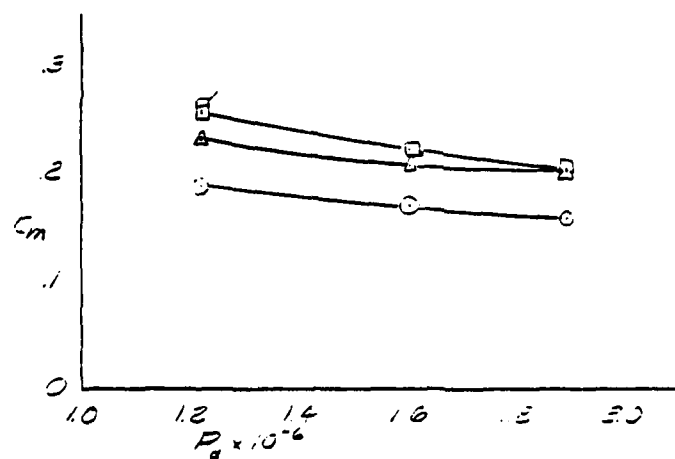


FIGURE A-21. FORCE AND MOMENT COEFFICIENTS FOR SPHERICAL RADOME ON PEI TOWER (Continued)

$\Delta \psi = 15^\circ$, RUN 28

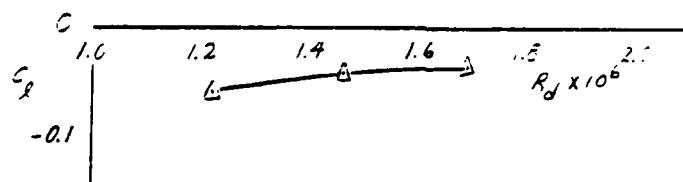


FIGURE A-21. FORCE AND MOMENT COEFFICIENTS FOR SPHERICAL RADOME ON PEI TOWER (Continued)

$\Delta \psi = 18^\circ$, Run 22

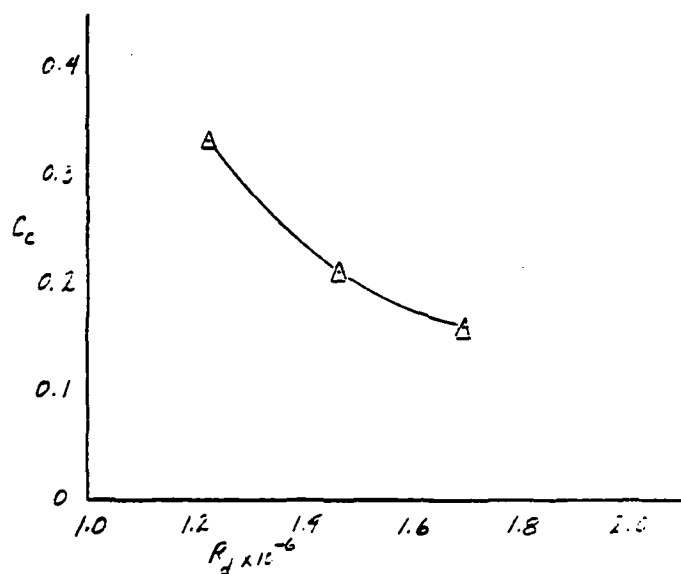


FIGURE A-21. FORCE AND MOMENT COEFFICIENTS FOR SPHERICAL RADOME ON PEI TOWER (Concluded)

O $\psi = 0^\circ$ RUN 49
 Δ " = 22.5° " 40
 □ " = 45° " 45

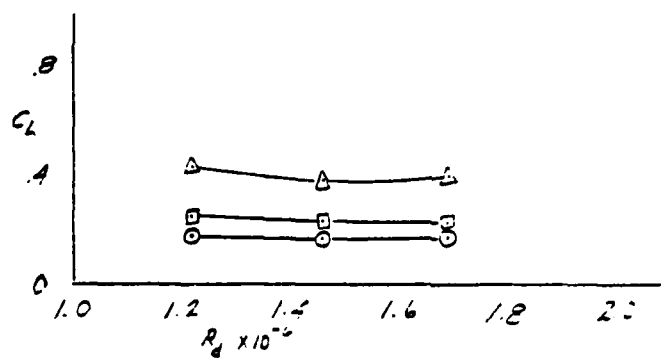


FIGURE A-22. FORCE AND MOMENT COEFFICIENTS FOR SPHERICAL RADOME ON WELTON-BECKETT TOWER

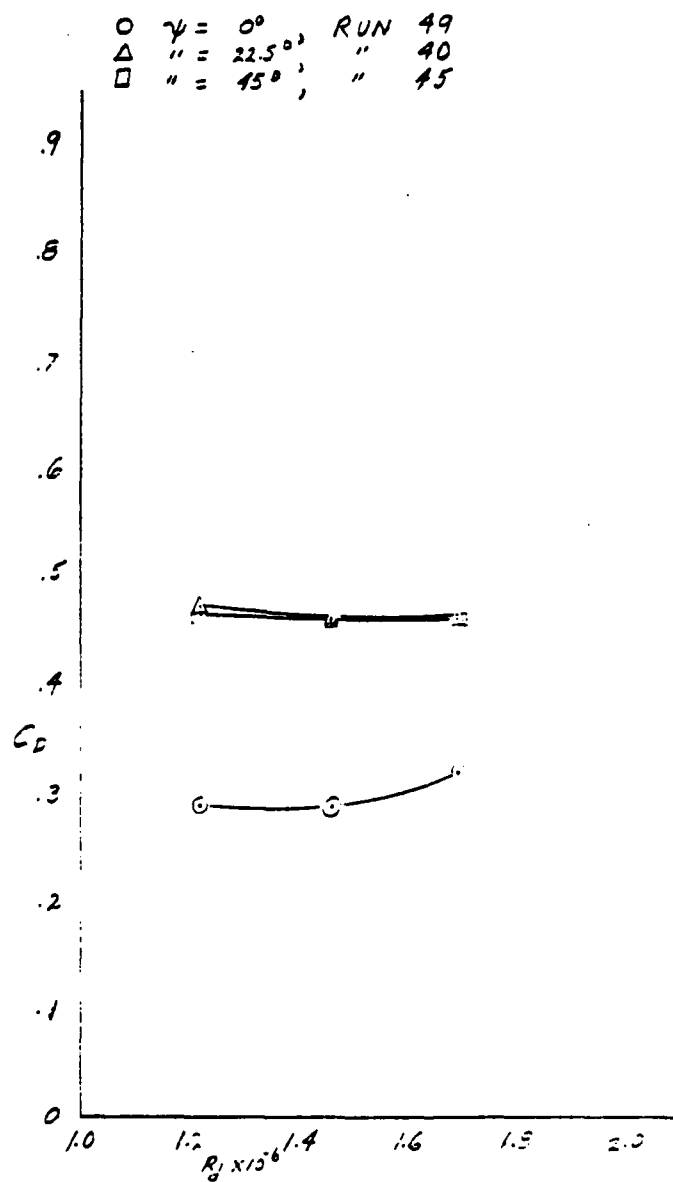


FIGURE A-22. FORCE AND MOMENT COEFFICIENTS FOR SPHERICAL RADOME ON WELTON-BECKETT TOWER (Continued)

O $\psi = 0^\circ$, RUN 49
 Δ " = 22.5° , " 40
 □ " = 45° , " 45

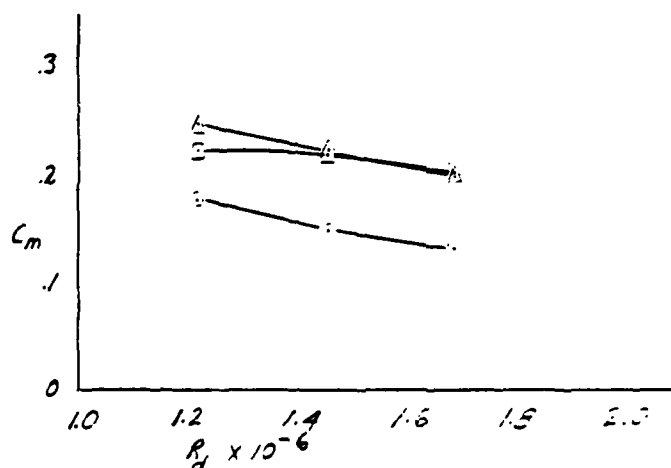


FIGURE A-22. FORCE AND MOMENT COEFFICIENTS FOR SPHERICAL RADOME ON WELTON-BECKETT TOWER (Concluded)

O $\psi = 0^\circ$, RUN 22
 Δ " = 22.5°, " 7
 □ " = 45°, " 6

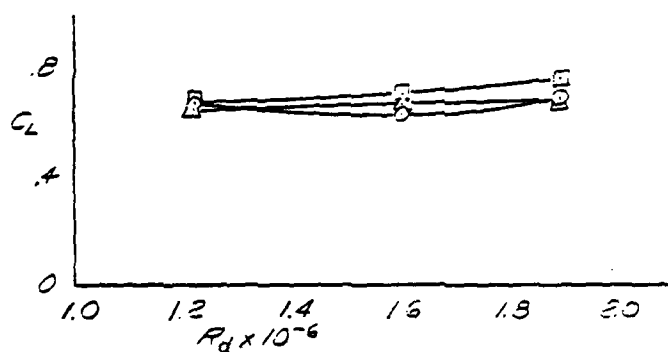


FIGURE A-23. FORCE AND MOMENT COEFFICIENTS FOR TEACUP RADOME ON FAATC, TOWER

$\circ \psi = 0^\circ$, RUN 22
 $\Delta \psi = 22.5^\circ$, " 7
 $\square \psi = 45^\circ$, " 6

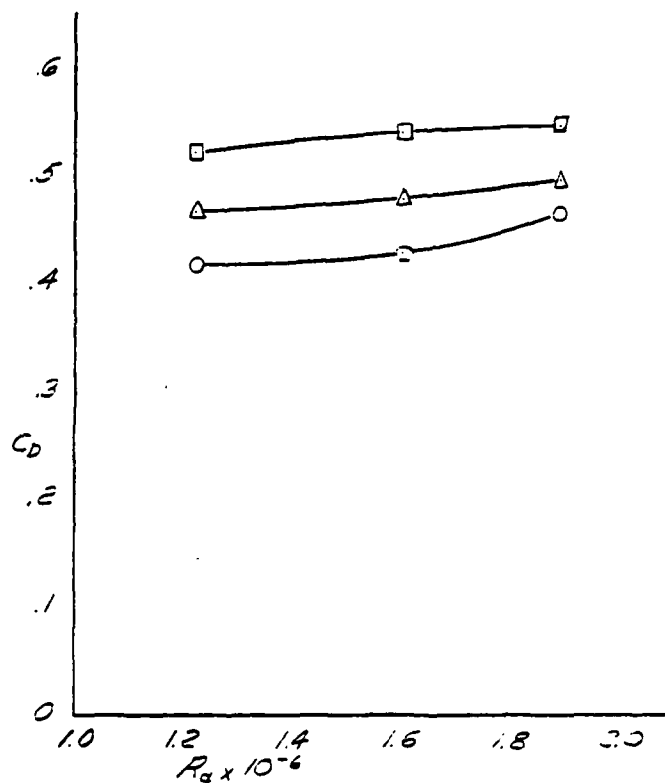


FIGURE A-23. FORCE AND MOMENT COEFFICIENTS FOR TEACUP RADOME ON FAATC TOWER (Continued)

\circ $\gamma = 0^\circ$ RUN 22
 Δ " = 22.5° " 7
 \square " = 45° " 6

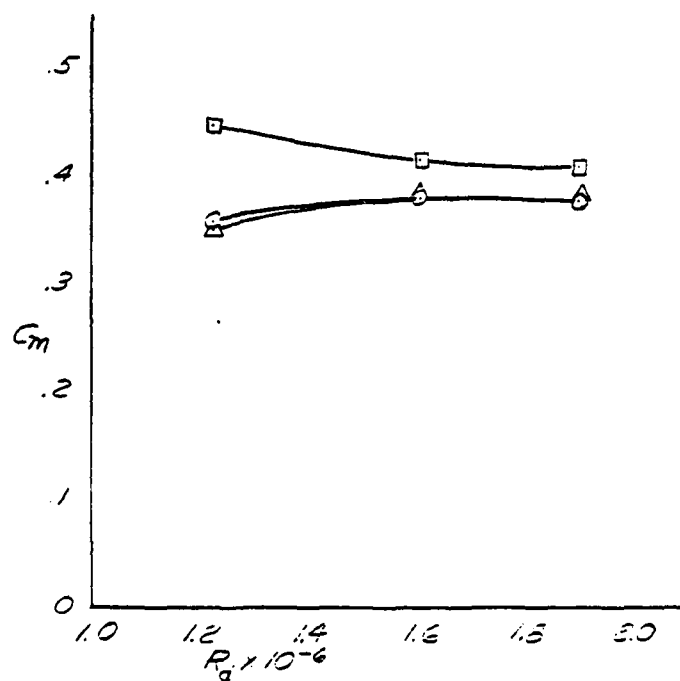


FIGURE A-23. FORCE AND MOMENT COEFFICIENTS FOR TEACUP RADOME ON FAATC TOWER (Continued)

$\Delta \psi = 22.5^\circ$, RUN 7

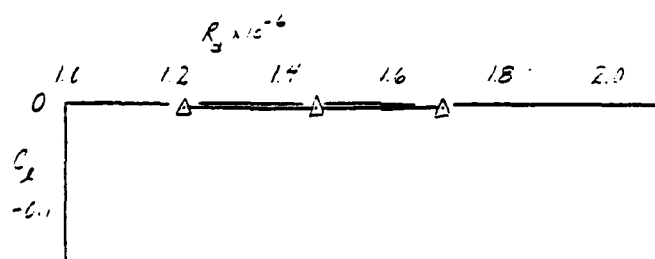


FIGURE A-23. FORCE AND MOMENT COEFFICIENTS FOR TEACUP RADOME ON FAATC TOWER (Continued)

$\Delta \psi = 22.5^\circ$, RUN 7

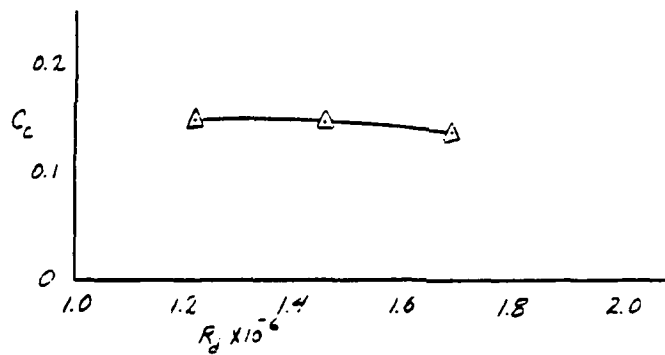


FIGURE A-23. FORCE AND MOMENT COEFFICIENTS FOR TEACUP RADOME
ON FAATC TOWER (Concluded)

O $\psi = 0^\circ$, RUN 26
 Δ $\psi = 18^\circ$, " 27
 □ $\psi = 36^\circ$, " 34

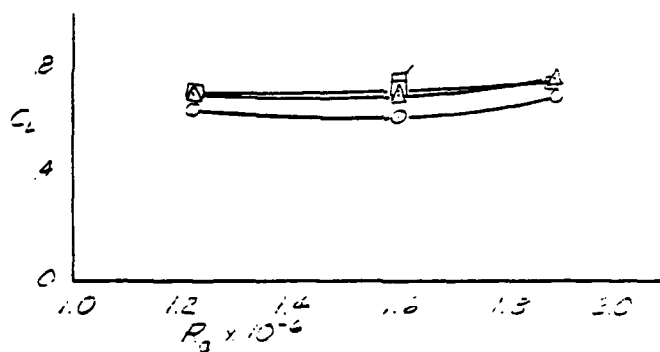


FIGURE A-24. FORCE AND MOMENT COEFFICIENT FOR TEACUP RADOME ON PEI TOWER

○ $\psi = 0^\circ$, RUN 26
 △ $\psi = 18^\circ$, " 27
 □ $\psi = 36^\circ$, " 34

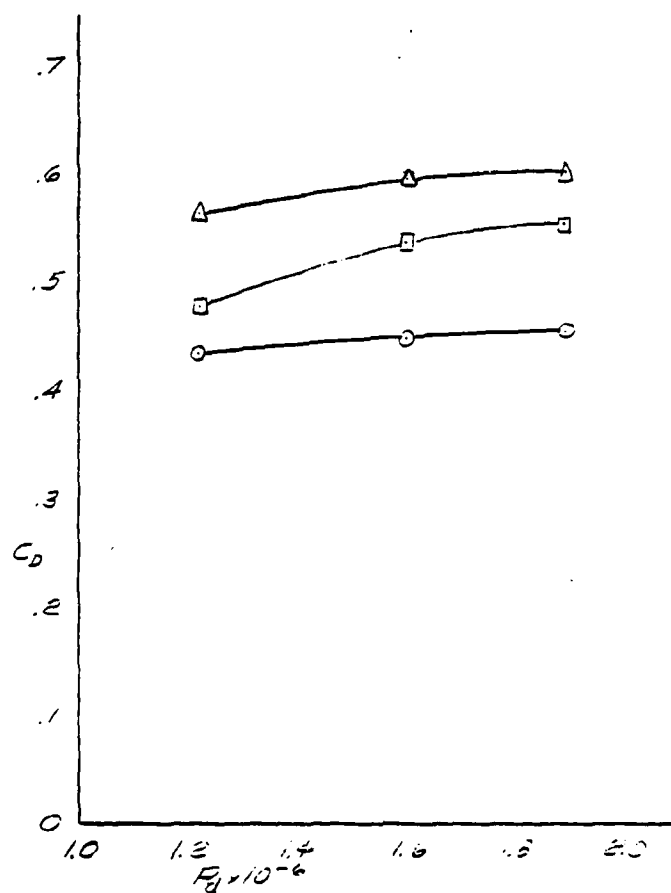


FIGURE A-24. FORCE AND MOMENT COEFFICIENT FOR TEACUP RADOME ON PEI TOWER (Continued)

\circ $\psi = 0^\circ$, RUN 26
 Δ $\psi = 18^\circ$, " 27
 \square $\psi = 36^\circ$, " 34

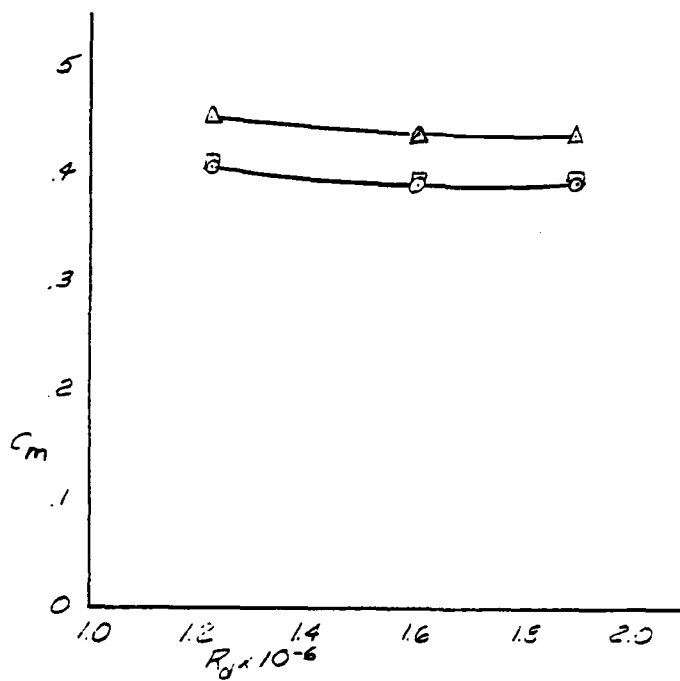


FIGURE A-24. FORCE AND MOMENT COEFFICIENT FOR TEACUP RADOME ON PEI TOWER (Continued)

$\Delta \psi = 18^\circ$, RUN 27

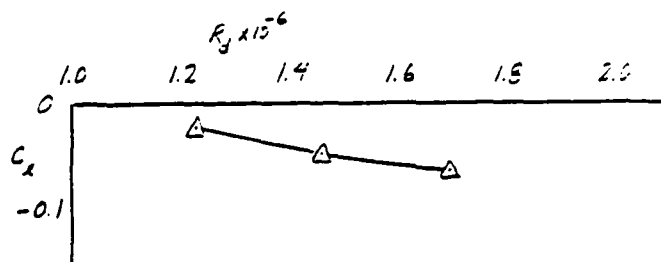


FIGURE A-24. FORCE AND MOMENT COEFFICIENT FOR TEACUP RADOME ON PEI TOWER (Continued)

$\Delta \psi = 15^\circ$, RUN 27

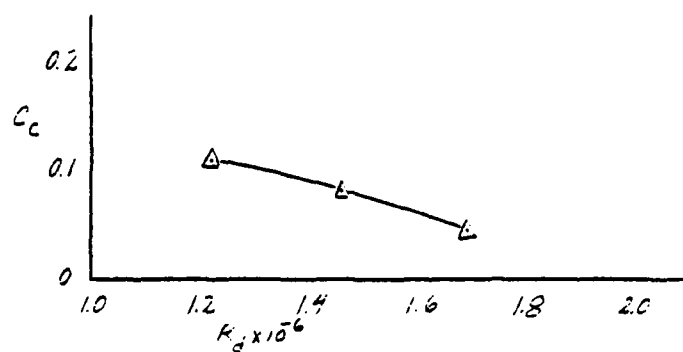


FIGURE A-24. FORCE AND MOMENT COEFFICIENT FOR TEACUP RADOME ON PEI TOWER (Concluded)

○ $\gamma = 0^\circ$, RUN 50
 △ " = 22.5° , " 39
 □ " = 45° , " 16

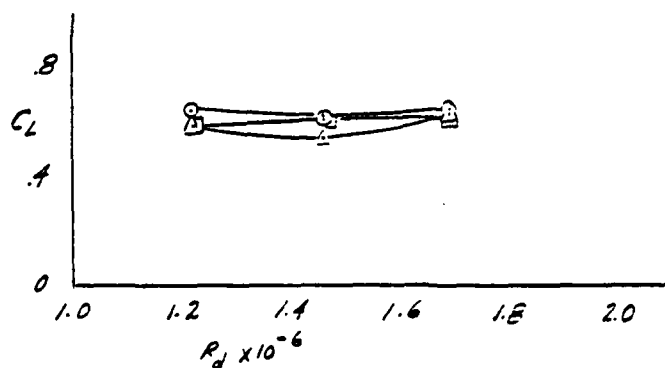


FIGURE A-25. FORCE AND MOMENT COEFFICIENTS FOR TEACUP RADOME ON WELTON-BECKETT TOWER

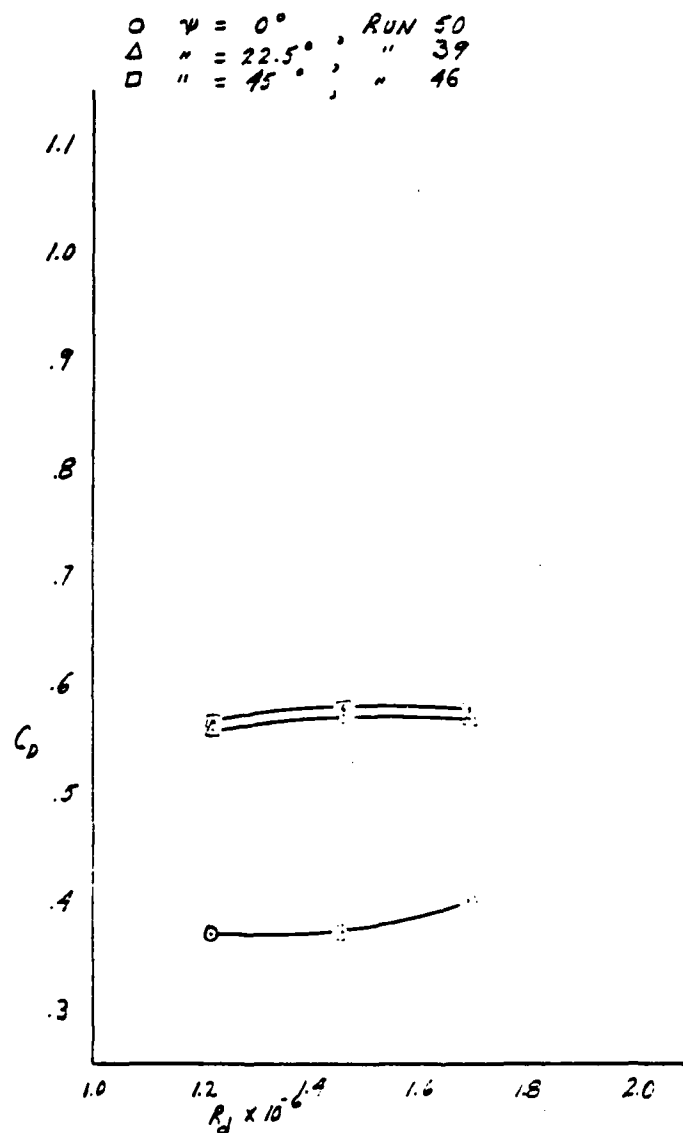


FIGURE A-25. FORCE AND MOMENT COEFFICIENTS FOR TEACUP RADOME ON WELTON-BECKETT TOWER (Continued)

\circ $\psi = 0^\circ$, RUN 50
 Δ $\psi = 22.5^\circ$, " 39
 \square $\psi = 45^\circ$, " 46

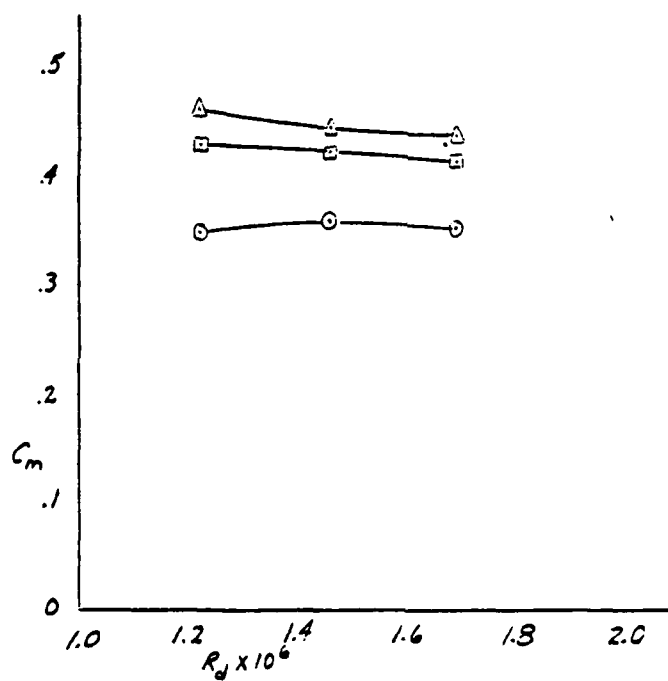


FIGURE A-25. FORCE AND MOMENT COEFFICIENTS FOR TEACUP RADOME ON WELTON-BECKETT TOWER (Concluded)

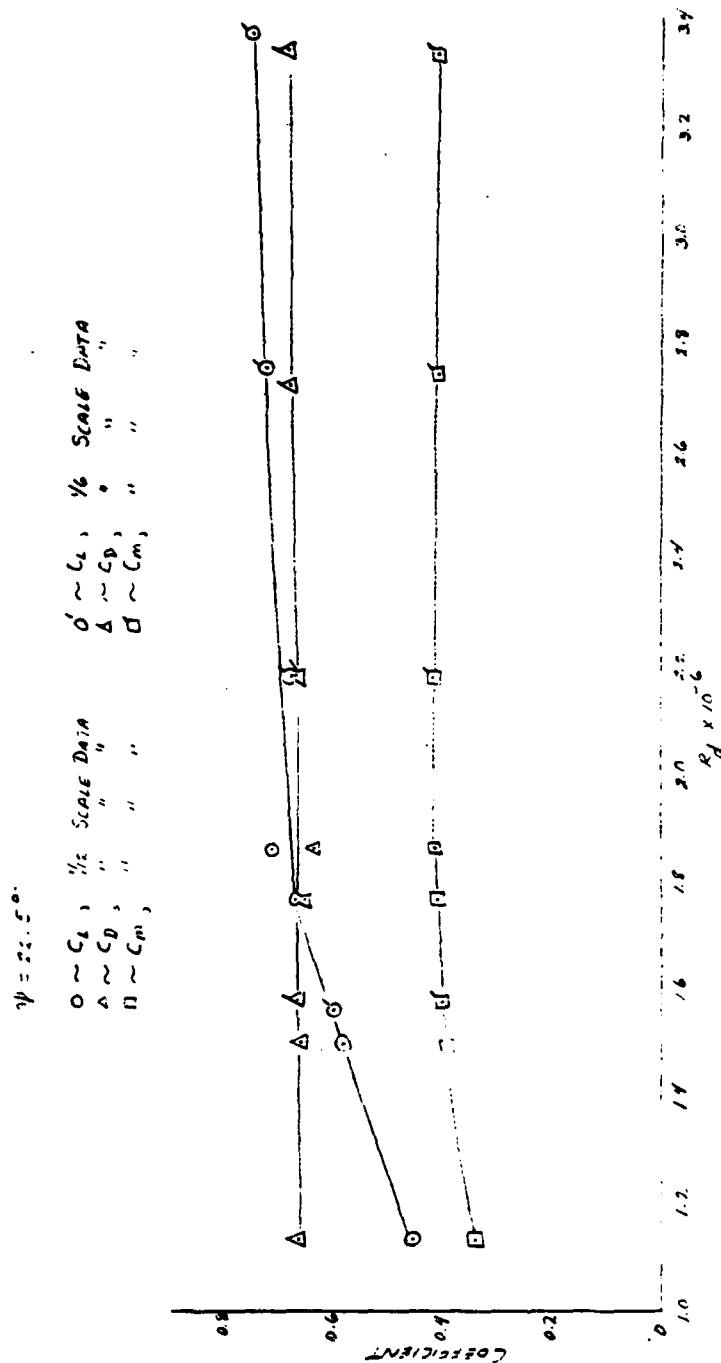


FIGURE A-26. COMBINED ONE-TWELFTH AND ONE-SIXTH-SCALE DATA FOR ROTADOME ON THE FAATC TOWER

$\psi = 45^\circ$
 $\circ \sim C_L, \quad 1/11 \text{ SCALE DATA}$
 $\Delta \sim C_D, \quad \text{"}$
 $\square \sim C_m, \quad \text{"}$
 $\delta \sim C_L, \quad 1/6 \text{ SCALE DATA}$
 $\Delta \sim C_D, \quad \text{"}$
 $\square \sim C_m, \quad \text{"}$

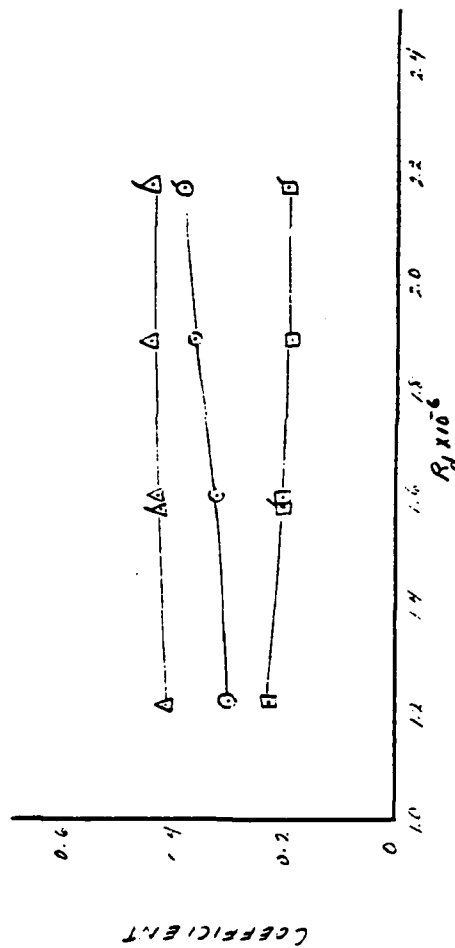


FIGURE A-27. COMBINED ONE-TWELFTH AND ONE-SIXTH-SCALE DATA FOR SPHERICAL RADOME ON THE FAATC TOWER

∇ $\psi = 23^\circ$, MOTOR FLOW, RUN 51
 \diamond $\psi = -3.6^\circ$, " " " " 52

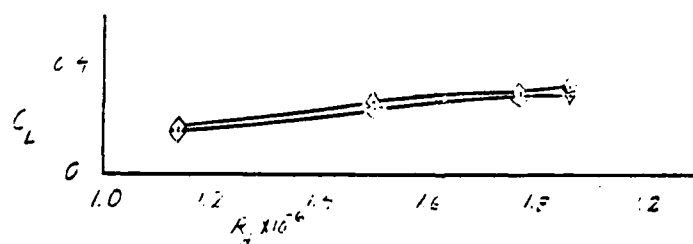


FIGURE A-28. FORCE AND MOMENT COEFFICIENTS FOR ROTADOME ON
 FAATC TOWER WITH LOAD-CELLS INSTALLED AT WIND ANGLES
 ENCOUNTERED MOST OFTEN DURING FIELD TESTS

∇ $\psi = 23^\circ$, MOTOR FWD., RUN 51
 \diamond " $= -3.6^\circ$, " " " " 52

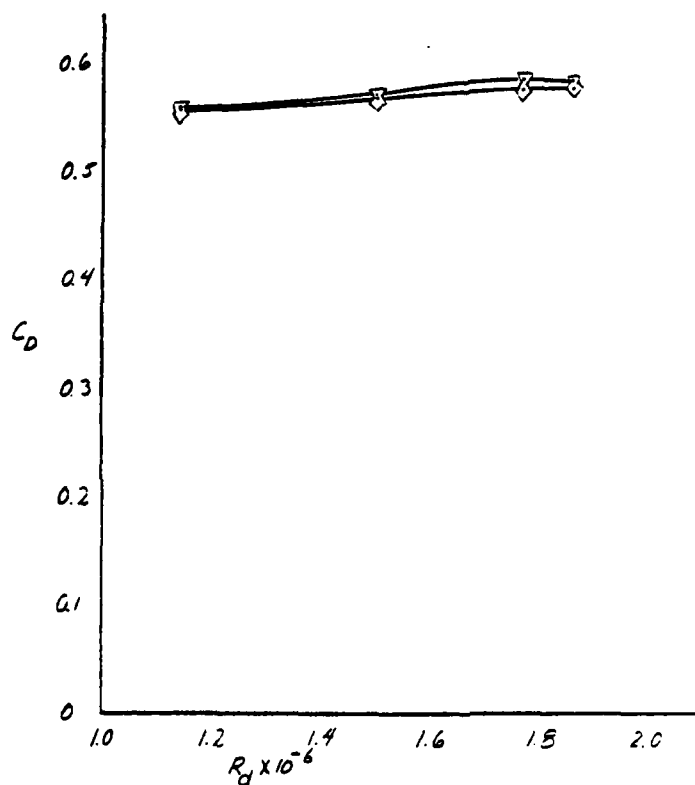


FIGURE A-28. FORCE AND MOMENT COEFFICIENTS FOR ROTADOME ON
 FAATC TOWER WITH LOAD-CELLS INSTALLED AT WIND ANGLES
 ENCOUNTERED MOST OFTEN DURING FIELD TESTS (Continued)

∇ $\psi = 2.30$, MOTOR F.W.C., RUN 51
 \diamond " $= -3.60$, " " " " 52

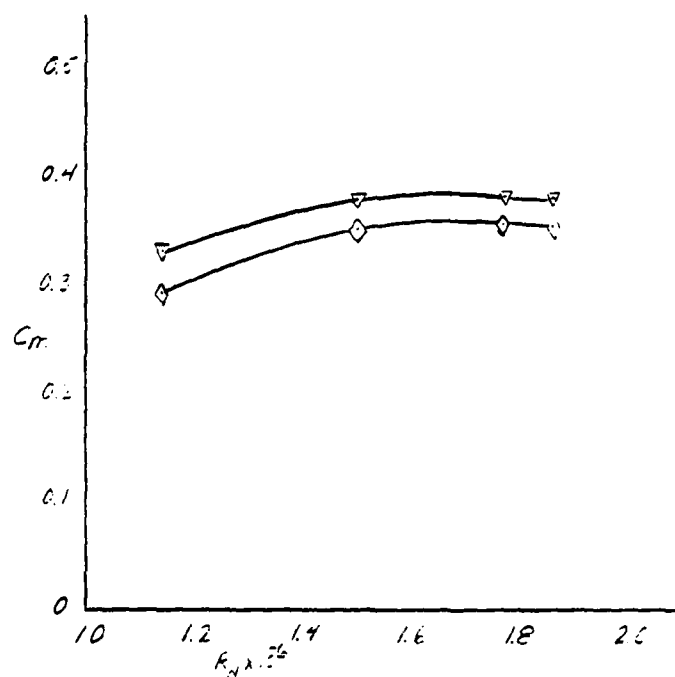


FIGURE A-28. FORCE AND MOMENT COEFFICIENTS FOR ROTADOME ON
 FAATC TOWER WITH LOAD-CELLS INSTALLED AT WIND ANGLES
 ENCOUNTERED MOST OFTEN DURING FIELD TESTS (Continued)

AD-A105 854

CALIFORNIA INST OF TECH PASADENA GRADUATE AERONAUTIC--ETC F/G 20/4
DETERMINATION OF AIRLOADS ON CERTAIN AIRPORT TOWERS DUE TO ADDI--ETC(U)
AUG 81 C D BABCOCK, W H BETTES DOT-TSC-1633
GALCIT-1020

UNCLASSIFIED

FAA/RD-81-74

NL

2 OF 2

AD-A
105 854

END

DATE

FILMED

11-81

DTIC

$\nabla \psi = 2.3^\circ$, MOTOR FWD., $R_d \times 10^{-6}$
 $\diamond \psi = -3.6^\circ$, " " " " " "

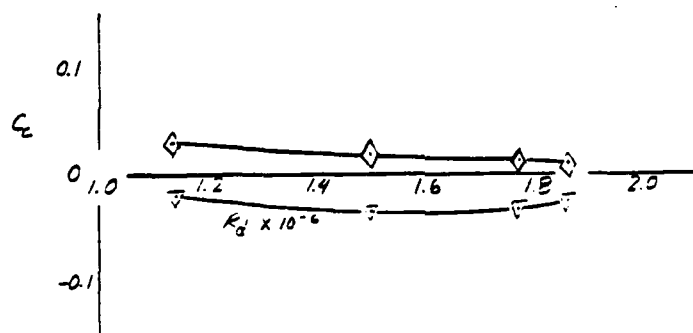


FIGURE A-28. FORCE AND MOMENT COEFFICIENTS FOR ROTADOME ON
 FAATC TOWER WITH LOAD-CELLS INSTALLED AT WIND ANGLES
 ENCOUNTERED MOST OFTEN DURING FIELD TESTS (Continued)

$\nabla \psi = 2.3^\circ$, Motor FWD, Run 51
 $\diamond \psi = -3.6^\circ$, " " " " 52

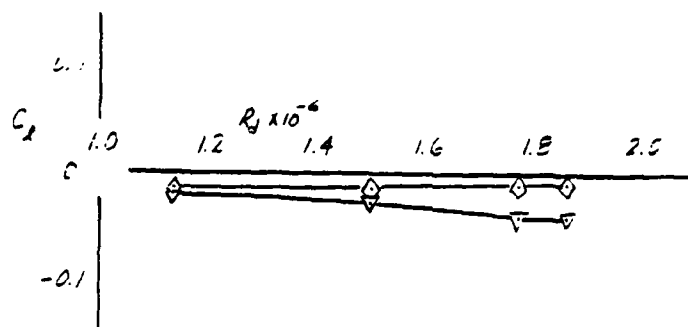


FIGURE A-28. FORCE AND MOMENT COEFFICIENTS FOR ROTADOME ON
 FAATC TOWER WITH LOAD-CELLS INSTALLED AT WIND ANGLES
 ENCOUNTERED MOST OFTEN DURING FIELD TESTS (Concluded)

to each of the aforementioned towers are presented in Figures A-20 through A-22, and results of the teacup radome tests in proximity to the same tower configurations are presented in Figures A-23 through A-25.

While attempts were made to test each configuration at the highest airstream velocity possible, to obtain the higher Reynolds numbers, problems were encountered as follows. For the FAATC and Pei towers, intermittent grounding occurred (contact between tower model and antenna support strut) at $q = 55 \text{ lb/ft}^2$. When grounding occurred, the data were discarded. The large size and consequent large airloads on the Welton-Beckett tower limited the airstream dynamic pressure to 40 lb/ft^2 for the same reason.

An overview of the data shows that both airport-tower geometry, and the angle of the approaching wind relative to the tower, have a substantial effect on the airloads encountered by all of the radome configurations tested. For example, all of the radomes tested encountered maximum airloads when $18^\circ \leq \psi \leq 45^\circ$, depending upon tower geometry. At these angles, the flat sides of the upper portion of all of the towers was not normal to the approaching airstream as they were at $\psi = 0^\circ$. When a large flat side of the tower is normal to the airstream, the airflow is separated over a substantial portion of the tower roof which, in effect, shields the lower portion of a radome mounted on this roof from the airstream. This was verified by flow visualization tests in the wind tunnel.

In general, the maximum airloads on each radome were recorded when the radome was mounted on the Pei tower, with the lowest airloads recorded for the radome in proximity to the Welton-Beckett or FAATC towers. The Pei tower was the smallest of the towers represented relative to the size of the radomes. The fact that the larger airloads were recorded with the radomes in proximity to the Pei tower is again due to the flow separation which occurs over the cab roof of all of the towers tested. The smallest tower (the Pei) had a smaller separation zone.

The maximum airloads occurred during these limited tests for each of the radomes as follows: The rotadome encountered its maximum airloads when the FAATC tower was at $\psi = 22.5^\circ$, when the Pei tower was at $\psi = 36^\circ$, and the Welton-Beckett tower was at $\psi = 45^\circ$. The spherical radome encountered maximum airloads when the FAATC tower was at 45° , the Pei tower $\psi = 36^\circ$, and the Welton-Beckett tower at $\psi = 22.5^\circ$. The teacup radome encountered its maximum airload for the FAATC tower at $\psi = 45^\circ$, the Pei tower at $\psi = 18^\circ$, and the Welton-Beckett tower at $\psi = 22.5^\circ$. In general, the maximum radome airloads occurred when a major corner of the upper portion of a tower was facing into the wind. This is the condition which minimizes the airflow separation over the tower-cab roof, and allows the full force of the wind to contact the radome.

Certain test wind angles relative to the tower models resulted in an asymmetric flow over the tower-cab roof, and hence, over the radome models. For these cases, non-zero rolling moments and cross-wind forces were generated on the radomes (i.e., a moment and a force acting in the plane normal to the approaching airstream). This situation occurred for the FAATC tower at $\psi = 22.5^\circ$, and the Pei tower at $\psi = 18^\circ$. Data acquired using the Welton-Beckett tower, at the selected test angles, did not display any such non-zero values of rolling moment or cross-wind force. This was either due to the fact that the lower portion of the Welton-Beckett tower was so large that it masked asymmetric details on the tower cab, or that the test angles used did not result in sufficient tower-cab asymmetry to influence strongly the lateral data.

It should be pointed out that a comparison of airloads between the various test radomes can only be made after multiplying the force and moment coefficients by the projected frontal areas (A) of each respective radome, given in Table A-2. The moment coefficient must also be multiplied by the radome diameter, d.

· Making this comparison at $R_d = 1.8 \times 10^{-6}$ reveals that the drag force or shear load transmitted into the tower-cab roof by radome airloads is twice as large for the spherical and teacup radomes as for the rotadome. The lift force which is not of much interest since the lift loads do not exceed the static weight of the radomes by much even at $V = 130$ mph, full scale, is highest for the teacup radome due to the large overhang at the juncture of the spherical and conical sections. The lift loads are lowest for the rotadome, probably because the lower section of this radome was in a tower-induced flow separation zone for all towers tested. The overturning moments were again highest for the teacup radome for all towers tested because of the overhang as previously described. The primary overturning moments given by $C_m \times A \times d \times q$ for the rotadome and the spherical radome were somewhat similar in magnitude for each tower configuration, with the rotadome having consistently lower moments.

The flow-visualization tests, in addition to depicting the tower-separation region previously mentioned, showed large flow angularity just upstream of the radomes. These angles, measured in the vertical plane, were found to be of the order of 20 degrees up to 2 ft (model scale) upstream of the tower cab at cab-roof level for both the FAATC and Welton-Backett towers at $\psi = 0^\circ$. This angularity was reduced to the order of 12° for the $\psi \neq 0^\circ$ angles. Flow angularity upstream of the Pei tower was of the order of 10 degrees.

Special data recorded during the initial wind tunnel tests primarily for analyzing the field test data are presented in Figures A-16 and A-17. The field tests were conducted after the initial wind tunnel tests were complete. When the model of the rotadome was designed, it was not known if lap joints or external bands would be used to assemble the radome-surface elements. It was therefore, necessary to determine if these joints would affect the data, and as shown by comparing Figures A-16 and A-17, these joints produce little or no effect. A photograph of the lap-joint simulation is presented in Figure A-8.

To measure the radome airloads during the field tests, it was necessary to install the rotadome on top of load cells attached to the FAATC tower roof. This resulted in positioning the radome 4.5 inches, full scale, higher relative to the tower roof than would be the case for a normal installation. To determine the effects of this change in the wind tunnel, a spacer was installed between the support strut and radome, such that the radome would be correctly positioned on the tower for field test data comparison. The results of these data are presented in Figure A-16, and by comparing these data with those presented in Figure A-14, the effects of rotadome height relative to the FAATC tower can be determined. These results indicate that while the lift is reduced by over 30 percent due to the height increase, the drag is increased by only 5 percent and the moment is not affected. This suggests that the moment is primarily due to the drag force acting on the radome and its center of pressure, and that the lift force is acting near the center of rotation of the radome where the moment is referenced.

Another investigation carried out during these tests was to look at the effects of the rotadome drive motor and drive belt pan positions relative to the airstream. Data presented in Figures A-14, A-16, A-18, and A-19 show this comparison directly. As can be seen, these effects are relatively small in all cases primarily because the motor and pan are usually located within the airflow separation zone from the towers. Photographs of the upstream (Fwd.) and downstream (Aft) motor locations tested are shown in Figure A-7.

Upon completion of the field tests and the field test data analysis, it was found that a majority of these field data were recorded at wind-approach angles of $\psi = 2.3^\circ$ and $\psi = -3.6^\circ$, as well as some near $\psi = 0^\circ$. To have a larger wind tunnel data base to compare with the field test data, the FAATC tower and rotadome model was retested at $\psi = 2.3^\circ$ and $\psi = -3.6^\circ$. These data are presented in Figure A-28 as well as in the body of this report.

Airflow interactions between the separating shear layer from the various towers, and the airstream and separations around the radomes themselves, make the extrapolation of the wind tunnel data, with its limited Reynolds number range, difficult if the coefficient values appear to be varying with Reynolds number at the limit of the wind tunnel data. While the majority of the coefficient data appears to be approaching a constant value with increasing Reynolds number over the wind tunnel test range, those data recorded with the FAATC tower in place seem to be an exception.

To extend the Reynolds number range to approximately twice that available during the present tests, data recorded during previous tests of the rotadome and spherical radome in proximity to the FAATC tower were used. These data are reported in GALCIT Report 997,* where 1/6-scale models were used. One-sixth-scale models were not used during the present series because insufficient portions of the Pei and Welton-Backett towers could have been represented. The 1/6-scale test data have been normalized by the same reference dimensions used for the present tests, in appropriate scale, and are presented together with test data in Figures A-26 and A-27. Data are for the highest airloads measured.

* Wind Tunnel Tests on 1/6-Scale Models of a Teledyne Rotadome and a Spherical Radome in Proximity to a Truss-supported Tower. GALCIT Report 997, California Institute of Technology, Gussenheim Graduate Aeronautical Laboratories, Pasadena, CA, Sep. 1977.

APPENDIX B

FIELD TESTS

Introduction

One phase of the airload-determination program for the ASDE-3 rotadome was a field test of the prototype. The rotadome was mounted on one of the towers at the FAATC Center, Atlantic City, New Jersey, and was in operational condition. A photograph of the tower and rotadome is shown in Figure B-1.

The objectives of the field test were (a) to measure the airloads on the rotadome, and (b) to compare these with the loads measured on a 1/12-scale model in the GALCIT 10-foot wind tunnel. To accomplish this, simultaneous loads and wind measurements were necessary, so that load coefficients could be calculated. The instrumentation, data acquisition, data reduction, and results are discussed in subsequent sections.

Instrumentation and Calibration

The measurement of all six load components requires a complicated load-measurement system. This is difficult to accomplish particularly in a full-scale field test where less than ideal conditions are often encountered. It was decided early in the program that only the vertical loads at each of the three legs of the rotadome-mounting pedestal would be measured. This would enable the calculation of lift, pitching moment, and rolling moment in the load cell plane. The remaining components (drag, yawing moment, and side forces) could not be found from the load-cell configuration chosen.

The load cells chosen were BLH type U3L2. BLH signal-conditioning units provided excitation voltage, zero balance, and output connections. As installed, calibration was accomplished by statistically loading the load cells using a center bolt accessible inside of the tower house below the rotadome.

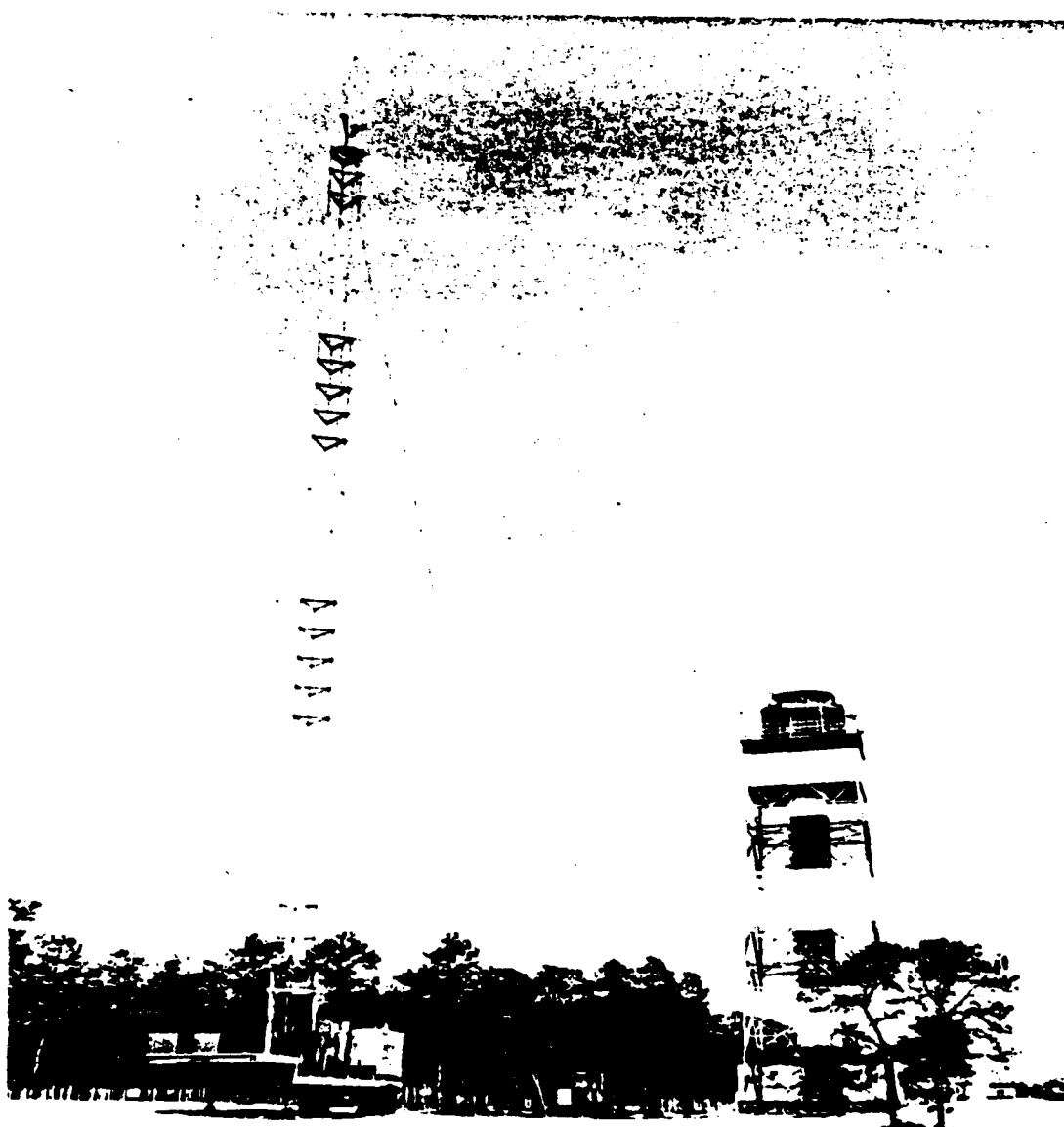


FIGURE B-1. ROTADOME AND TOWER AT FAATC

The capacity of each load cell was 5,000 lb. This was larger than desirable, and was chosen due to safety and overload (during installation) considerations. The expected wind loads were of the order of a few hundred pounds, and calibration was carried out to 200-lb compression. The calibration factors are given below in Table B-1 for the three load cells. Since the weight of the rotadome rests on the load cell, the zero-load point can only be established during a no-wind condition. This presents a problem during testing due to load-cell zero drift over a long period of time.

TABLE B-1. LOAD-CELL CALIBRATION FACTORS

Leg (deg)	Calibration (lb/0.01 volt)
0	11.15
120	9.69
240	10.60

The load cells were mounted under the three legs of the ASDE-3 rotadome-mounting pedestal. The distance from each load-cell center to the rotadome rotation center was 3.90 ft. The load cells were mounted between 1.0 ins thick mounting plates that were attached to the tower roof and each leg of the pedestal. The installation also included safety bolts that could be secured in case of high-wind conditions. A photograph of the installation is shown in Figure B-2.

The load cells were subjected to side loads due to drag and differential expansion between the rotadome pedestal and the tower roof. The side loads were estimated and found to be within the specification of the load cells chosen. The influence of the side loads on the load-cell readings was assumed to be zero due to lack of better information.

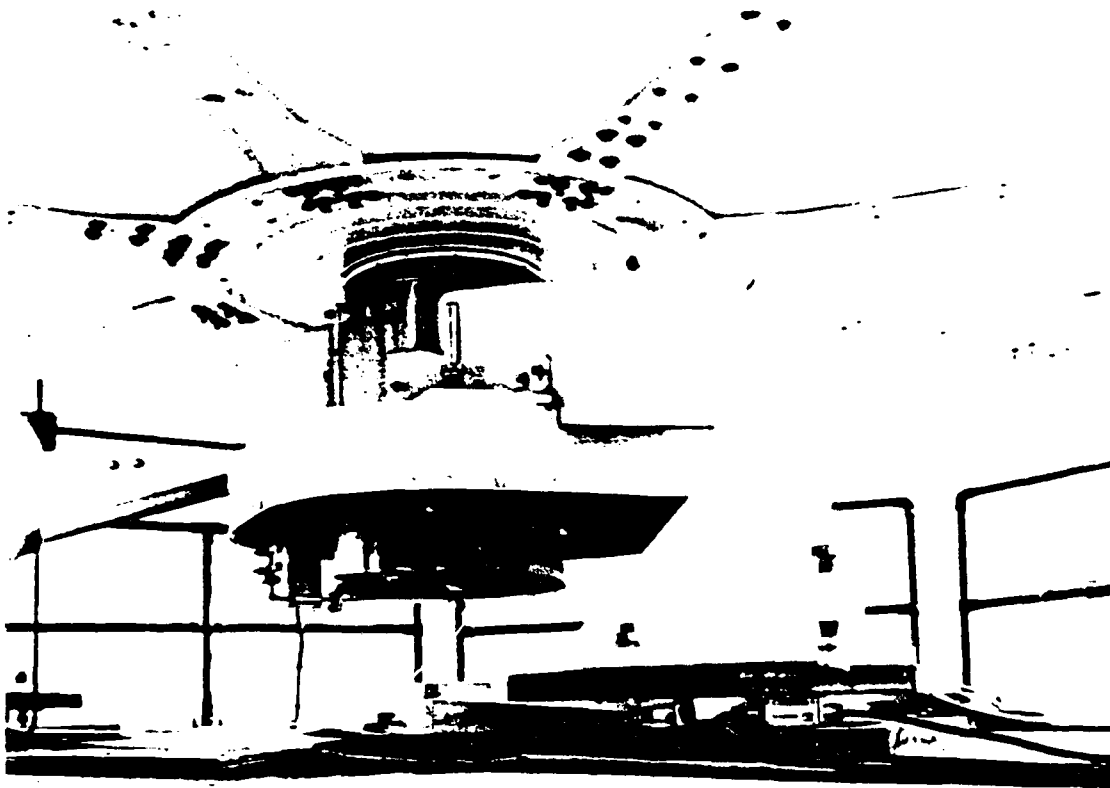


FIGURE B-2. LOAD-CELL INSTALLATION

The wind instrumentation consisted of a single three-axis propeller-type anemometer (Gill Model 27004). This instrument was mounted on a 120-ft high portable tower approximately 225 ft from the rotadome axis. The portable tower and anemometer can be seen in Figure B-1. The axis of the anemometer was 14.5° from the N-S side of the tower platform. A sketch of this instrumentation is shown in Figure B-3. The anemometer calibration was taken from the manufacturer's specifications. This factor is 62.48 ft/sec/volt.

In the initial phase of this program, other wind instrumentation was considered. Anemometers suspended from the tower were abandoned based on wind tunnel information that the airstream disturbances caused by the tower extended several tower diameters upstream. This makes local wind measurement unreliable in estimating approaching wind velocity. The far-field measurement provided by the anemometer as used in the field test is quite satisfactory for steady-state wind conditions as long as the anemometer is not in the wake of the tower. However, if the wind is rapidly changing (gusty), it is difficult to interpret the load measurements since the wind velocity (and direction) is not the same at the rotadome and anemometer. In a steady 30-mph wind (44 ft/sec), it takes about 5 seconds for the air going past the anemometer to reach the rotadome.

Data Acquisition and Reduction

The data from the load cells and anemometers were recorded on three two-channel strip-chart recorders (Gould 110 model 15-4328-00). Each division on the voltage scale corresponded to 2.4 sec (5 cm/min). Some difficulty in data reduction was encountered due to differences in chart speeds of the three recorders. This was accommodated by scaling the data using coincident timing marks recorded on the three charts. The indicated zeroes for the load cells were judged to be in error. The zeroes used in the data reduction were those established during the load-cell calibration which was carried out one day after the data was recorded.

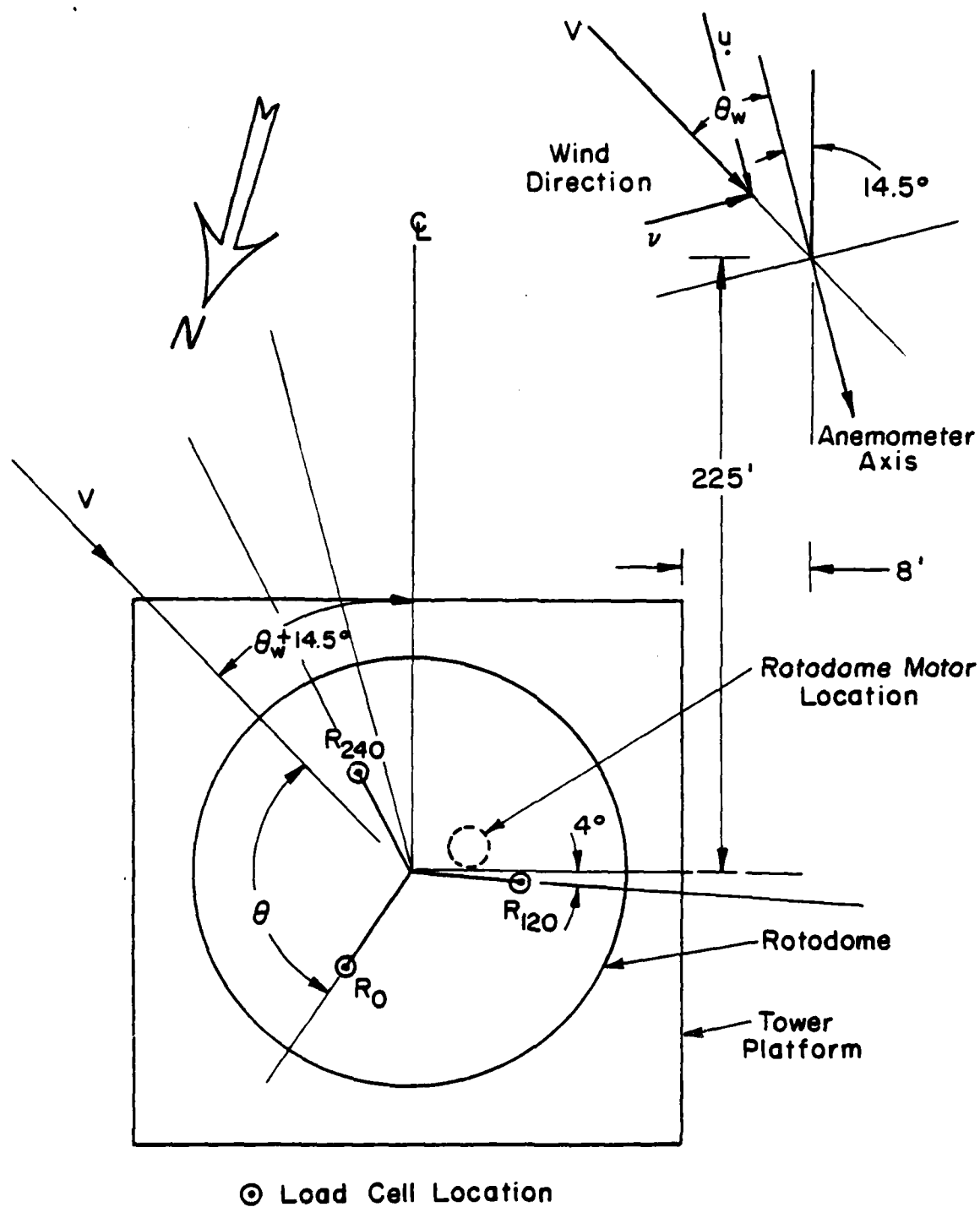


FIGURE B-3. FIELD TEST INSTRUMENTATION LAYOUT

The six channels of data (three reactions and three velocity components) were converted to physical quantities using the load-cell calibrations given in Table B-1 and the anemometer calibration factor (62.48 ft/sec/volt). Further reduction proceeded as follows.

The horizontal component of the wind velocity and the angle relative to the anemometer are given by

$$V = \sqrt{u^2 + v^2},$$

$$\theta_w = \tan^{-1}(v/u).$$

Some care must be used in calculating θ_w to be sure that the correct quadrant is selected in calculating the arctangent. The wind angle relative to the 0° leg of the rotadome is (see Figure B-3)

$$\theta = 131.5^\circ - \theta_w.$$

The lift (L), pitching moment (P), and rolling moment (R) are calculated from the reactions as follows:

$$L = R_o + R_{120} + R_{240},$$

$$P = \ell \cos \theta \left[R_o - \frac{1}{2} R_{240} - \frac{1}{2} R_{120} \right] +$$

$$\ell \sin \theta \left[\frac{\sqrt{3}}{2} R_{240} - \frac{\sqrt{3}}{2} R_{120} \right],$$

$$R = \ell \sin \theta \left[-R_o + \frac{1}{2} R_{120} \right] +$$

$$\ell \cos \theta \left[\frac{\sqrt{3}}{2} R_{240} - \frac{\sqrt{3}}{2} R_{120} \right],$$

where ℓ is the distance of the load cells from the center of the rotadome.

It should be emphasized that the pitching and rolling moments are calculated at the plane of the top of the load cells. The

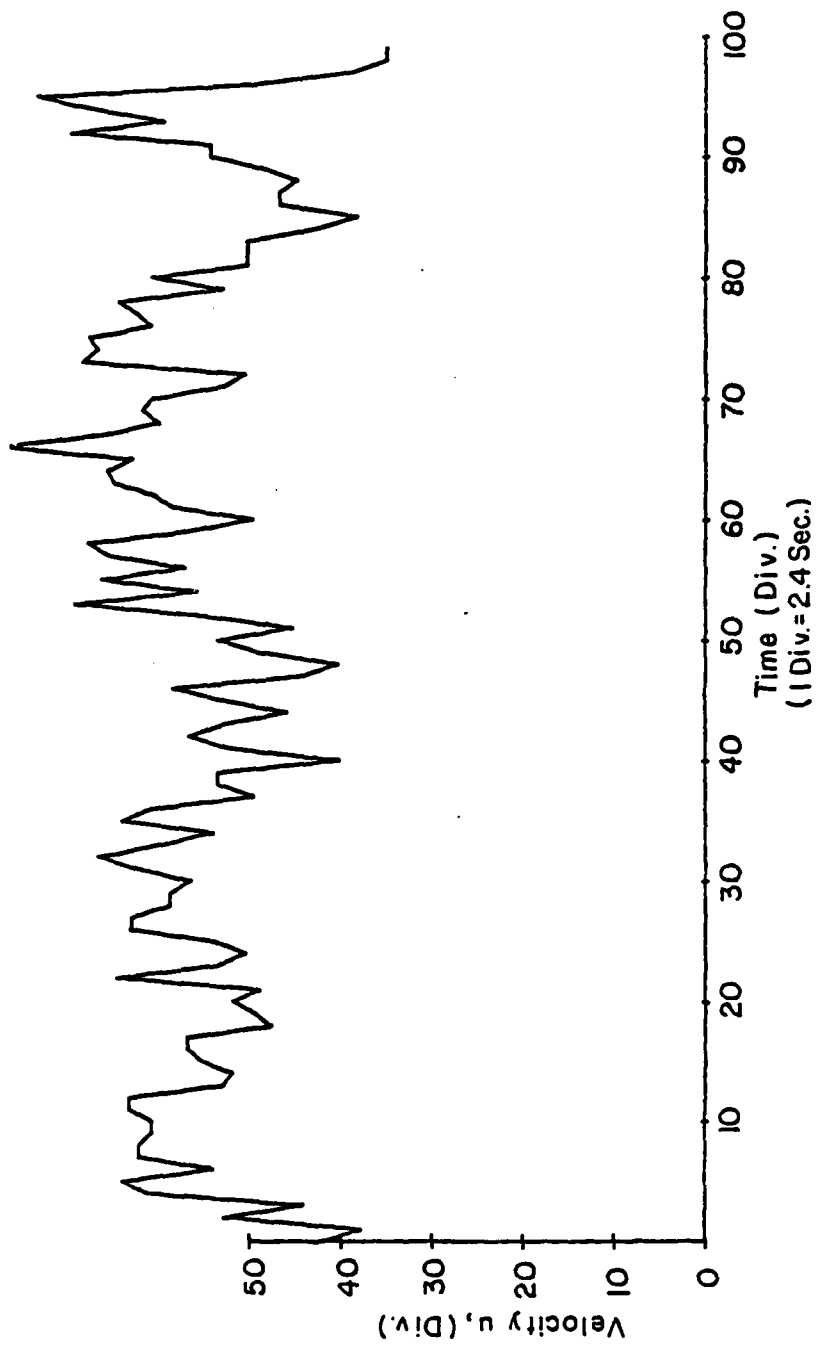


FIGURE B-4a. RAW-DATA SAMPLE VERSUS TIME

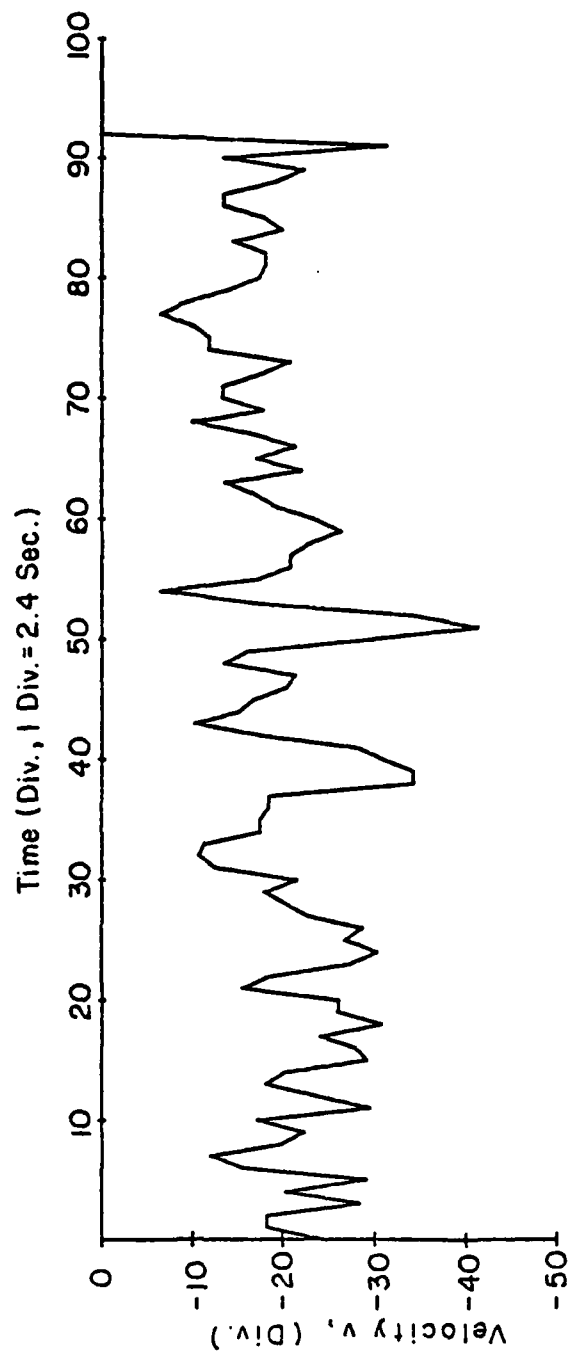


FIGURE B-4b. RAW-DATA SAMPLE VERSUS TIME (CONTINUED)

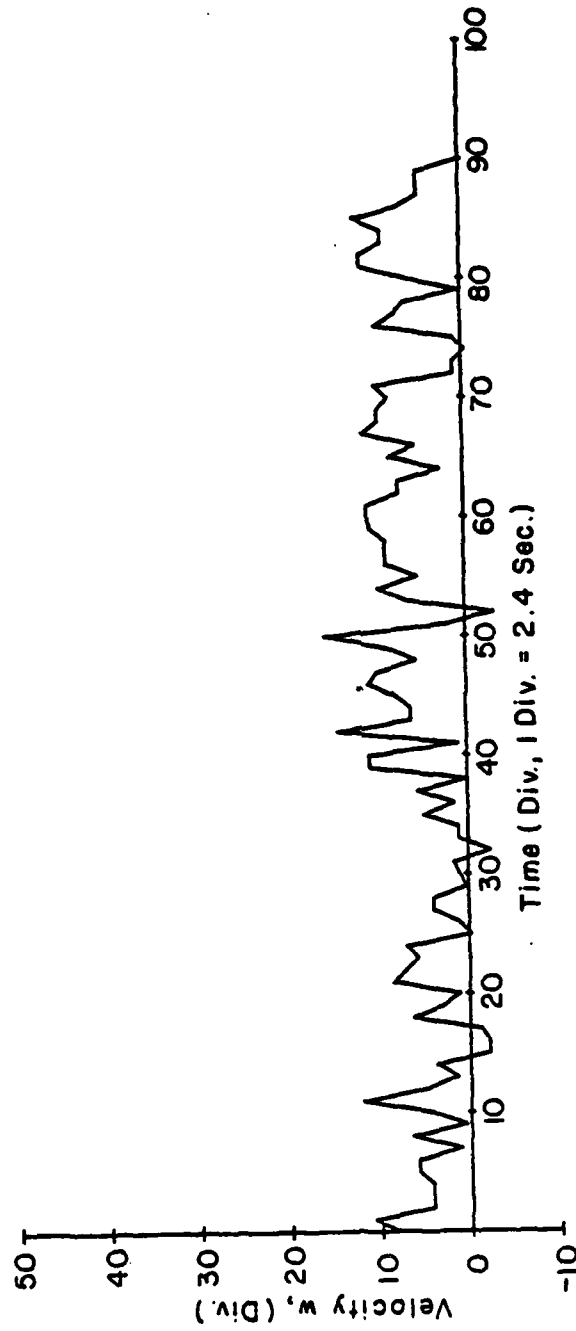


FIGURE B-4c. RAW-DATA SAMPLE VERSUS TIME (CONTINUED)

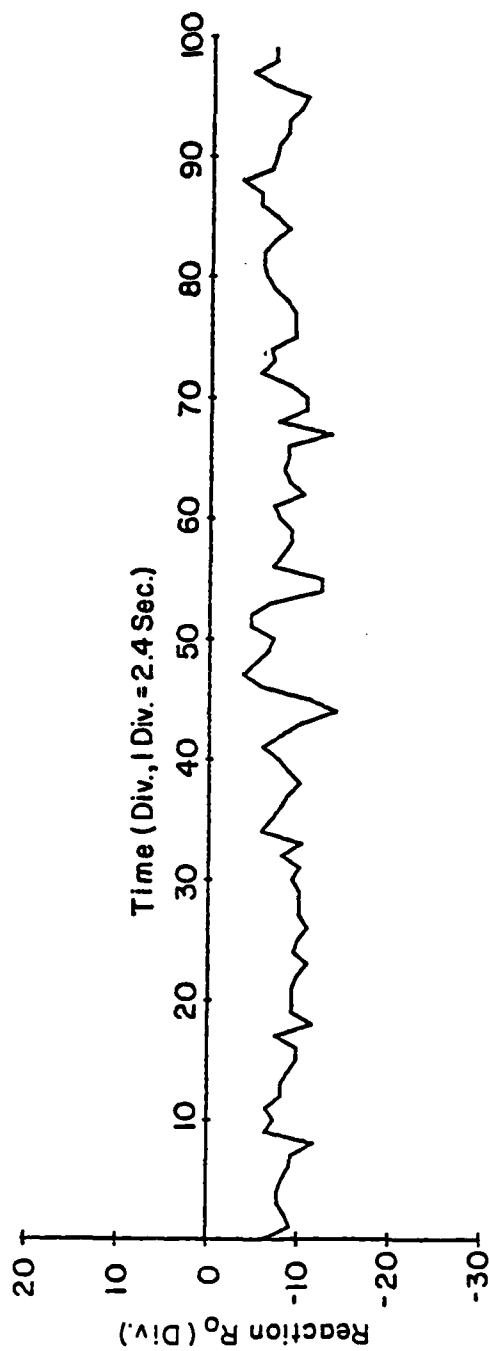


FIGURE B-4d. RAW-DATA SAMPLE VERSUS TIME (CONTINUED)

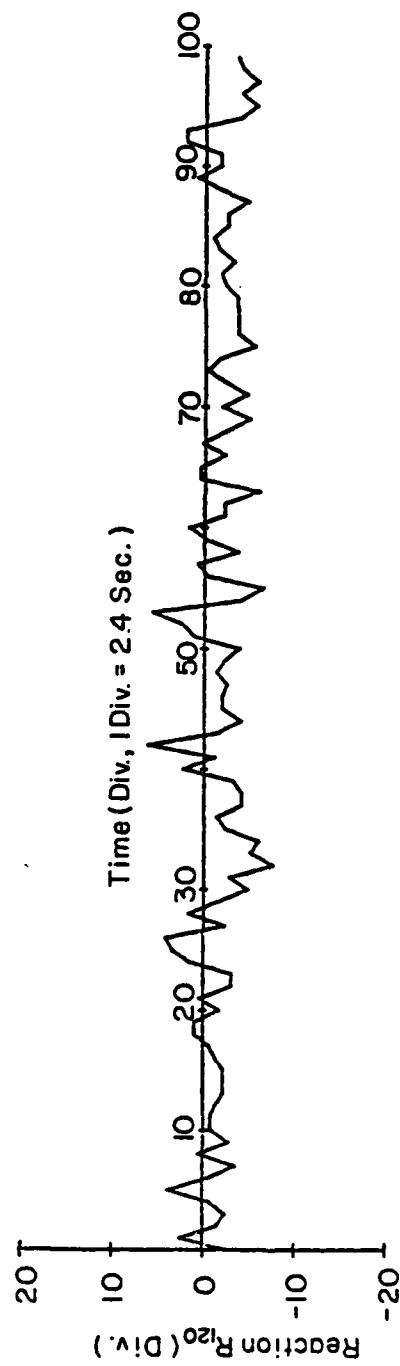


FIGURE B-4e. RAW-DATA SAMPLE VERSUS TIME (CONTINUED)

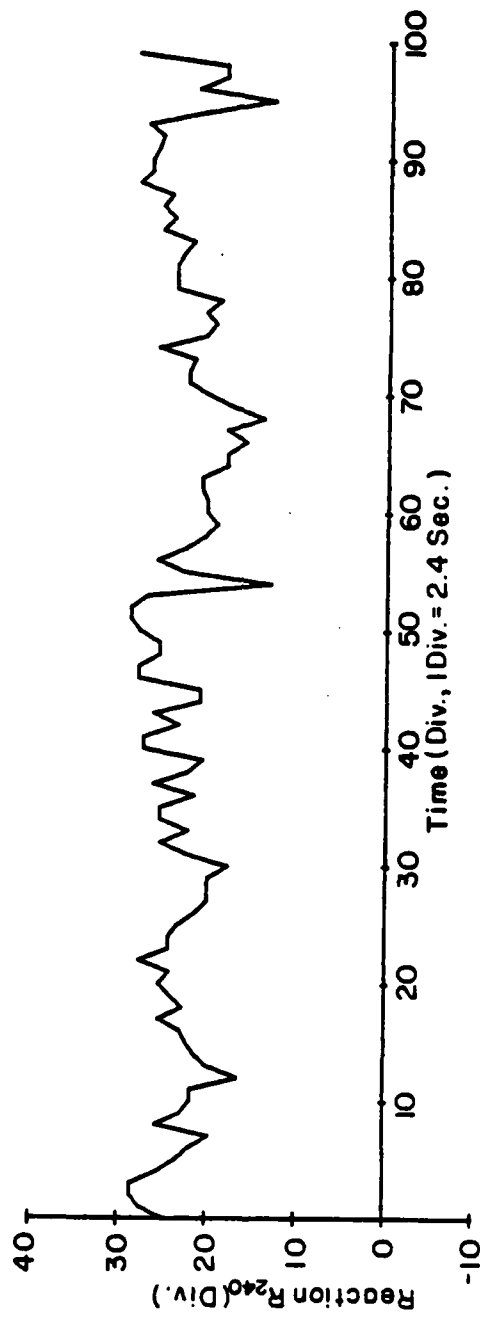


FIGURE B-4f. RAW-DATA SAMPLE VERSUS TIME (CONCLUDED)

calculation of pitch, for example, in any other plane requires that the drag is known.

The coefficients were calculated as follows:

$$C_L = L/qA,$$

$$C_m = P/qAd,$$

$$C_\ell = R/qAd,$$

where $A = 88.474$ ft, $d = 18.0$ ft, and $\ell = 4.9$ ft.

Standard-day, sea-level conditions were assumed, and therefore, $\rho = 0.002378$ lb/sec²/ft⁴ was used for the calculations. Recorded conditions during the data acquisition yield $\rho = 0.002391$, obtained from barometric pressure = 762.0 - 762.5 mm Hg, temperature = 55° - 56°F and dewpoint = 50°F. The small difference (1/2 percent) in the actual air density and that used for data reduction do not warrant any correction in the final data. It should be noted that the dimension ℓ is not correct in the program used to reduce the data. The distance between load-cell centerline and rotadome centerline was actually 3.9 ft, and therefore, the final moment data must be multiplied by 3.9/4.9 or 0.7959 to obtain the correct values. This correction has been made for data used in tables or otherwise in this report, and has not been made for Figures B-5 and B-6.

Data Processing

The data used to calculate the rotadome lift and moment coefficients were recorded by FAATC personnel on 9 April 1980, between 1600 and 1915 hours. Wind velocities during this time were between 20 and 45 ft/sec. The data were divided into sets with each set approximately 240 seconds long. The sets selected have a minimal up and down velocity (w), and hence, are more likely to represent non-swirling flow.

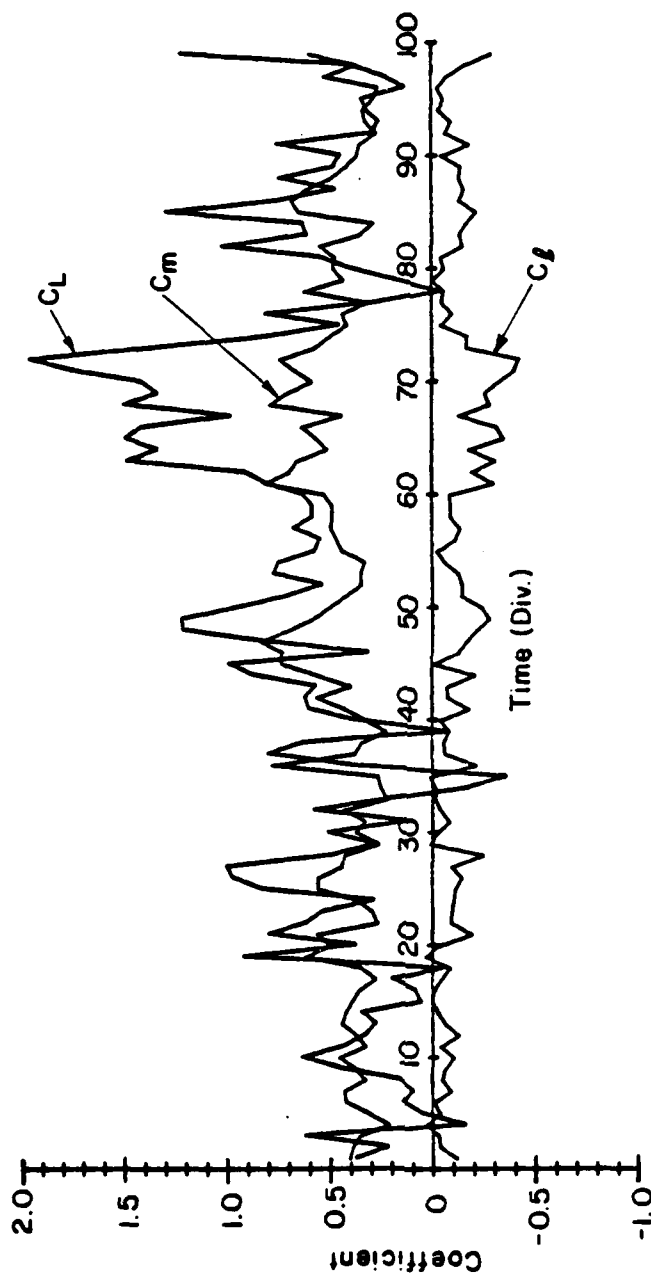


FIGURE B-5a. FORCE AND MOMENT COEFFICIENTS AS A FUNCTION OF TIME

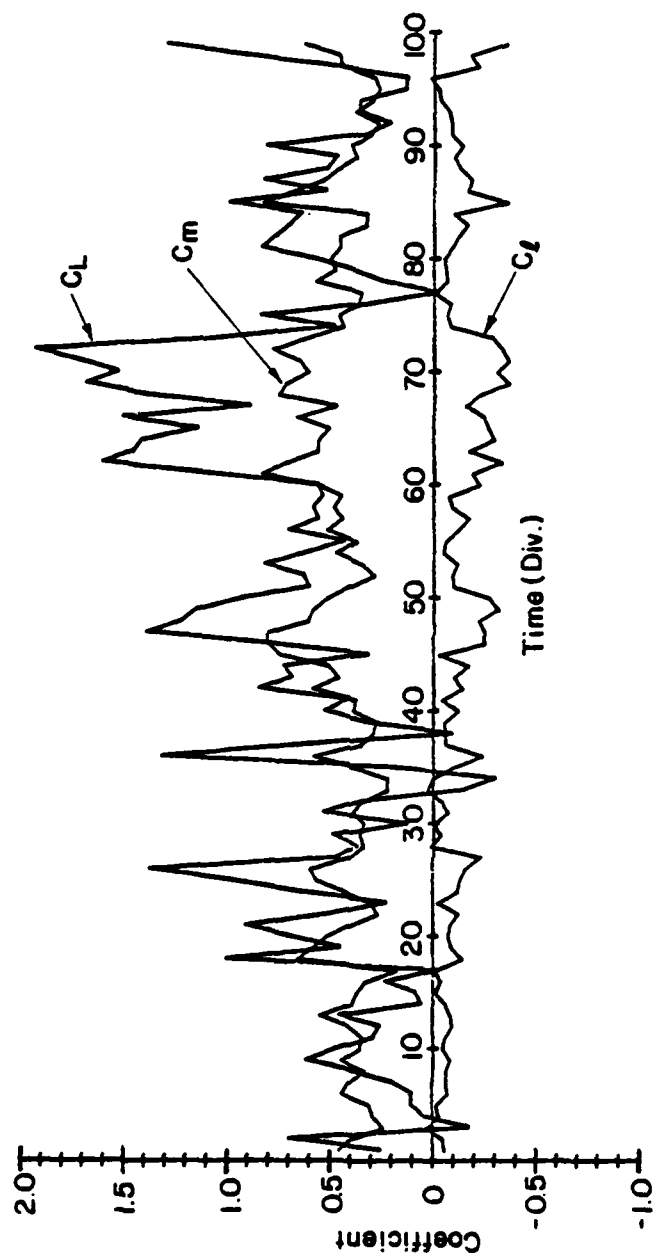


FIGURE B-5b. FORCE AND MOMENT COEFFICIENTS AS A FUNCTION OF TIME (CONTINUED)

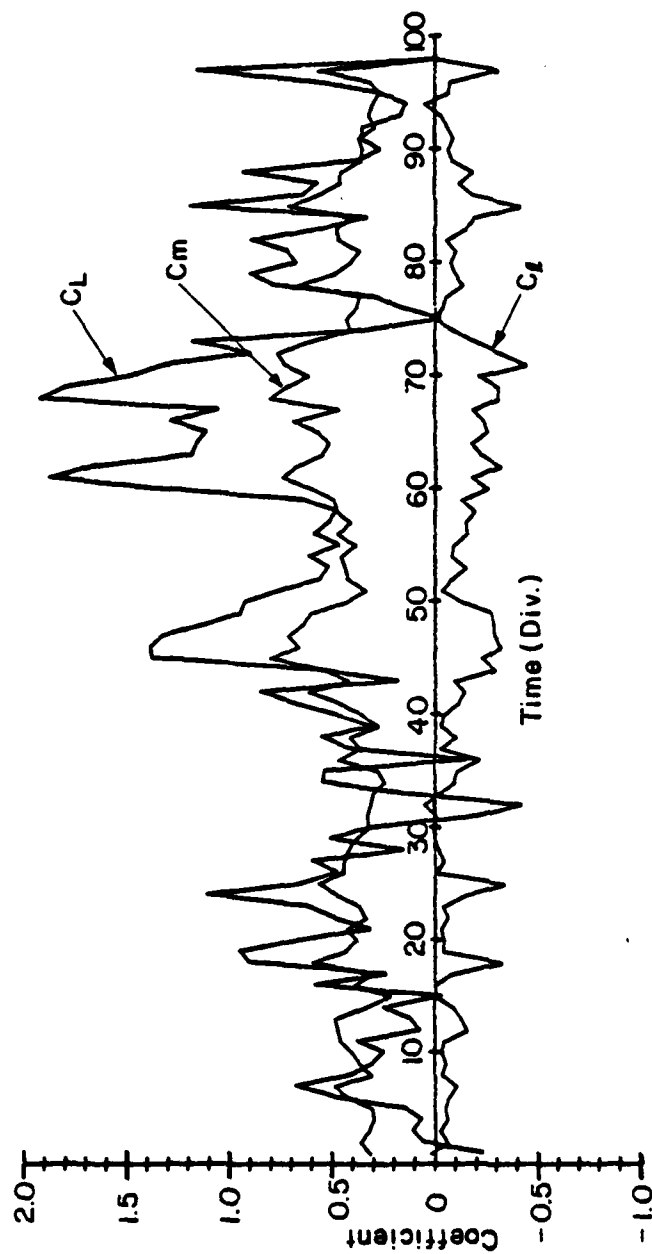


FIGURE B-5c. FORCE AND MOMENT COEFFICIENTS AS A FUNCTION OF TIME (CONTINUED)

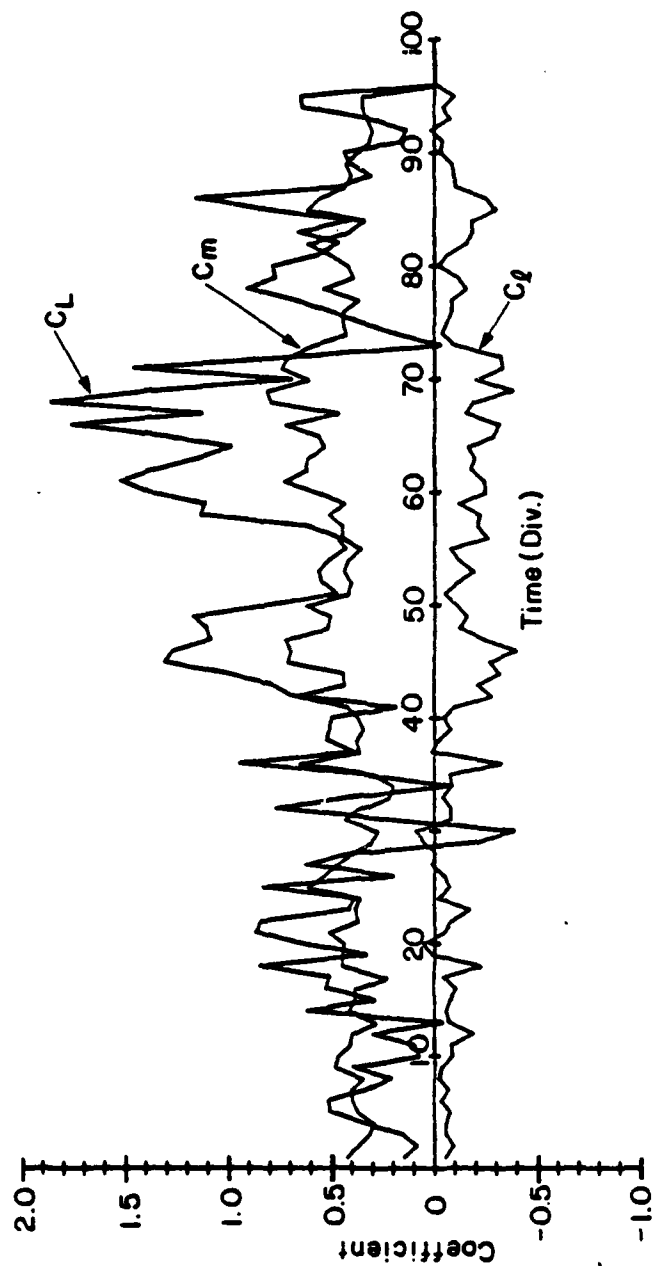


FIGURE B-5d. FORCE AND MOMENT COEFFICIENTS AS A FUNCTION OF TIME (CONCLUDED)

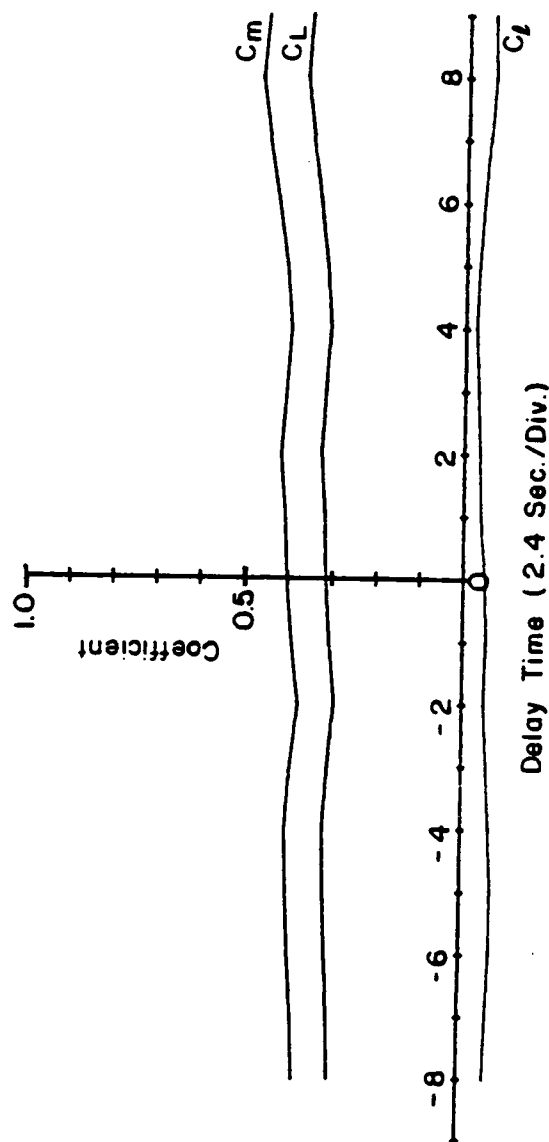


FIGURE B-6a. FORCE AND MOMENT COEFFICIENTS VERSUS DELAY TIME

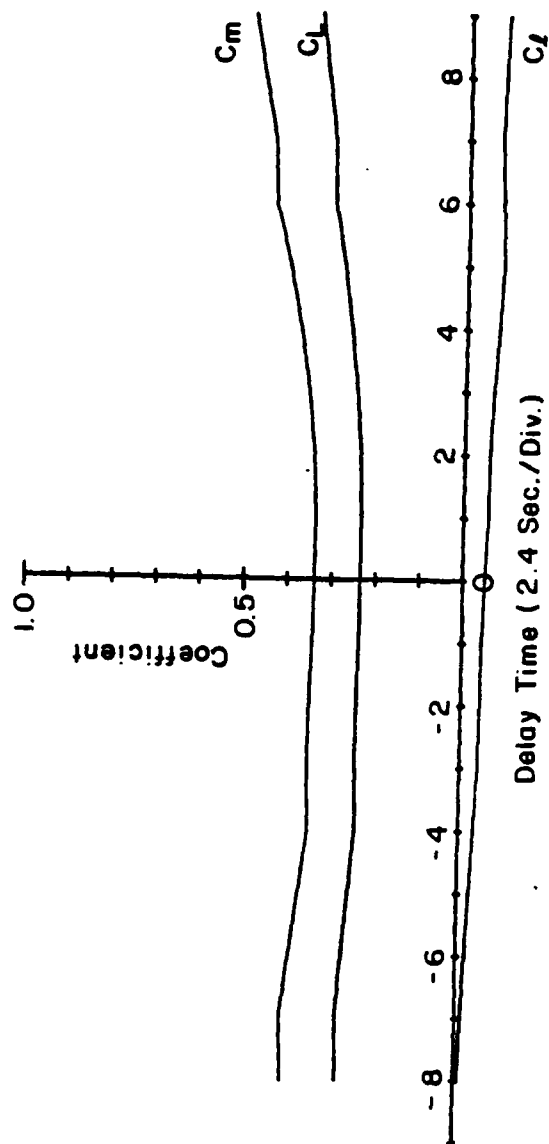


FIGURE B-6b. FORCE AND MOMENT COEFFICIENTS VERSUS DELAY TIME (CONTINUED)

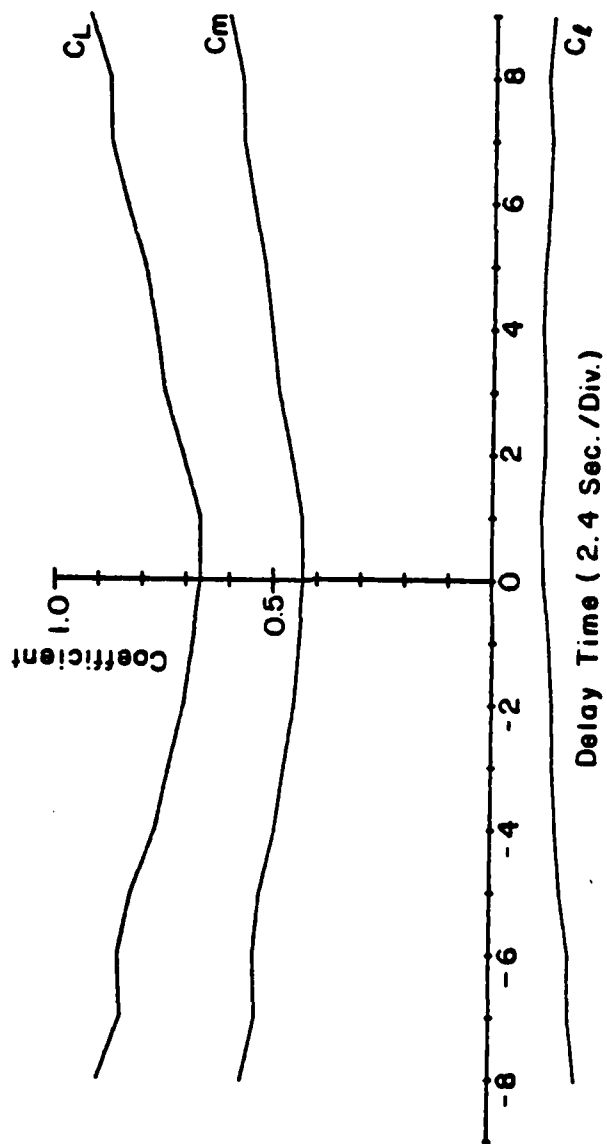


FIGURE B-6c. FORCE AND MOMENT COEFFICIENTS VERSUS DELAY TIME (CONTINUED)

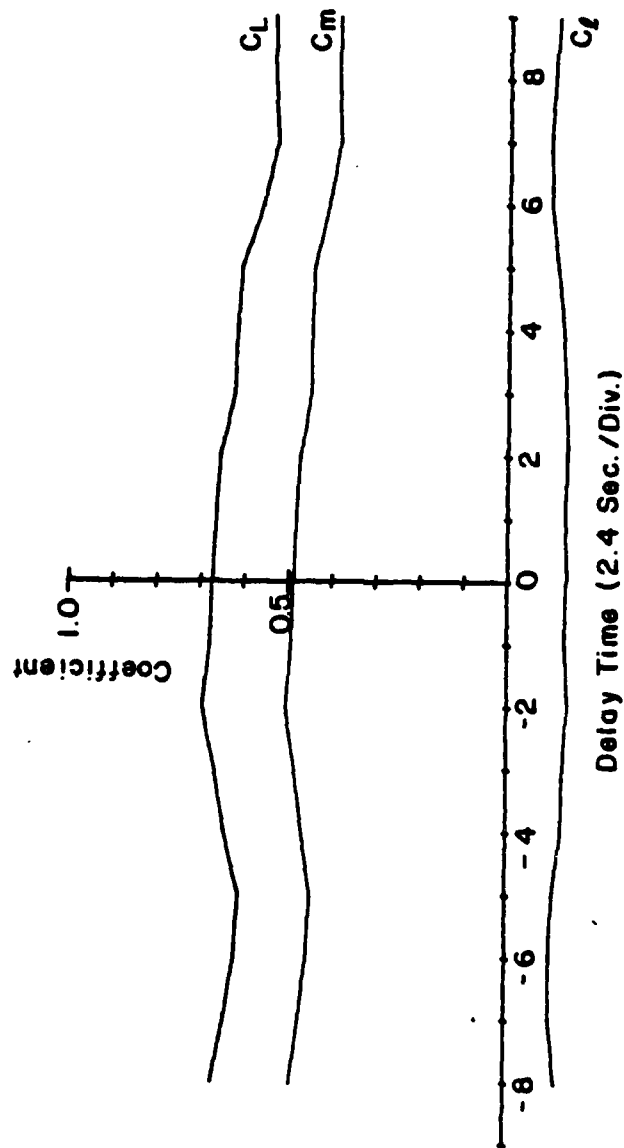


FIGURE B-6d. FORCE AND MOMENT COEFFICIENTS VERSUS TIME DELAY (CONTINUED)

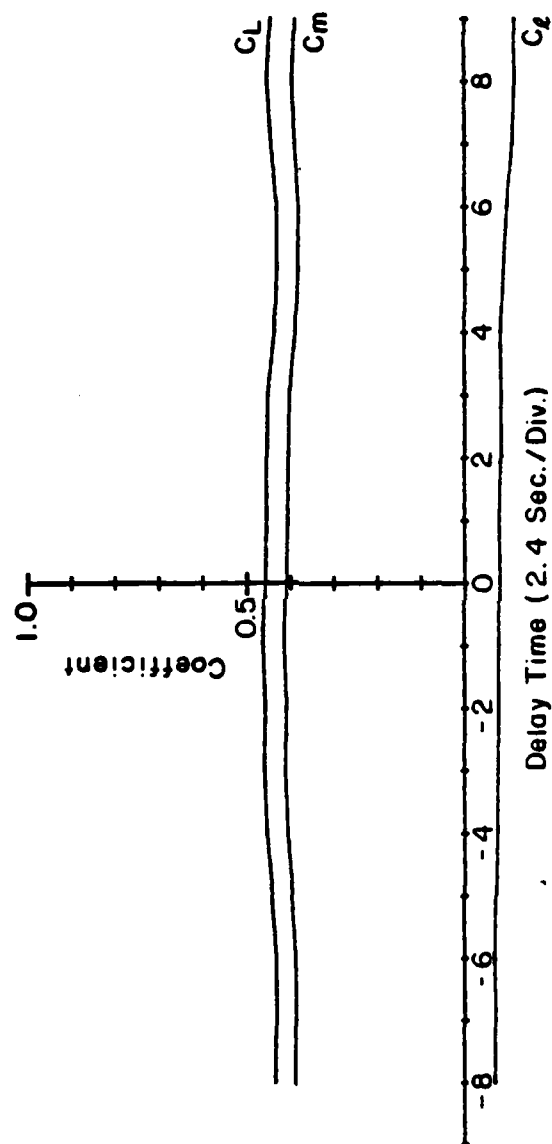


FIGURE B-6e. FORCE AND MOMENT COEFFICIENTS VERSUS TIME DELAY (CONTINUED)

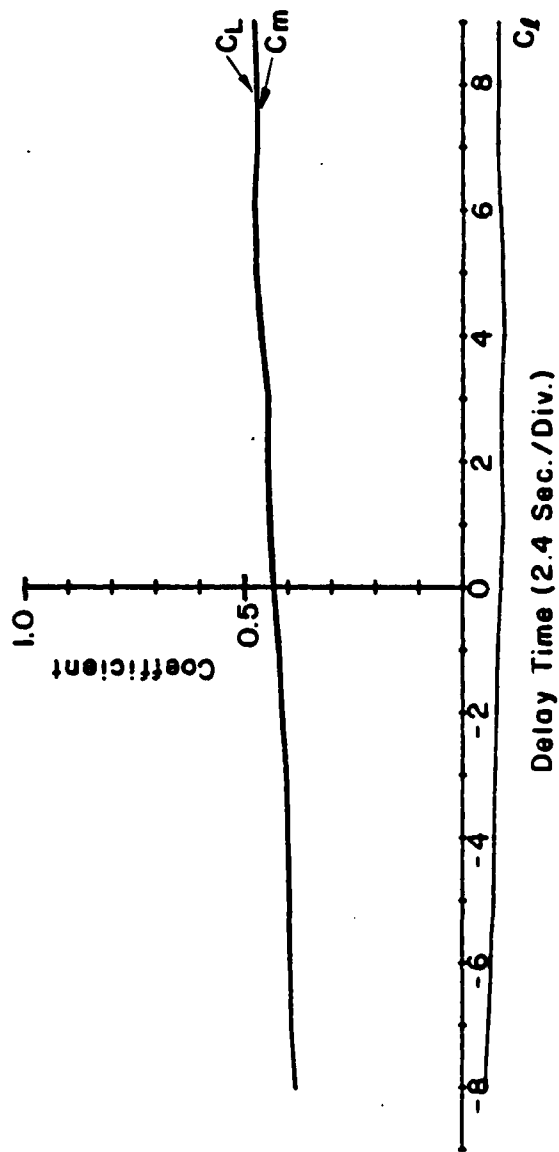


FIGURE B-6f. FORCE AND MOMENT COEFFICIENTS VERSUS DELAY TIME (CONTINUED)

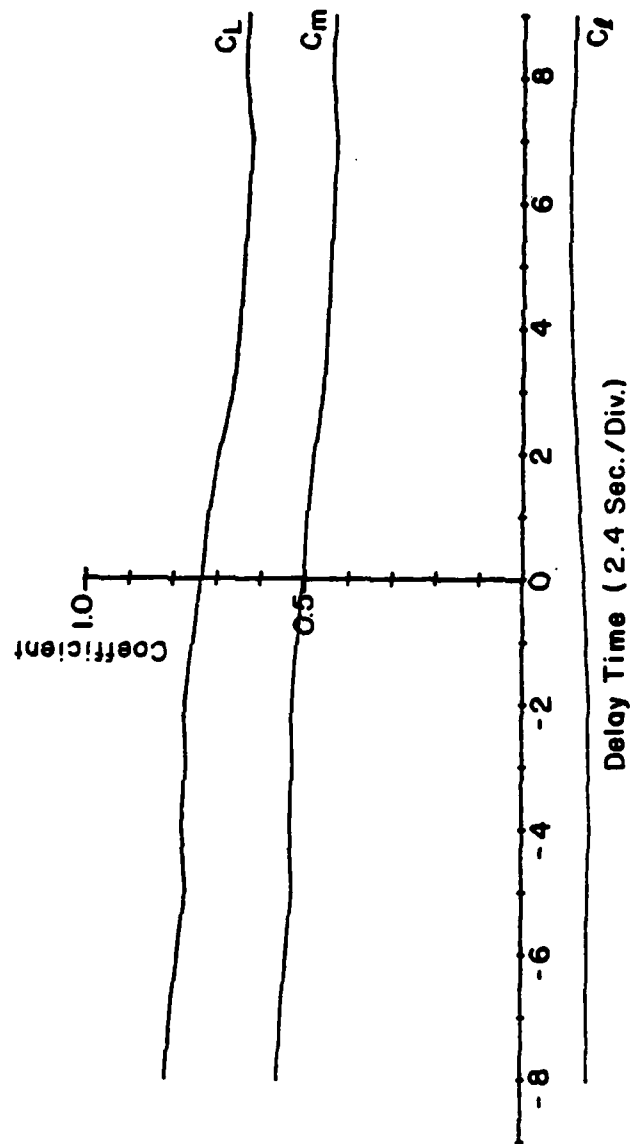


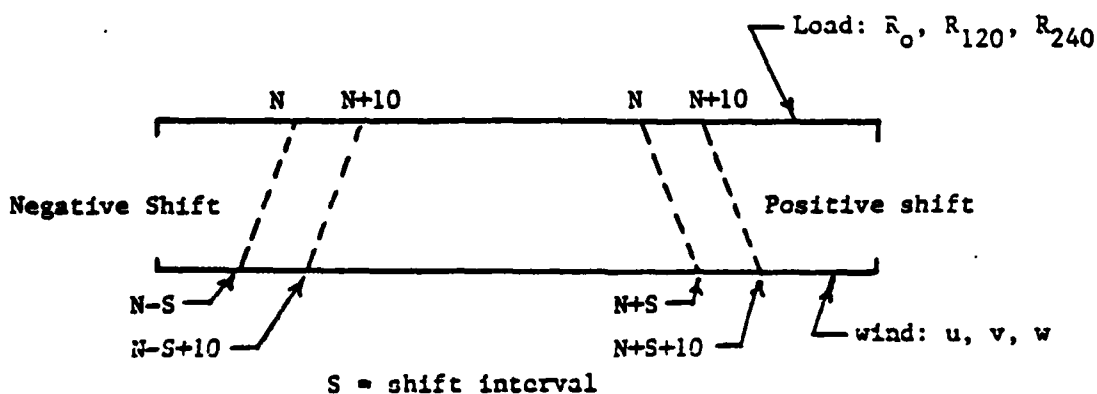
FIGURE B-6g. FORCE AND MOMENT COEFFICIENTS VERSUS TIME DELAY (CONCLUDED)

An interval of 240 seconds long was established on the recorder chart for each trace of R_0 , R_{120} , R_{240} , u , v , and w . The beginning and end points of each interval were determined by taking into account the facts that the three recorders ran at different speeds, and that the two pens on the same recorder were separated by two small divisions on the horizontal axis. Traces of loads and winds were digitized using an HP 9827A plotter in conjunction with an HP 9825A calculator. Data were digitized at every 2.4 seconds (or one small division of the charts) for a total of 100 intervals. The resulting six sets of data for each case are stored on a digital tape cartridge in six separate files. It should be pointed out that the stored data are in terms of the number of small divisions on the recorder chart. The procedure for converting these data into the lift, pitching, and rolling-moment coefficients is outlined in the preceding section.

The following data reduction schemes were carried out.

- a. Plots made of raw data: an example of these plots is included as Figure B-4.
- b. Data averaged over 10 points.

The diagram below shows the files of load and wind data.

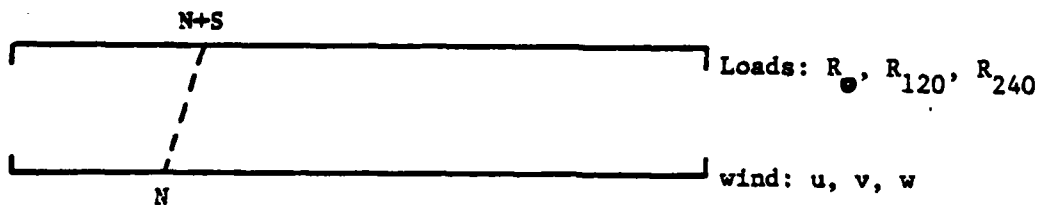


The 100 data points for each load and wind sensor were taken simultaneously. However, because of the remote location of the wind sensor, there is a time delay between the appropriate load and wind data. The distance between the tower and the wind sensor is approximately 225 ft, and using an average wind velocity (say, 36 fps), the resulting delay is approximately 6 sec or between 2 or 3 intervals on the data file.

Taking this fact into account, it was decided to analyze the data with a variable-shift interval. The diagram above shows both negative and positive shifts. In the negative-shift case, the average load data between N th and $(N+10)$ th points are matched with the average wind data from the previous $(N-S)$ th point to $(N-S+10)$ th point to give the lift, pitching, and rolling aerodynamic coefficients. In the positive-shift case, the wind data from the "future" time are matched with the load data. This is unrealistic for these particular data since the wind sensor is always located upstream. The resulting aerodynamic coefficients are plotted against the shift interval S for various values of the starting point N . Examples of graphs are included in Figure B-6.

c. Same as above, and data are averaged over 20 points (see Figures B6e-B6g).

d. Aerodynamic coefficients given as a function of time: In this case, data were processed in a manner depicted below:



The wind data, i.e., u , v , and w of the N th point are matched with the load data; e.g., R_0 , R_{120} , and R_{240} of the $(N+S)$ th point. N is the starting point, and S is the amount of shift which varies from 0 to 6 intervals. The resulting coefficients are then plotted as a function of N . The resulting graphs show the variation of the aerodynamic coefficients as a function of time.

e. Averaged raw data: Raw data were averaged over the entire file, first half of the file and second half of the file. The resulting averages were then converted to aerodynamic coefficients.

f. An attempt was made to examine the frequency content of the load and wind data using a Fourier analysis scheme. An attempt was made at correlating predominant frequencies if they could be located between the two data types. This attempt was unsuccessful however; no useful data could be obtained.

Field Test Results

The data from the field tests were analyzed to extract information for comparison with the wind tunnel data. This resulted in a large number of computer-generated plots, and not all are included in this report. Instead, a typical data sequence is described in this section.

The first set of graphs presents the raw data as digitized from the strip-chart recordings (Figures B4-a-B4f). These data are typical of those recorded. It shows considerable fluctuation about a fairly steady mean. Large fluctuations in velocity are accentuated in the data reduction since the dynamic pressure is proportional to the square of the velocity.

The next set of data (Figures B5a-B5d) shows the coefficients as a function of time. Due to the delay time of the wind in going from the anemometer to the rotadome, the data have been shifted as described in the preceding section. Four different delay times are used in these figures. All of these coefficients show considerable variation with time. The use of a delay time does

not appear to improve the data to any great extent. This was characteristic of all the data processed, probably due to the extremely unsteady wind conditions under which the data were recorded.

The next set of data was developed in an attempt to remove some of the unsteadiness. The data averages 10 (or 20) points and then, shifts the data in time to account for the wind delay. The results are presented for various data averages, number of points averaged, and delay times, in Figures A6a to A6g. This averaging considerably smooths the data. The data are fairly independent of the delay times for negative delay (the appropriate shift for the wind direction in this case). However, considerable variation in coefficients is still seen to be dependent on which 10 (or 20) points of data are averaged.

The last data-processing method averages either half of the data file or the complete data file. The results are given for an example in Table B-2 below.

TABLE B-2. DATA-AVERAGED RESULTS

AVERAGE	C_L	C_m	C_ℓ
First half	0.411	0.328	-0.060
Second half	0.720	0.380	-0.109
Overall	0.557	0.353	-0.083

The table shows that the results for C_m and C_ℓ are much the same over the span of the data recorded. However, as Figure B-5 shows, there is considerable variation during the data span recorded.

The rolling-moment data (C_ℓ) on Figures B-5 and B-6 are fairly typical of all of these data recorded. The non-zero C_ℓ values are at least partially due to the wind angle relative to the tower, and partially due to nonuniformities in the wind-velocity front approaching the tower. Since the vast majority of these C_ℓ data are of negative sign, it is also possible that the assumed zero-load location on the raw-data acquisition charts is incorrect, by a small number, for one or more of the load cells.

APPENDIX C
REPORT OF NEW TECHNOLOGY

The work accomplished under this contract as reported herein provides data that could be used to establish loads which might be transitted to a supporting tower roof due to airloads acting on a radome attached to that roof. This report contains data on specific radome shapes attached to specific towers peculiar to the ASDE radar, and represents the only data of its kind.

110 Copies

C-1/C-2

